

Study of Ocular Aberrations Within a 10 *deg* Central Visual Field.

by Maciej Nowakowski

Supervisor: Prof. Chris Dainty

Co-supervisor: Dr. Alexander Goncharov



A thesis submitted in partial fulfilment of the requirements for the degree of
Doctor of Philosophy,

School of Physics, Science Faculty,
National University of Ireland, Galway

March 2011

Abstract

The human eye has been a subject for study for many scientists across several centuries. Even axial or foveal image quality is often degraded by wavefront aberration or intraocular light scatter. Additionally vision degrades with age. It is also known that the aberrations of the eye, like any optical system, vary with the field angle. Image degradation increases with retinal eccentricity, which is the main factor limiting retinal imaging off-axis. Secondly, the knowledge of the on-axis (foveal) and off-axis ocular aberrations pattern is especially important for understanding the optical properties of human eye and all origins of its optical imperfections. This knowledge would give reasonable answer of how our built-in optical system can be corrected and modeled, taking into account all inter-subject variabilities.

The central visual field is not fully understood yet. With all asymmetries, tilts and decenterations of the optical surfaces of the eye, the Seidel theory of aberrations should be expanded accordingly to match the case of the eye. We performed sequentially measurements of the field aberrations within the horizontal and vertical meridian (10x10 degree visual field) of 25 young eyes with an aberrometer based on the Shack-Hartmann principle. The experiments have resulted in field distribution and the weights of ocular aberrations and gave an idea about complexity of the optical system of the eye.

We stressed the importance of taking into account all non-negligible effects that influences the final data. We performed ocular wavefront measurements in order to estimate optical effects of the tear film's evolution on the cornea after a single blink. The experimental results suggested that it can significantly influence measured wavefronts by causing an additional temporal fluctuation of some of the aberration terms.

Acknowledgements

First of all I would like to thank my supervisor Prof. Chris Dainty. He opened the doors of the Applied Optics Group welcoming me aboard. I was very fortunate to have such a good supervisor throughout my PhD studies. He shared his deep knowledge about the field of optics on an every day basis. I have also benefited from his constant enthusiasm, support, common-sense advice and constructive criticism that helped me to proceed with my research and bring my thesis to the final form.

I am also very grateful to my co-supervisor Dr. Alexander Goncharov that I have had the pleasure of working with. He always found the time to discuss my research, often cutting to the core of the problem. His valuable and vast knowledge helped me to understand and opened my eyes to the complex nature of the human eye's optical system.

Many thanks also to all my colleagues from the group that were interacting with me along the "*scientific*" meridian but moreover, became my friends for life. I salute Dr. Charlie Leroux for all open-air discussions we went through, talking about the meaning of life. I salute Dr. Conor Leahy, who never said "*no*" if I needed his help or just playing his drums. I salute Dr. Eugenie Dalimier, who guided me and showed some tips and tricks when I started. I salute Matt Sheehan for being supportive and open for any question I could come up with. Thanks to Dr. Szymon Gładysz for all advices I gathered from him. I also owe gratitude to other good people I got the chance to meet during my studies.

I would like to express my special gratitude to my parents, who supported me from the first day I started my high-level education in Wroclaw University of Technology (1997). They never stopped believing in me, always cheered me up and supplied me with every kind of support I could imagine. Thank you so much, I will never forget all your help throughout my entire education.

Finally I salute my wife Marta and my little precious girl Zosia. Marta for huge credit of patience, understanding and for never-ending mental support. Zosia for giving me a large portion of motivation when she came to this world in September 2010. There would be little chance to accomplish this thesis without both of you.

This research was funded under the Marie Curie Programme "*HIRE SOMI*", MEST-CT-EST 2005-020353-2, and also by Science Foundation Ireland under Grant No. SFI/07/IN.1/1906.

Chciałbym z całego serca podziękować moim rodzicom za całą pomoc, którą otrzymałem od nich od początku mojej drogi akademickiej rozpoczętej w murach Politechniki Wrocławskiej. Przez te wszystkie lata nigdy we mnie nie zwątpili a bez ich olbrzymiego wsparcia osiągnięcie jakiegokolwiek celu byłoby niemal niemożliwe. Za to i za wszystko co dla mnie zrobiliście należą Wam się najwyższe wyrazy wdzięczności i szacunku. Tacy rodzice to prawdziwy skarb, dziękuję Wam kochani.

Podziękowania składam również na ręce mojej żony. Marto, zawsze byłaś dla mnie mocnym oparciem i szalenie dużo Ci zawdzięczam. Dziękuję Ci, tym bardziej, że gdyby nie Ty pewnie w ogóle nie pisałbym teraz podziękowań włączających tę pracę.

Jestem także niezmiernie wdzięczny pozostałym członkom mojej rodziny którzy szczerze trzymali za mnie kciuki do samego końca. Chodzi mi tu o moją drogą siostrę z mężem i dziećmi a także drogich teściów. Bardzo Wam za te "*kciuki*" dziękuję.

Maciej Nowakowski
Galway, March 2011

To Marta and my little precious Zosia.

Contents

Abstract	i
Acknowledgements	ii
List of Tables	viii
List of Figures	ix
Abbreviations	1
1 Introduction and Thesis Synopsis	2
1.0.1 Simplified Historical Review of the Ophthalmic Instrumentation	3
1.0.2 Modern Times	5
1.0.3 Thesis Synopsis and Publications	6
2 Background for the Study	8
2.1 Optics and Physiology of the Eye	9
2.1.1 Axes of Reference in the Eye	12
2.2 Mathematical Models of the Eye	15
2.3 Monochromatic Aberrations of the Optical Systems	18
2.3.1 Polynomial Representation of Aberrations	22
2.3.2 Primary Distortion	24
2.3.3 Primary Field Curvature	25
2.3.4 Primary Astigmatism	26

2.3.5	Primary coma	28
2.3.6	Primary Spherical Aberration	29
2.3.7	Secondary Aberrations and Seidel Series	31
2.3.8	Zernike Power Series and the RMS Wavefront Error	32
2.4	Measures of the Quality of Optical Systems	37
2.4.1	Ocular Aberrations in the Human Eye	41
2.5	Wavefront Measurement Techniques for the Human Eye	45
2.5.1	Laser Ray-tracing	46
2.5.2	Spatially Resolved Refractometer	47
2.5.3	Tscherning Aberrometer	47
2.5.4	The Pyramid Wavefront Sensor	48
2.5.5	Shack-Hartmann Wavefront Sensor	49
2.5.6	Combined Wavefront and Corneal Topographer	52
3	On-axis and Off-axis Aberrations of the Human Eye	54
3.1	Literature Review	55
3.2	The Experiment	58
3.2.1	The Optical Setup	58
3.2.2	The Experimental Procedure	65
3.3	Experimental Results	68
3.3.1	Young Population Study	68
3.4	Estimation of the Isoplanatic Patch	82
4	Assessment of the Tear Film Contribution to the Total Ocular Aberration	85
4.1	Literature Review	86
4.2	Experimental Procedure	88
4.3	Experimental Results	94
5	Conclusions	107
5.1	Field Dependence of Ocular Aberrations	108
5.2	Optical Effects of Tear Film Evolution After a Single Blink	117

5.3 Future Work and Applications	122
Bibliography	126

List of Tables

2.1	Primary and Secondary Aberrations.	32
2.2	Zernike Polynomials.	36
3.1	Repeatability test of the aberrometer.	65
3.2	Subject full record table.	66
3.3	Assessment of the isoplanatic patch.	83
4.1	Additional wavefront aberration caused by a tear film variation. Zernike aberration orders.	105
4.2	Additional wavefront aberration caused by a tear film variation. Zernike aberration coefficients.	106

List of Figures

1.1	Helmholtz's ophthalmoscope	3
1.2	Gullstrand's slit lamp.	4
1.3	Image of the retinal photoreceptor cells.	6
2.1	Schematic layout of the right eye.	9
2.2	Cardinal points of the single lens.	12
2.3	The optical and visual axes of the eye.	13
2.4	The line of sight and pupillary axes of the eye.	14
2.5	Schematic tree of the development of the eye models.	17
2.6	The imperfect optical system.	19
2.7	The geometrical aberration of the ray: transverse, longitudinal, and angular.	20
2.8	Polar coordinates in the exit pupil.	23
2.9	Primary distortion aberration.	25
2.10	Primary field curvature aberration.	26
2.11	Primary astigmatism aberration.	27
2.12	Primary coma aberration.	28
2.13	Primary spherical aberration.	30
2.14	Zernike polynomials.	33
2.15	Zernike pyramid of polynomials.	35
2.16	Angular resolution of the two object points A and B	38

2.17	Variation in the width of the <i>PSF</i> as a function of pupil diameter.	39
2.18	Example of modulation transfer function (<i>MTF</i>) of the human eye as a function of retinal eccentricity.	40
2.19	Wavefront slopes.	45
2.20	Laser ray-tracing aberrometry.	46
2.21	Tscherning aberrometry.	48
2.22	The pyramid wavefront sensor.	49
2.23	Shack-Hartmann wavefront sensor principles (<i>a</i>).	50
2.24	Shack-Hartmann wavefront sensor principles (<i>b</i>).	50
2.25	Relationship between the wavefront slope across single <i>SH</i> lenslet. . .	51
2.26	Optical layout of combined corneal topographer and aberrometer based on Shack-Hartmann wavefront sensing.	53
3.1	Schematic layout of the off-axis measurements.	55
3.2	Schematic layout of the aberrometer.	58
3.3	Pupil image in the sensing channel.	59
3.4	Shack-Hartmann spots pattern image in the pupil plane.	60
3.5	Calibration of the aberrometer.	62
3.6	Repeatability test on the aberrometer.	64
3.7	Schematic layout of the off-axis measurement procedure.	67
3.8	The Optical Society of America standard coordinate system.	68
3.9	Population study of 25 young eyes. Mean values for each Zernike coefficient.	69
3.10	Population study of 25 young eyes. Mean absolute values of the Zernike coefficients.	70
3.11	Mean <i>RMS</i> wavefront error across the horizontal and vertical visual field.	72
3.12	Mean <i>RMS</i> wavefront error of significant aberration groups across the horizontal and vertical visual field.	72
3.13	Residuals wavefront of subject no. 14.	73
3.14	Distribution of the average residual <i>RMS</i> wavefront error in the horizontal and vertical meridian.	74
3.15	Three observed groups of the total <i>RMS</i> variation across the horizontal visual field.	75

3.16	Three observed groups of the residual <i>RMS</i> variation across the horizontal visual field.	77
3.17	Three observed groups of the total <i>RMS</i> variation across the vertical visual field.	79
3.18	Three observed groups of the residual <i>RMS</i> variation across the vertical visual field.	80
3.19	Horizontal and vertical meridians. Group mean <i>RMS</i> wavefront error for all eyes in the study divided into the three observed groups of aberration's field distribution.	81
4.1	Refractive index along the optical axis coordinate.	86
4.2	Schema of the three layers, which form the pre-corneal tear film.	87
4.3	Schematic illustration of tear film evolution on the corneal surface.	88
4.4	Two single Shack-Hartmann pattern images of subject <i>EG</i> , taken after 2 and 12 <i>second</i> from a single blink.	89
4.5	An example of the correlation assessment between distribution of the total <i>RMS</i> and pupil displacement <i>d</i>	91
4.6	An illustration of the " <i>tolerance</i> " window for the center of the pupil displacement.	93
4.7	Mean values of Zernike aberration coefficients obtained from an artificial eye.	93
4.8	Distribution of the selected data points, and the mean total <i>RMS</i> wavefront error along the 12 <i>seconds</i> time period after a single blink for 5 subjects.	95
4.9	Set of phase maps of Subject <i>EG</i> , including original, reference and residual wavefronts.	96
4.10	Distribution of the residual <i>RMS</i> wavefront error over 12 <i>seconds</i> of each experimental trial for each subject in our experimental group.	97
4.11	Evolution of the residual mean <i>RMS</i> wavefront error over 12 <i>seconds</i> for each subject in our experimental group.	98
4.12	Evolution of residual Zernike aberration coefficients (orders 2 nd , 3 rd , and 4 th) during 12 <i>seconds</i> after a single blink.	99
4.13	Distribution of the residual mean Zernike lower-order aberration coefficients.	100
4.14	Distribution of the combined, residual mean Zernike higher-order aberration coefficients.	101

4.15	Distribution of the mean, absolute values of the residual higher-order RMS wavefront error.	103
4.16	Group mean standard deviation (<i>SD</i>) of each subject for each Zernike aberration coefficient.	104
5.1	Inter-subject variability expressed as the mean standard deviation error for each Zernike aberration coefficient.	109
5.2	Mean standard deviation of each Zernike aberration variation for averaged over 5 field points in two meridians.	110
5.3	The mean Zernike defocus coefficient $c(2,0)$ plotted as a function of field angle (ω).	111
5.4	The mean Zernike astigmatism coefficient $c(2,0)$ plotted as a function of field angle (ω).	112
5.5	Mean coma components distribution in the two meridians.	113
5.6	The mean Zernike coefficients $c(2,0)$, $c(2,2)$ and $c(3,1)$ plotted as a function of field angle (ω).	114
5.7	Mean residual phase maps of the wavefront aberration for each subject.	119
5.8	The <i>PSF</i> images for each subject as a function of time elapsed after the blink.	120
5.9	An illustrative diagram showing possible factors and results of an uneven distribution of the tear film on the corneal surface.	121
5.10	Wavefront aberration distribution across the horizontal visual field for the eye no.14 and no.4.	123

Abbreviations

AE	Artificial eye
AO	Adaptive optics
cSLO	Confocal scanning laser ophthalmoscope
CCD	Charge coupled device
D	Diopters
FT	Fourier transform operator
FC	Field curvature
HOA	Higher-order aberrations
LOS	Line of sight
MTF	Modulation transfer function
n	Refractive index
OCT	Optical coherence tomography
PSF	Point spread function
RMS	Root-mean-square
SA	Spherical aberration
SD	Standard deviation
SH	Shack-Hartmann wavefront sensor
SLO	Scanning laser ophthalmoscope
TF	Tear film
ω	Field angle

Chapter 1

Introduction and Thesis

Synopsis

Human vision is very complex mechanism that includes a detection, registration and data processing stages. Even small imperfections in the optical system of the eye, can degrade the quality of vision. These optical imperfections are called ocular aberrations. It has been a long way for science community to uncover all the complexity of the optical system of the eye and a delicate photoreceptor layer as a detector. The nature of aberrations occurring in the human eye is complex mainly due to the lack of rotational symmetry of the eye, irregular shape of the cornea and gradient index structure (*GRIN*) of the crystalline lens. In light of this in order to create a new, realistic eye model, we should understand the origins of aberrations of the eye not only on-axis but also at the periphery of the field. However, after few hundred years of exploration of the eye and evolution of imaging, wavefront sensing and other ophthalmic instruments, the eye remains to be not fully understood. Even if we consider the modern imaging instruments with the ability of cross-sectioning of the retina layers *in vivo*, we come across some limitations in resolution. In this chapter we briefly introduce a history of the development of some important instruments for the investigation of the eye. We also present the synopsis of this thesis and a list of publications.

1.0.1 Simplified Historical Review of the Ophthalmic Instrumentation

The unremitting development of science and technology, especially medicine, causes a creation of a vast number of novelty instruments and techniques. The same applies to the science of human eye and vision. Simplifying the complex history of discoveries in the optics of human eye area, scientists, who lived at the turn of the 16th and 17th century such as Galileo, Kepler, Scheiner and Descartes initially started to treat the eye as an optical instrument. They provided the first description of the eye's optical components realizing, that the image on the retina was inverted [1,2]. The 17th century brought Christiaan Huygens, who, besides deriving the laws of reflection and refraction, built a physical eye model made of two hemispheres filled with water and a diaphragm [2,3]. It was not until the beginning of the 19th century that Thomas Young gave a geometric optics description of the cornea and the lens. However, the mentioned names include only famous astronomers, mathematicians and physicists, the number of bright researchers worked in this field was much greater. A great step forward, as it turned out, was the invention of ophthalmoscope by a German physicist Hermann von Helmholtz in 1850 [4]. This instrument is schematically shown in Figure 1.1(original illustration). It allowed observation of the details of the living retina and it was widely recognized as revolutionary invention in ophthalmology.

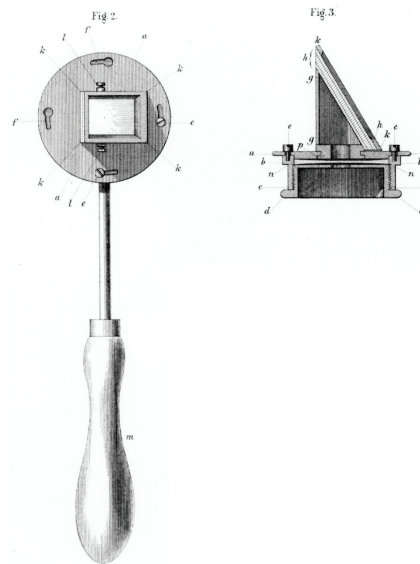


Figure 1.1: Helmholtz's ophthalmoscope. *Fig.2* (left side) - the instrument is viewed from in front, *Fig.3* (right side) - the instrument is exhibited in horizontal cross-section. Illustration adopted from [5].

Another milestone in the history of the investigation of the internal eye components was the development of the slit lamp biomicroscope. This instrument was not only important as an essential diagnostic tool in the clinic, but also served to greatly advance the scientific knowledge of the optical structure of the eye. The history behind this device started in 1820, when Jan Evangelista Purkinje applied an adjustable microscope to the iris examination in scattered light [5]. Several decades later, Louis de Wecker constructed a primitive version of unioocular slit lamp, with combined eyepiece, objective and adjustable lens. An improved version of de Wecker's instrument was proposed in 1899 by Siegfried Czapski, who added binocularity to the microscope and mounted it on the horizontal axis. However, it was still too early for these instruments to be clinically useful. The Swedish ophthalmologist Alvar Gullstrand (the Nobel price laureate in 1911), created a first true slit lamp to illuminate the eye. The modern slit lamp biomicroscope was born in 1910, when Henker and Vogt improved a Gullstrand's device by creating an adjustable slit lamp and combining Czapski's microscope with Gullstrand's slit lamp illumination. Figure 1.2, is an example of early slit lamp biomicroscopy from 19th century. It was a powerful tool capable of stereoscopically examining optical sections of the anterior segment in great detail.

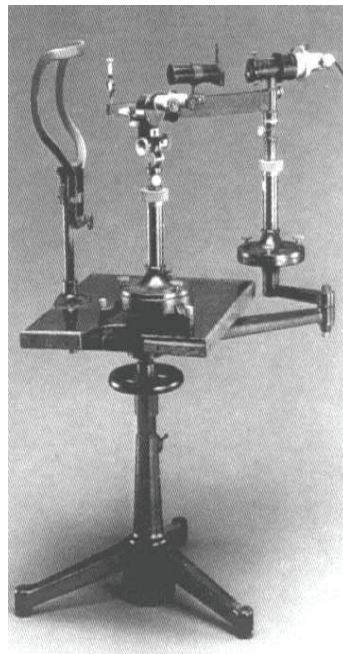


Figure 1.2: Gullstrand's slit lamp. The version shown with a corneal microscope, that was built at Carl Zeiss from 1916 onwards. Image taken from an electronic data base at <http://www.zeiss.de/>.

In considering the history of the development of ophthalmic devices, is important for understanding how long it took to form the ophthalmic devices to the current shapes and level of usefulness. We should bear in mind that there were much more inventions and individuals who spent their entire professional activity on this topic. Furthermore, the history of the human eye investigation is constantly running, and we are still looking for solutions for new tasks.

1.0.2 Modern Times

Classical ophthalmoscopes or slit lamps gave the origin for many modern instruments, that resemble their predecessors in name only. These are the scanning laser ophthalmoscope (*SLO*), that allows to obtain a high resolution images of the retina [6], and optical coherence tomography (*OCT*), which is an imaging technique based on interferometry [7]. Of course such techniques could not be developed without many important discoveries that the 20th century has brought with (e.g. the invention of the *LASER*). Another important development came from the field of astronomy. Adaptive optics (*AO*) was first proposed by Babcock in 1953, for compensating the aberrations introduced by the atmosphere in telescope images [8]. In the mid to late 1980s the astronomy community took advantage of the advancements made by the military in the field of adaptive optics. Technological developments in *CCD* detectors and deformable mirrors have given rise to a new era of aberration correction. It turned out, that applying the *AO* system to the correction of the aberrations of the human eye, one can get tangible benefits in terms of enhancing resolution of the retinal imaging process [9–11]. We should bear in mind that the evolution of wavefront sensing and aberrometry techniques was crucial for retinal imaging, and we shall give a brief description on other techniques in Chapter 2.

The aberrations of the eye limit any optical system imaging the eye *in vivo*. Not surprisingly, the adaptive optics has been combined with other techniques in order to improving the resolution of retinal images down to almost the diffraction limit. In 2002 *AO* was combined with the confocal scanning laser ophthalmoscope (*cSLO*) by Roorda *et.al* [10]. Integration *AO* into *cSLO*, gave a benefit in enhanced resolution (up to about 3 μm) and field of view up to 3 degree. About year later, *AO* was implemented in optical coherence tomography (*OCT*) by Miller and colleagues [12]. This resulted in improved resolution being axially around 3 μm and from 5 to 10 μm transversally [13]. In 2009 Torti and colleagues, using the *AO-OCT* optical set-up, reached even better resolution level of 2 μm axially and about 2.7 μm of transverse resolution [14]. More

detailed description of the *OCT* technique and its applications may be found here [15]. An adaptive optics system can also act as a visual simulator, when the impact of ocular aberrations on the visual performance is measured [16–18]. There are still ongoing effort to make imaging systems with *AO* more commercially achievable, however a classical, direct ophthalmoscope is still an indispensable tool for initial investigation of the eye. Figure 1.3 shows an example of the retinal image from one of the commercial instrument with the *AO* system onboard.

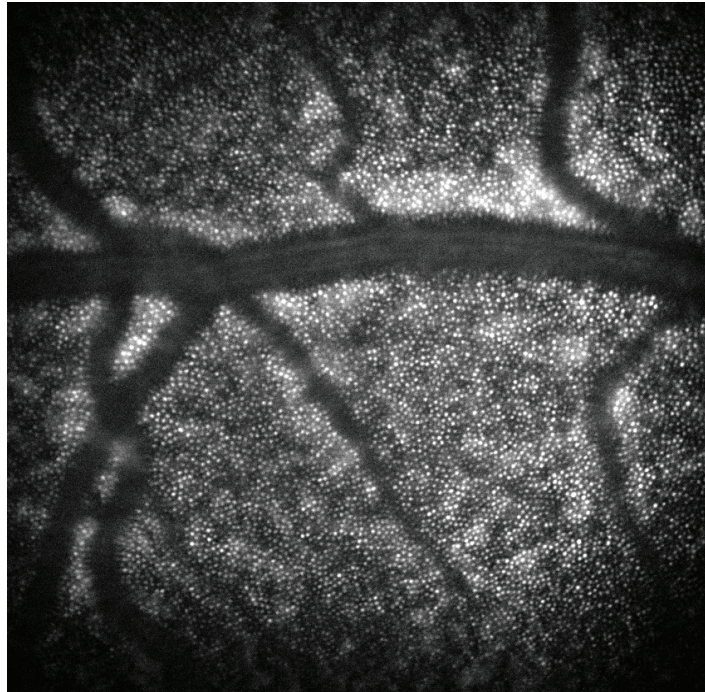


Figure 1.3: Image of the retinal photoreceptor cells (4×4 degree) of author, taken with an Adaptive Optics Retinal Camera, at the Imagine Eyes Company, Orsay, France. Thanks to Barbara Lamory.

1.0.3 Thesis Synopsis and Publications

Chapter 2 provides the background information related to the human eye and its optics. A general description of the optics and physiology of the eye is given here, with an emphasis on the axes of reference. Next a review of existing models of the eye is presented and a brief description of the main features during their developing is also given. Next, since we treat an eye as the independent optical system, we give a basis principles of aberration theory, followed by a more detailed overview of different kind of the optical aberrations, then we describe how the aberrations are

commonly quantified using Zernike polynomials. We show different metrics to quantify the optical quality of any optical system with reference to the human eye. Finally, an overview of common techniques used in wavefront sensing is given.

Chapter 3 presents our measurements of the off-axis, 10×10 degree visual field. We present here our optical set-up and experimental procedure that we used to examine 25 healthy eyes of 25 individuals from the young population. We show how the aberrations of the wavefront, measured with a dedicated Shack-Hartmann (*SH*) wavefront sensor (*WFS*) in the pupil plane of the eye and expressed in Zernike polynomials, are distributed along horizontal and vertical meridian of the visual field. Our attempt to understand the origin of inter-subject variability in terms of the *RMS* wavefront error distribution and estimation of the size of the averaged isoplanatic patch is also shown in this Chapter.

Chapter 4 focuses on the experimental assessment of the optical effect of tear film variation after blinking in young healthy eyes. Here we present a statistical analysis, based on an experimental data, gathered from 5 young subjects. Results we display here, show decomposition of some single Zernike aberration terms and groups mainly inducted by the evolution of the tear film layer on the front surface of the cornea after a single blink.

Chapter 5 concludes on the work presented in this thesis and discusses the origins of some types of ocular aberrations. Finally, we give here an outlook for further investigations and possible improvements in realism in eye modeling.

Publications

- A. V. Goncharov, M. Nowakowski, E. Dalimier, M. Sheehan, and J.C. Dainty. A study of field aberrations in the human eye. In *Proceedings of 6th International Workshop on Adaptive Optics for Industry and Medicine*, Galway, Ireland, 6:293-298, 2007. , Galway, Ireland, 6:342-347, 2007.
- A. V. Goncharov, M. Nowakowski, M. T. Sheehan, and C. Dainty. Reconstruction of the optical system of the human eye with reverse ray-tracing. *Optics Express*, 16(3):1692-1703, 2008.

Chapter 2

Background for the Study

Most optical imaging systems suffer from aberrations and the human eye is no exception. The optical system of the eye contains three main components: the cornea, the iris, and the crystalline lens. The cornea is responsible for roughly two thirds of the total optical power of the eye and hence it is one of the two major contributors to the total aberrations of the eye. The corneal shape is usually aspheric without rotational symmetry, which gives rise to astigmatism, trefoil coma and some other higher-order aberrations. The crystalline lens is the second major contributor to the aberrations of the eye, especially in view of its gradient index nature (*GRIN*). Understanding the optical properties of the eye with all decentrations, misalignments and asymmetries of the optical surfaces is of a main goal of research on the optics of the human eye.

In this Chapter we provide the background information about the optics and physiology of the eye. We discuss the different approaches and the properties of existing models of the eye. We also give an overview of the aberration theory with an emphasis on the Zernike polynomials, which are commonly used to quantify ocular aberrations. Next, we show different metrics of the quality of any optical system with reference to the human eye. Finally, an overview of common techniques used in wavefront sensing is given.

2.1 Optics and Physiology of the Eye

The eye enables us to view an external world. From the optical point of view it works like a photographic objective creating an image with a focusing mechanism allowing the eye to adjust its optical power. The optical system of the eye has four distinctive refractive surfaces: anterior and posterior surfaces of the cornea and the crystalline lens. The optical power K for each optical interface is proportional to the change in refractive index and inversely proportional to the radius of curvature r , as showed an eq. 2.1

$$K = \frac{(n_2 - n_1)}{r}, \quad (2.1)$$

where n_1 and n_2 are the refractive indices of the first and latter optical medium respectively. The accumulative effect of all surfaces and gradient index distribution in the lens determine the imaging properties of the eye.

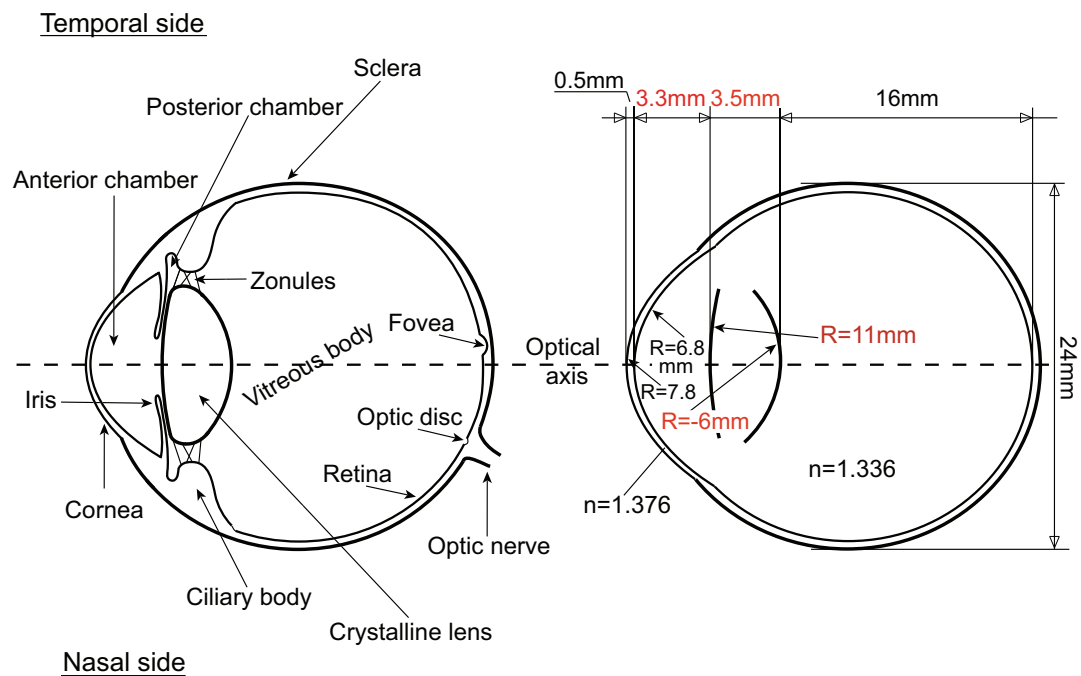


Figure 2.1: Schematic layout of the right eye. The values given in red depend upon accommodation. Note, that this is a schematic of a typical adult eye and some of values exhibit large inter-subject variability (see [19, 20] for more examples).

For a better understanding of the image formation in the optical system of the eye, we consider its characteristics more closely. Figure 2.1 presents the physiological components and representative dimensions together with the refractive indices of the right

eye, based on [1]. When the rays of light are entering the eye, they first hit a thin layer of the tear-film, which has a refractive index of approximately 1.337 at $589 \mu\text{m}$ wavelength [21]. For clarity, in this section we will use the wavelength of $589 \mu\text{m}$ for refractive indices of other components of the eye. This thin layer of liquid (3-8 μm thick [22]) consists of three tear layers: mucus, aqueous and oil, where 98% of the total thickness is supplied by the aqueous layer. It provides a smooth layer on the cornea and prevents light scattering on the rough surface of the epithelial cells of the cornea. The tear-film does not contribute significantly to the refractive power compared to the rest of the optical components. However, it plays a significant role in clear vision. We will describe it in more detail later in Chapter 4.

After the tear film, ingoing rays enter the cornea. It is defined by the anterior and posterior surfaces. The typical central thickness is 0.55 mm with the bulk consisting mainly of a pattern of parallel fibers, with refractive index of about 1.376 [23]. The radius of curvature of the front surface of the cornea is not constant as it increases toward the corneal periphery, however at the vertex it reaches the value of about $7.8 \pm 0.25 \text{ mm}$ [24]. In terms of the optical power the cornea is the strongest component of the eye. It refracts the light with the power being around 42 dioptres (D) [1], although this includes the power of the front and back surfaces. Figure 2.1 shows typical values for the radii of curvatures of the corneal surfaces, to a first approximation modeled as spheres. In reality, neither the anterior nor the posterior surfaces are perfectly spherical due to both toricity and asphericity. Therefore, the radii of curvature do not fully describe the shape of the cornea and its refracting properties. The asphericity is required to estimate the aberrations for each ocular surface.

After the cornea light enters the anterior chamber with an axial depth of about 3.3 mm . It is filled with the aqueous humor, a clear liquid, which supplies nutrition and oxygen to the cornea and the lens. The aqueous humour, with a refractive index of 1.336, also surrounds the lens and fills the vitreous body, and the amount of liquid governs the intraocular pressure of the eye [23].

The next element in the optical system of the eye, acting like an aperture stop, is the iris. The image of the iris in the object space is known as the entrance pupil, which usually varies from 2 to 8 mm in diameter, although it may be artificially dilate by using parasympatholytic eye drops (such as *Tropicamide*, *Cyclopentolate* [25]). To control the size of the pupil, the iris contains muscle fibers in two orientations: radial fibers, which dilate the pupil and circular fibers, which decrease the pupil diameter [23]. The most important factors affecting the pupil size are the level of illumination and age. In the case of perfect rotationally symmetric optical system, the pupil is always

located on axis. However, the pupils of real eyes are usually decentred, often being displaced less than 0.5 mm relative to the visual axis [26], and moreover, the center of the pupil may be shifted up to 0.6 mm after pupil dilation in the nasal or temporal direction [27].

Passing the opening in the iris the rays of light are refracted gradually in the crystalline lens. The lens is contained within a capsule, which is essentially a transparent elastic bag attached to the ciliary body by the zonular fibers. Contraction of the ciliary muscle within the ciliary body leads to changes in zonular tension, which alter the lens shape. This mechanism, so-called accommodation, allows the eye to focus on objects at different distances [28]. Optically the crystalline lens is a biconvex, gradient index lens with an equatorial diameter between 8.5 and 10 mm and thickness of about 3.5 mm (relaxed state, depending on the age) and the unaccommodated refractive power of $+21\text{ D}$. The range of accommodation is about $+15\text{ D}$ at birth and diminishes during life as the lens becomes more rigid. By the age of 60 there is almost no accommodation left; this condition of an aging eye is called presbyopia [23]. The crystalline lens consists of onion-like layers with soft cortex around a harder nucleus. The crystalline lens grows throughout life as new layers are continuously added to the cortex. The refractive index within the lens is not constant, it increases gradually from the periphery towards the core from about 1.36 to 1.41 at $555\text{ }\mu\text{m}$ wavelength [29]. Together with the iris it is the only adjustable part of the eye.

Finally the image is formed on the retina [30], which is a light sensitive tissue directly connected to the brain (in fact the retina is an extension of the nerve fibers of the brain). The image created on the retina is sampled by the photoreceptors organized in hexagonal mosaic. We can divide the photoreceptors into two classes: rods and cones. Rods are cells highly sensitive to light of any wavelength in the visible range. The number of rods is between 110 and 125 million in the human retina with a typical diameter of $1.5\text{ }\mu\text{m}$ [31]. The highest density of 160 000 per mm^2 (equivalent to a centre-to-centre spacing to of about $2\text{ }\mu\text{m}$) is found at 20 degree from the fovea [32]. Cones are cells capable of color detection, but less sensitive to low intensities thus they give us with color vision with high resolution when the luminance is sufficient. The number of cones cells is ranged between 6.3 and 6.8 million in the retina [31]. There are three different types of cones in the eye, and these are responsible for different spectral ranges of visible light: *S*-cones (short-wavelength photoreceptors, with a spectral sensitivity highest for blue light) *M*-cones (green light) and *L*-cones (long-wavelength photoreceptors, red light). The total amount of cone cells in the retina is about 20 times less than rod cells. However they are mainly concentrated in the

fovea, which is a shallow depression region in the retina with diameter of 1-2 *mm*, corresponding to a visual field of about 5 *degree*. The center of the fovea, the foveola, contains only cones, up to 150 000 per mm^2 and thus it provides the highest quality of vision in terms of angular resolution and contrast [23].

2.1.1 Axes of Reference in the Eye

Most manufactured optical systems have rotationally symmetric components. In cases when the reflecting and refracting surfaces are spherical and aligned centered optical systems, there is the unique line joining the centres of curvatures of these surfaces, so-called the optical axis. Of course there are many different systems with, for example, two planes of symmetry (astigmatic or toroidal components), but still we can plot the line intersecting of these two planes thereby defining the optical axis. As it was mentioned earlier, the eye is not a rotationally symmetric optical system thus the optical axis is not uniquely defined. Despite the lack of symmetry, one can introduce a number of axes and consider some idealized properties of the eye. We are going to look at various axes of reference and the important cardinal points.

In 1841, Gauss demonstrated, in his famous treatise on optics, that for paraxial rays a lens of any degree of complexity can be represented by its cardinal points: 2 principle points and two focal points (see Fig. 2.2, case (a)). In 1845, Listing introduced the concept of nodal points (having unit angular magnification) for his simple model of the eye. The reason for considering the nodal points is simple; if refractive indices on both sides of the lens are not the same then the nodal points are not coincident with principle points (see Fig. 2.2, case (b)). This is true for the case of the human eye.

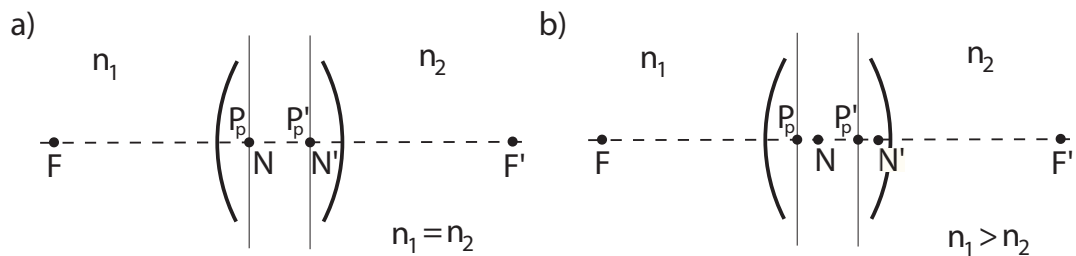


Figure 2.2: The cardinal points of the single lens: P_p, P'_p -principal points, N, N' - nodal points, F, F' - focal points. (a)- Gauss model with $n_1 = n_2$ assumption, (b)- Listing general approach for $n_1 \neq n_2$.

Figure 2.3 presents the visual axis together with the idealized optical axis. The ide-

alized optical axis is the line, which contains the centres of curvature of all optical surfaces of the eye and passes the pupil at the center E . A real eye is not a centred system, thus the the optical axis does not exist. However to have a reference for other axes we can define the optical axis of the eye as the line of "best fit" through the centres of curvature of the "best fit" spheres to each surface [1]. The visual axis connects the fixation point P to the front nodal point N , and the rear nodal point N' to the foveal point P' . The sense of the nodal points in optical system is such that a ray entering the front nodal point N , exits the system parallel to the incident direction through the other nodal point N' [33]. It can be clearly seen that this visual axis is rather theoretical in the eye, since it is not possible to define a straight line that goes through all four points (P, N, N' and P'), yet it defines the direction of fixation.

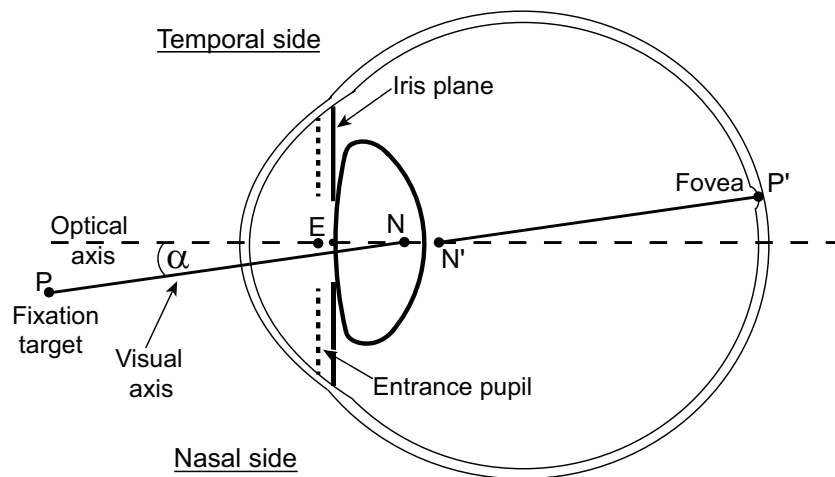


Figure 2.3: The optical and visual axes of the eye. The optical axis (dashed line) connects the centres of curvature of all optical surfaces, crossing the entrance pupil at the midpoint (E). The visual axis contains the fixation point (P), front and the rear nodal point (N and N'), and the foveal point (P').

The angle between the visual axis and the optical axis is called the angle alpha (α) and is often assumed to be about +5 degree horizontally (i.e. the fovea is shifted from the optical axis in the temporal retina), but is usually in the range +3 to +5 degree (however, Marcos *et al.* measured an even wider variation, from 2 up to 7.4 degree [34]). The visual axis is also downwards relative to the optical axis by 2-3 degree [1, 35].

The pupillary axis, depicted in Figure 2.4, is defined as the line that is normal to the cornea and passes through the center (E) of the iris and exits through the corneal center of curvature C . If the eye was a centred optical system, the pupillary axis would coincide with the optical axis. However in reality, the pupil is often shifted nasally

relative to the optical axis and the front cornea may not be a regular surface. Navarro showed that for young eyes the corneal front surface is tilted by 2 degree midway between optical axis and line of sight [35]. Taking into account these findings it is evident that the pupillary axis lies in some other direction, and in general it does not pass through the fixation point (P). From a point of view of ocular aberrometry and wavefront sensing, the line of sight (LOS) is the most important axis, since it is the preferred reference axis for analysis of the ocular aberrations. It goes from the fixation point P to the center of entrance pupil E . In other words the LOS axis defines the centre of the beam of light entering the eye. However it is not fixed as the pupil center may vary due to fluctuation in the diameter of iris opening [1]. The angle between the pupillary axis and the LOS axis is usually denoted as lambda (λ). It is important to emphasize here that angle λ is sometimes confused with angle kappa (κ)(see Fig. 2.4 for reference), which is the angle between pupillary and visual axes. Taberner *et al.*, based on an instrument recording reflections of light from different ocular surfaces (Purkinje images), showed that an average value of angle kappa for a typical eye is around 5 degree [36]. This result lies within the average range for angle kappa values of 1.4 degree and 9 degree, reported in earlier work of Mandell [37].

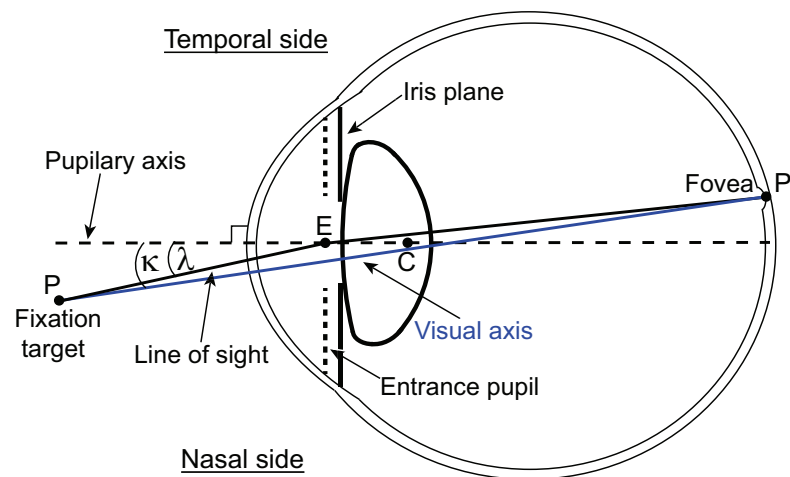


Figure 2.4: The line of sight and pupillary axes of the eye. The line of sight connects the fixation point P to the foveal point P' , going through the center of the entrance pupil E . The pupillary axis (dashed line) is the line normal to the corneal surface, containing the center of the entrance pupil E and the corneal center of curvature C . The angle between the pupillary and the LOS axes is denoted as lambda (λ). It also shows the angle between the pupillary and the visual axes (solid blue line) usually denoted as kappa (κ).

The importance of estimating angle kappa arises when a combination of different

methods is used to measure corneal and internal aberrations of the eye (e.g. videokeratoscopes are often not aligned with the line of sight but aberrometers usually are [38, 39]). A paper published in 2002 by Salmon and Thibos emphasized this problem with the conclusion that the misalignment between both axes (if ignored) can significantly affect the final results of corneal and internal aberrations measurements [38]. A recent study by Navarro *et al.* gave another measure of the eye mismatch properties, since there is about 2.3 *degree* between the optical axis and the "*keratometric*" axis which is close to the *LOS* axis [35].

2.2 Mathematical Models of the Eye

There has been extensive work done by many researchers on developing realistic models of the human eye. Many scientists and optical designers showed various approaches to this topic and a lot of theoretical models have been defined for many of different purposes. The wide range of schematic eyes can be used for better understanding of the role of different optical components: designing of ophthalmic and imaging instruments, simulating the refractive surgery outcomes or finding the optimal optical power for intra ocular implants. Although the idea of a perfect universal eye model is attractive, it is unlikely that such a model could be created in practice. The problem arises from the fact that the data for a real human eye are scattered around mean values in a broad statistical distribution. Therefore we shall develop task-specific and customized models, which can be implemented to predict ocular aberrations of a given subject.

The first model operating on-axis and reproducing the Gaussian properties of an average eye was the famous "*No. 1*" Gullstrand's model [40]. It consists of six refractive surfaces assumed to be spherical and centred on a common optical axis. The gradient index structure of the crystalline lens was modeled by two concentric shells with a different index of refraction in which the inner shell (nucleus) had a higher refractive index than the outer shell (cortex). Using the Gullstrand model, Le Grand and El Hage replaced the shell structure of the lens for a homogeneous index lens [41]. Although this model has been accepted and widely used they concluded that using so-called reduced eye models might be inaccurate in some cases and should be treated as a first approximation. Other paraxial models have been developed such as Emsey's reduced eye [42], Thibos's "*Indiana*" model [43] or Bennett's model [44] which provided good prediction for some ocular aberrations. However, the main goal for all reduced models is to describe the paraxial properties of the eye by the corresponding

radii, axial distances and refractive indices.

Apart from rather simplistic models mentioned above some authors considered anatomical characteristics of the eye more carefully. In order to create models with better agreement with experimental data, aspheric surfaces and a crystalline lens with a varying refractive index have been proposed.

We can divide the models with a complex lens structure into two main groups. First group consists of schematic eyes with the lens represented by a finite number of concentric shells differ in index of refraction in which Gullstrand's exact model is a first attempt. Lotmar proposed the lens composed of seven shells with increment of refractive index of 0.005 [45]. In the shell-model lens of Pomerantzeff *et al.* we can find 398 layers with different indices, radii of curvature and thickness [46], whereas Al-Ahdali and El-Messiery designed an eye model consists of 300 spherical shells in the lens I [47]. More recent Liu *et al.* extended this approach incorporating 602 ellipsoidal shells in order to achieve anatomically close schematic eye [48].

The second group constitutes eye models with a continuous distribution of refractive index, so-called gradient index (*GRIN*), which is usually described by a set of equations. Such a mathematical representation of a gradient index of the lens avoids the effect of multiple foci [49], which comes from the noncontinuous structure of the shell lens. Several models using the idea of the *GRIN* lens have been created such as: Blaker's model [50], Smith *et al.* aging eye [51], Liou and Brennan's model [29], Goncharov's wide-field eye model [52], and the aging eye model of Navarro and colleagues [53]. The shell-lens and the *GRIN* models are described with a more details in the work of Smith [54].

Another factor that can specify the usage for some models is their ability to predict ocular aberrations not only on-axis but also off-axis, the so-called field aberrations. Wide field models are of great importance when imaging the peripheral retina. Furthermore, creating off-axis capable models of the eye, one can discover more about the origin and nature for some types of ocular aberrations. Lotmar proposed, based on Gullstrand's schematic eye, a model containing aspheric surfaces at the front of the cornea and the back of the lens [45]. Lotmar's model was able to predict astigmatism and coma up to the visual angle of 90 *degree*. The work of Wang and Thibos [55] suggested a way to mimic off-axis astigmatism, chromatic aberration and spherical aberration by using a reduced-eye model with a single elliptical refracting surface [56]. Another well-known wide-angle model is the one from Escudero-Sanz and Navarro [57]. It was an extended version of previously proposed on-axis model

of Navarro [58] and with similar idea to Kooijman’s wide-angle schematic eye [59]. The Escudero-Sanz and Navarro’s model using four conic surfaces and constant refractive index lens gives a prediction of all monochromatic aberrations off-axis up to 60 degree in the field. Using predictions of this model, Goncharov and Dainty replaced the lens by an adaptive GRIN lens with age-dependent shape [52]. Such a wide-field model was used as the basis for personalized eye model [60]. Figure 2.5, presents a schemataic tree of eye’s models development. More detailed reviews of those and other schematic eye models can be found in [61,62].

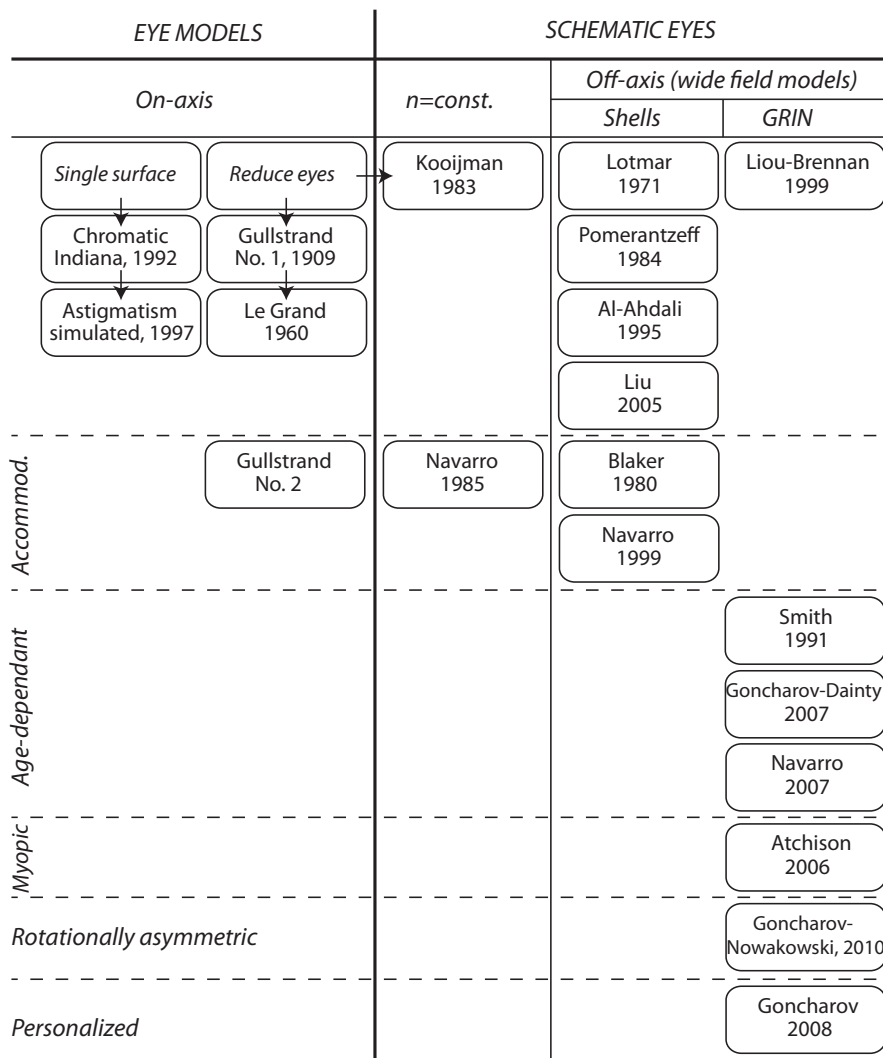


Figure 2.5: Schematic tree of the development of the eye models.

2.3 Monochromatic Aberrations of the Optical Systems

It is well-known that the perfect optical systems do not exist in real life. In other words there is no such a system which is able to create the perfect image of an object. There are various reasons that prevent the perfect image formation, among which we can distinguish the most important three:

- Geometrical aberrations. The rays of light coming from a point in object space do not come together in the same point in image space after they pass the optics of the system. Furthermore, even if the system could give one point for incoming rays it may be not exactly at the image plane in the case when the system is ideal.
- Diffraction on the aperture stop and edges of optical elements. In this case the ideal image of a point in the object plane is given by the diffraction pattern in the image plane (Airy disc). The Airy pattern occurs even when the object point is formed by an aberration-free system, so the system is diffraction limited. Very often some information is lost due to apertures and stops in the optical setups which may filter out some spatial frequencies.
- Scattering, which means deflection of photons by small particles within an optical medium. In the eye scattering results in contrast degradation. However the eye has several tools to fight the scattering of the light, e.g. the tear-film on the cornea, the uveal tract (pigmented tissue consisting of iris, ciliary body and choroid) which absorbs the scattered light. From the other hand, some eye diseases, like cataract for instance, can significantly create new sources of light scattering. Solving this problem is of great importance for retinal imaging quality.

We can use two mathematical tools that describe geometrical and wave-optics. These are rays of light and waves (wavefronts). The well known today concept of geometrical wavefront was firstly introduced in early work of Fermat (1667), then Malus (1808), Hamilton (1820-30) and others. The wavefront is described as a surface of constant optical path from the source (or surface that merges all points with the same phase in the physical meaning). The surface of the wavefront is always orthogonal to the rays from a source point [63].

As an example of geometrical aberrations let assume that there is an optical system with a point P in the object plane. From this point the wavefront, which is approaching the optical system is a perfect sphere however after it passing the system the shape of the wavefront is not a sphere any more. Figure 2.6 illustrates this situation where three rays departing from an off-axis point P in the object space do not intersect the image plane exactly at the same point. This is the appropriate place to mention the role of stops and pupils in optical systems. Logically all stops put some limitations within the optical systems, and more specifically the aperture stop limits the amount of light entering the optical setup while the field stop limits the extent of the image or, in other words, field of view (the human eye is an example of the optical system that does not have a definite field stop). The extent of the functional retina limits the field of view and vignetting. The aperture stop is usually physically inside an optical system and its image in object space is called the entrance pupil EP and exit pupil EP' in the in image space (see Figure 2.6). It is worth noticing here that, in spite of mutual conjugation of object and image planes, the aperture stop plane is conjugated with both pupil planes (entrance and exit) as so entrance and exit pupils are mutually conjugated as well. In general, pupils are good locations for deformable mirrors or filters and the reason is that the pupil contains all the rays taking part in the image reconstruction, whatever the field angle.

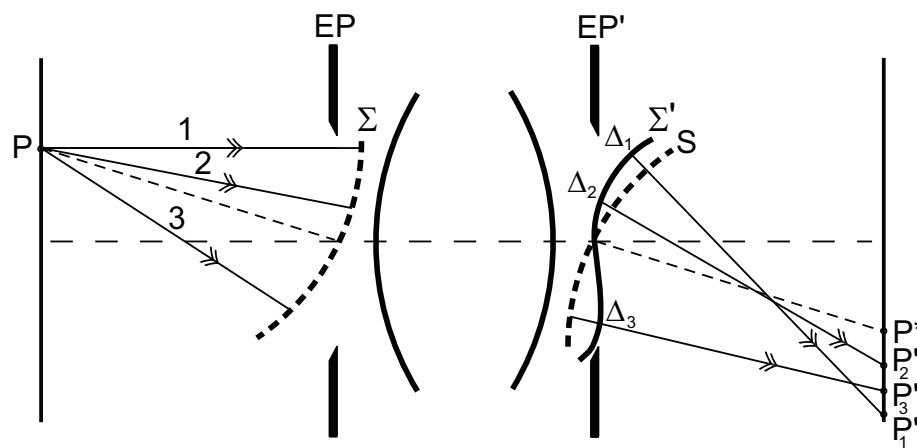


Figure 2.6: A simplistic sketch of an imperfect optical system. Three rays (1, 2, and 3, which are outgoing from an object point (P), go through the entrance pupil (EP) and the exit pupil (EP') of the optical system. In the presence of aberration the current wavefront (Σ') is deformed and differs from the hypothetic perfect wavefront (sphere (S)). Note, that the chief ray (the ray, that goes through the centres of (EP) and (EP'), shown by a dashed line) indicates location of the perfect image point (P^*), which is the center of curvature for the perfect sphere (S).

In the case of a perfect imaging system point P^* would be an image of point P and corresponding shape of wavefront would be a perfect sphere centered on P^* in the image space. Due to aberrations in the system, the rays intersect the image plane at various points: P'_1, P'_2, P'_3 . The aberrated wavefront Σ' (shown by the solid line) is perpendicular to these rays. Three lengths ($\Delta_1, \Delta_2, \Delta_3$), plotted in Figure 2.6, represent distances between the real, aberrated wavefront Σ' and a reference sphere S with the centre of curvature located at P^* . This optical deviation of the wavefront from a reference sphere measured along the optical path of rays is defined as wavefront aberration W [63]. Different locations of P'_1, P'_2, P'_3 from a reference point P^* at the image plane expressed as $\delta l'_i = \overline{P'_i - P^*}$ for ($i = 1, 2, 3, \dots$) are called: transverse or lateral aberrations of the ray.

Reconstruction of an aberration's pattern of an optical system can be achieved by finding the transverse ray aberration expressed as discrete optical path differences at various locations within the pupil. To illustrate this, we shall trace a single ray coming from an exit pupil and intersecting the image plane. Figure 2.7 depicts this case with the reference sphere S (sphere of the constant phase) containing the center of the exit pupil P_0 and with the center of curvature positioned at the point P'_0 of the image plane.

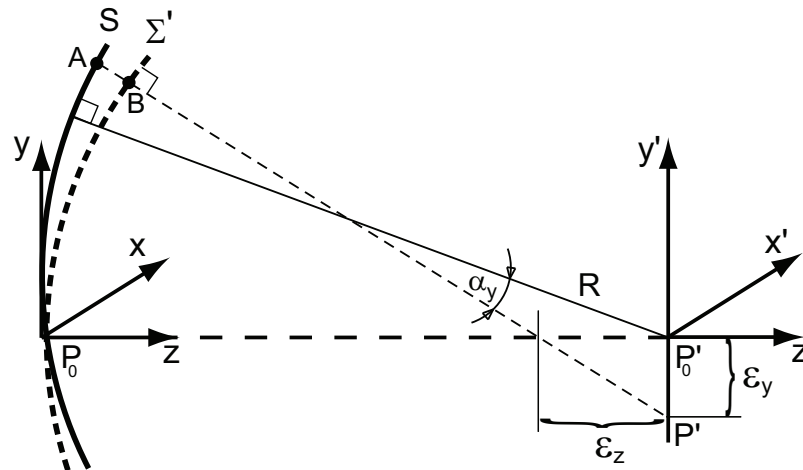


Figure 2.7: The geometrical aberration of the ray: transverse (ϵ_y), longitudinal (ϵ_z), and angular (α_y). The Z axis is the optical axis of the system. Sphere S depicts the reference sphere with a center of curvature located at point P'_0 in the image plane. The aberrated wavefront Σ' , deviates from the sphere S by the quantity of AB and hence, aberrated ray comes to the image plane at different location (point P').

Sphere Σ' (dashed line) displays a local deviation from a reference sphere S and hence an aberrated ray hits the image plane at different location (point P'). Because different regions of aberrated wavefront come to focus at different locations instead of a unique focus there is a small circle that confines all aberrated rays intersecting the paraxial image plane. The maximum deviation at the point $y'_0 = -\epsilon_y$, gives the amount of transverse aberration.

Assuming that the angle between an aberrated ray and the optical axis (z) is sufficiently small, we can approximate its sine by the angle itself, and the cosine of the angle by unity. The distance AB (Figure 2.7) is related to the wave aberration $W(x,y)$. In ophthalmology is also called wavefront aberration. In order to obtain the optical path we multiply the distance by the refractive index n of the propagation media:

$$W(x,y) = ABn. \quad (2.2)$$

It is assumed as well, that $W(x,y)$ is sufficiently small and the angle α_y is also small so using derivatives of $W(x,y)$ with respect to y (in the pupil plane) we can express α_y , as:

$$W = \frac{-\delta W(x,y)}{n\delta y}, \quad (2.3)$$

where n stands for the refractive index of the image space. This is the expression for the angular resolution. By using Eq. 2.3, we can find two components for transverse ray aberration:

$$\epsilon_y = R\alpha_y = \frac{-R\delta W(x,y)}{n\delta y}, \quad (2.4)$$

and

$$\epsilon_x = R\alpha_x = \frac{-R\delta W(x,y)}{n\delta x}, \quad (2.5)$$

where R is the radius of curvature of the reference sphere at point P'_0 . Following Wyant [64] and Gross [33] we can also write:

$$\frac{\epsilon_z}{\epsilon_y} \approx \frac{R}{y - \epsilon_y}, \quad (2.6)$$

and since $\epsilon_y \ll y$, we are able to find longitudinal aberration ϵ_z which is given as:

$$\epsilon_z \approx \frac{R}{y}\epsilon_y = -\frac{R^2}{y} \frac{\delta W(x,y)}{n\delta y}. \quad (2.7)$$

Analytical expression for transverse and longitudinal aberration of the ray allow us to find some useful tools for representing the aberration function. For example, if

the exit pupil coordinates are expressed in normalized coordinates such that $(x^2 + y^2)^{1/2} = 1$ at the edge of the exit pupil, the transverse and longitudinal aberrations can be easily written as:

$$\epsilon_y = -\frac{R}{h} \frac{\delta W}{n \delta y} \quad (2.8)$$

and

$$\epsilon_z = -\frac{R^2}{yh^2} \frac{\delta W}{n \delta y} \quad (2.9)$$

where h represents the geometrical pupil radius. Using Eq. 2.8 and Eq. 2.9, we can easily calculate transverse and longitudinal aberration from wavefront aberration W , which is usually measured by a wavefront sensor. Furthermore, knowing the position of each ray, in a given coordinate system, we can simply obtain a graphical representation of the aberration function such as ray-intercept curves or spot diagrams. Describing the geometrical image quality by lateral aberrations or spot diagrams is commonly used method for aberrated system with resolution far from the diffraction limit [33]. It is also possible to calculate the wavefront aberration based on the transverse ray aberration. As long as we know ϵ_x and ϵ_y as functions of x and y for some locus across the reference sphere, for instance, from A to B , then from Eq. 2.4 and Eq. 2.5, we can write:

$$\frac{R}{n}(W_B - W_A) = -\int_A^B \{\epsilon_x \delta x + \epsilon_y \delta y\}, \quad (2.10)$$

where the path of integration is from A to B . Measuring the wavefront aberration $W(x,y)$ is the method of choice for describing the image quality of good optical system (close to diffraction limit). More detailed description of geometrical and wavefront aberrations can be found here [63,65].

2.3.1 Polynomial Representation of Aberrations

Following our discussion of finding the aberration of a single ray or wavefront aberration, we shall consider now other methods describing different types of aberrations, which may occur in an optical system. Let us assume a ray coming from point P in the exit pupil to the point P' at the image plane (see Figure 2.8). As we showed earlier the wavefront aberration depends on the pupil coordinates (x,y) or in polar system. Because we are still describing wavefront aberration in a rotationally symmetric optical system, $W(x,y)$ or $W(\rho,\theta)$ has to be invariant to rotation. To fulfill this condition, we shall find all combinations of the pupil and image space coordinates that are rotation

invariant. Such combinations are:

$$x^2 + y^2, xx' + yy', (x')^2 + (y')^2. \quad (2.11)$$

Using the rotational symmetry of the system we need to consider only image points along the y' axis. To do so, we set $x' = 0$ and our wavefront aberration is now a function of:

$$W = W(x^2 + y^2, yy', (y')^2). \quad (2.12)$$

From Figure 2.8, one can see that it is convenient to specify the pupil coordinates by polar coordinates (ρ, θ) , where:

$$\rho = \sqrt{x^2 + y^2} \quad \text{and} \quad \tan\theta = \frac{x}{y} \quad (2.13)$$

$$x = \rho \sin\theta \quad \text{and} \quad y = \rho \cos\theta, \quad (2.14)$$

and therefore we can re-write Eq. 2.12 as:

$$W = W(\rho^2, \rho y' \cos\theta, (y')^2). \quad (2.15)$$

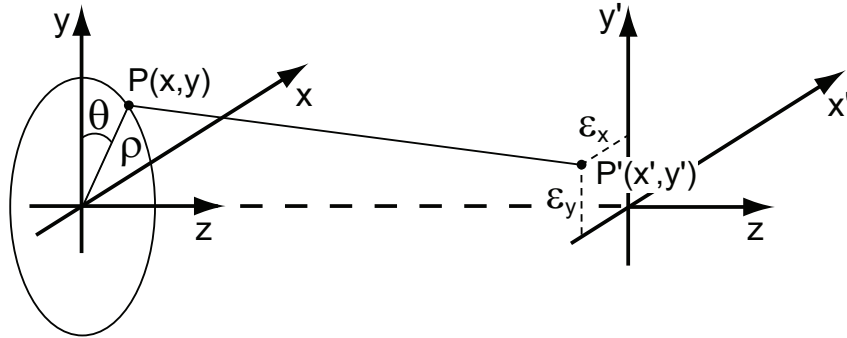


Figure 2.8: Polar coordinates in the exit pupil. The Z axis is the optical axis of the system. A single ray intersects the exit pupil plane at point $P(x, y)$ and hits point $P'(x', y')$ in the image plane. Quantities denoted as ϵ_x and ϵ_y are components for transverse ray aberration.

Now using these three variables from Eq. 2.15, for a point $P(\rho, \theta)$ at the pupil plane and a point $P'(x', y')$ at the imaging plane (assuming $x' = 0$) we are able to express

the aberration function as:

$$\begin{aligned}
 W(\rho^2, \rho y' \cos \theta, (y')^2) = & A(y')^3 \rho \cos \theta \\
 & + B(y')^2 \rho^2 \\
 & + C(y')^2 \rho^2 \cos^2 \theta \\
 & + D y' \rho^3 \cos \theta \\
 & + E \rho^4
 \end{aligned} \tag{2.16}$$

These five components are called primary aberrations or Seidel aberrations as a tribute to German mathematician, who gave an explicit formula for calculating wavefront distortions from paraxial ray-tracing parameters. Coefficients A , B , C , D , and E (also called Seidel's coefficients) depend only on the optical system parameters such as radii of curvature of refracting surfaces, refractive indices, and the positions of the aperture stop. As the primary aberrations are usually dominant factors that limit the image quality, we shall focus on their properties. In the following section we shall describe these primary aberrations in more detail.

2.3.2 Primary Distortion

Distortion appears in Eq. 2.16 with the coefficient ($A \neq 0$) and it is clear to see that it varies as the cube of the field angle. Figure 2.9 shows influence of the distortion of an object and the corresponding aberrated wavefront.

Distortion aberration is the aberration of the chief ray i.e. the ray, which goes from the edge of an object and passes through the center of an aperture. Therefore the distortion is strongly dependent on the location of the aperture in an optical system. For systems suffering from distortion, an object point is imaged as a point, but displaced with respect to Gaussian image point P^* of an ideal system. Therefore as a wavefront aberration, distortion results from the actual wavefront being formed tilted with respect to a perfect reference sphere. The quality of the image is not affected in presence of the distortion, however the image scale is deformed across the image field.

In the Seidel approximation, one has the positive (pincushion) distortion or negative (barrel) distortion as shown on Fig. 2.9. Optical systems with corrected distortion term are called orthoscopic. In a simple case shown in Figure 2.9, we introduce barrel-shape distortion whereas the pincushion type appears when the stop aperture is placed between the lens and image plane. The chief ray (showed as dashed line),

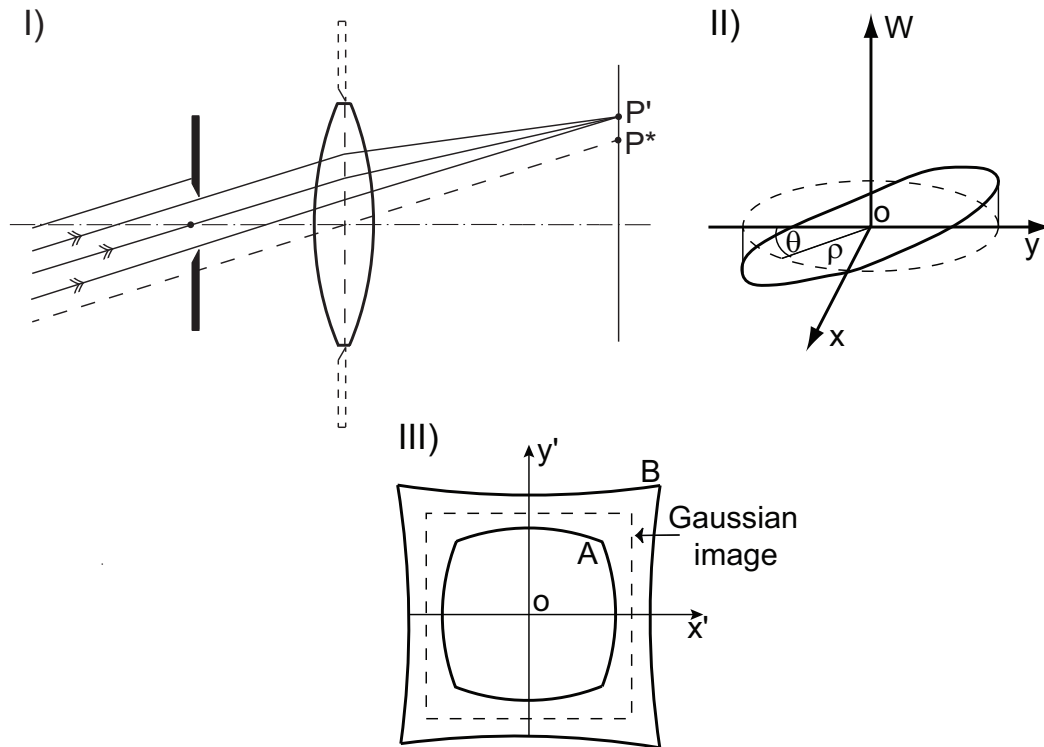


Figure 2.9: Illustration of the effect of image distortion. I) Sketch of distortion rays aberration. The chief ray (dashed line) represents the case, when the lens is located in the same plane as an aperture stop (dashed line). Such arrangement resulted in the chief ray crosses the lens in its center and hits a Gaussian image point P^* , II) Distortion wave aberration, III) An image of the rectangular grid: (Gaussian image) unaberrated image (A) barrel distortion (B) pincushion distortion.

shows the case when the lens lies in the same location as an aperture stop. In such arrangement the chief ray runs through the centre of the lens and hence the amount of distortion is equal to zero.

2.3.3 Primary Field Curvature

Field curvature as it appears in Eq. 2.16 is given by:

$$W = B(y')^2\rho^2. \quad (2.17)$$

It varies as a quadratic function of field position $(y')^2$. For an optical system with nothing but field curvature aberration, all the rays going from different object's points,

form the image on a curved surface, different from the Gaussian image plane. In the Seidel theorem, the image field can be described as a sphere with a radius R_{fc} . This curved surface is called the Petzval surface [66]. The curvature of the Petzval sphere can be expressed as:

$$\frac{1}{R_{fc}} = \frac{4R^2B}{n}. \quad (2.18)$$

Figure 2.10 presents a sketch of the system suffering from field curvature and corresponding shape of the aberrated wavefront. The systems with improved field flatness are basically begin with term "*plan*" e.g. plan-achromat. Obviously the human eye does not belong to "*plan*" systems, but the best image surface is quite close to the retinal surface.

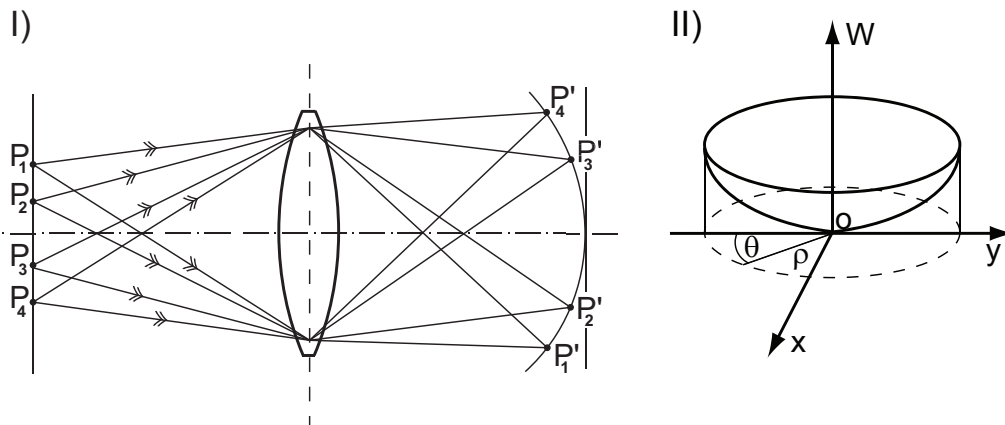


Figure 2.10: Field curvature aberration. I) Rays patch in the presence of field curvature. Object plane points $P_1 - P_4$ are imaged by the optical system on the curved surface in the image plane (points $P'_1 - P'_4$), II) Field curvature wavefront shape.

2.3.4 Primary Astigmatism

Primary astigmatism grows quadratically with the field size y' , and the wavefront shape is given by:

$$W = C(y')^2 \rho^2 \cos^2 \theta. \quad (2.19)$$

Usually astigmatism and field curvature are grouped together; however here we describe this term separately. Astigmatism occurs in optical systems when there is difference in optical power between the plane passing through an object point P and optical axis (meridional or tangential plane) and the plane which is perpendicular to it (sagittal plane). Tangential plane and sagittal plane are constituted by tangential

TR and sagittal *SR* rays consecutively.

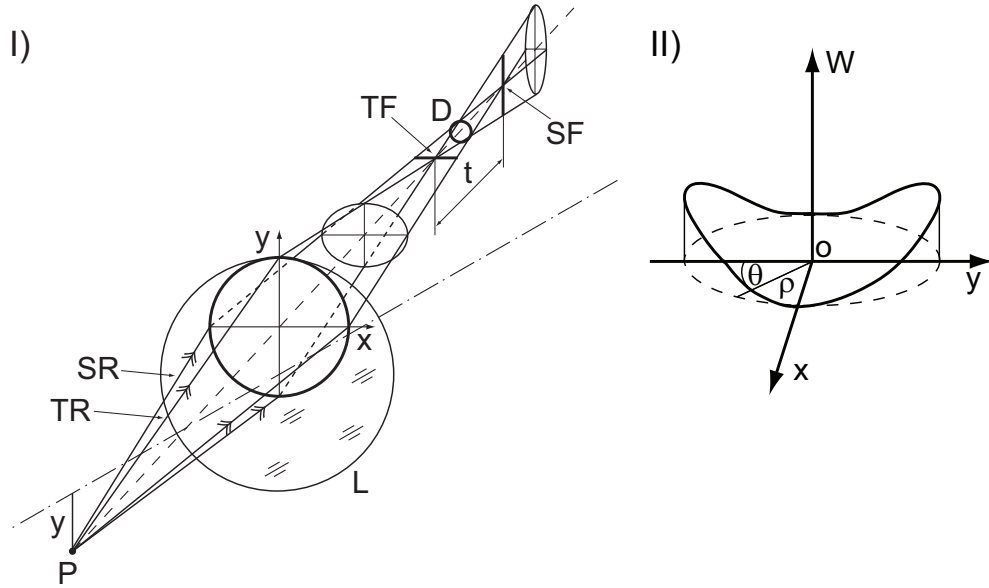


Figure 2.11: Astigmatism aberration. I) Off-axis astigmatism as the ray aberration. The beam of light, characterized by the tangential TR and sagittal SR rays, is propagating through the lens L from an initial point P . After it appears elliptically, the beam is transformed into a line TF called tangential focus and next into a line SF , called sagittal focus. Between the two focal lines TF and TS , the beam is re-formed into a circular shape D called the disc of least confusion. II) Astigmatism aberration wavefront.

Figure 2.11 depicts astigmatism caused by oblique light propagation through the lens L . The circular beam of light is transformed into elliptical shape and then into a line called tangential focus TF . Next, the beam is re-shaping into a, so-called, disc of least confusion D and then again, it is focused into a line perpendicular to TF and called sagittal focus SF . After the sagittal focus line the beam shape is elliptical again. The two lines are called astigmatic focal lines and in fact are at the centres of curvature of the wavefront for the x' - and y' - meridians [63]. It is important to note that the sagittal focal line lies in tangential plane and tangential focal line lies in sagittal plane. The distance t between two focal lines is often taken as a value of astigmatism and following [63] we can write:

$$t = \frac{2R^2C(y')^2}{n}. \quad (2.20)$$

From Eq. 2.20 it is clearly seen that if $y' \rightarrow 0$ then both focal lines coincide in one point, so that the system is free from astigmatism, which is in line with the principle (no astigmatism on-axis). Usually the disc of least confusion (circular shape, D in

Fig. 2.11) lies halfway between radial and tangential focal lines and we are able to calculate its diameter as:

$$d = \frac{2RC(y')^2h}{n}, \quad (2.21)$$

where h is the pupil radius.

2.3.5 Primary coma

The coma aberration occurs due to variation of the focal length within different zones in the pupil.

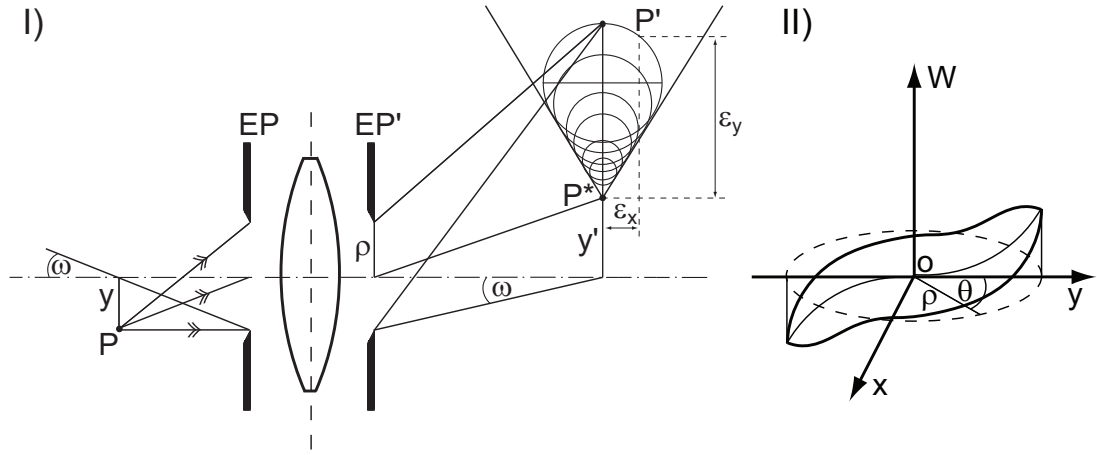


Figure 2.12: Coma aberration. I) Sketch of the coma aberration of object point P located off-axis with a distance y . Single ring of coma contains all rays that intersect the exit pupil EP' with the same distance ρ from the optical axis. Note: ϵ_y and ϵ_x are denoted as coma transverse ray aberrations, whereas P^* and P' are the Gaussian image point and aberrated image point respectively. II) Coma aberration wavefront.

The coma aberration depends linearly on field angle ω , an expression which characterizes it can be given as:

$$W = Dy'\rho^3 \cos \theta. \quad (2.22)$$

Following [63] we can find the transverse ray aberrations:

$$\epsilon_y = \frac{-R}{n} Dy'\rho^2 (2 + 2 \cos 2\theta) \quad (2.23)$$

and

$$\epsilon_x = \frac{-R}{n} Dy'\rho^2 \sin 2\theta \quad (2.24)$$

It is clear to see that if $y = 0$ then $\epsilon_y = \epsilon_x = 0$ and hence the coma aberration is absent on-axis. Based on Eq. 2.24 we are able to draw a sketch for an aberrated image of the object point. Figure 2.12 presents typical "comet" shape of the point spread function in the presence of only pure coma aberration in the system.

When the object point P is located on the axis y , then the coma is a collection of different sized rings located along an axis y' of the Gaussian image plane. A single "coma" circle is composed by a bunch of rays outgoing from the object point P , and crossing an exit pupil EP' with the same distance ρ from an optical axis. The focal length for these rays is the same, but different from other annular zones. Collection of all rings for given y distance, but different ρ values, contained in a cone with an angle of 60 degree is called coma aberration.

2.3.6 Primary Spherical Aberration

Spherical aberration (SA) usually occurs in optical systems after refraction or reflection from the spherical surface, which explains the name of the aberration. The reason is that the back focal distance is different for different ray heights. For a simple positive single lens, the back focal distance of the marginal rays is shorter than the back focal distance of the paraxial ray. This type of optical imperfection represents pupil-dependant aberration as it is not depend on field position y' of the object point (it is the only Seidel aberration which is a field independent term). The wavefront shape for the primary spherical aberration is given by:

$$W = E\rho^4 \quad (2.25)$$

Figure 2.13 shows bundle of rays going from the object point P to the image point P' in the meridional cross-section ($\theta = 0$). The Gaussian image point P^* may be found then by two paraxial rays denoted as $1a$ and $2a$ at the paraxial (Gaussian) focal plane. The longitudinal spherical aberration Δ_z indicates how much the image point is spread along the optical axis, whereas the linear size of the point spread in the paraxial focal plane (perpendicular to the optical axis) is indicated by Δ_y and it is called the transverse spherical aberration. For a simple case (third-order SA) Δ_z is proportional to the pupil coordinate of the incident ray (radial distance ρ from the optical axis). Figure 2.13 presents the longitudinal SA as a function of the pupil radius ρ . Traditionally, primary spherical aberration is characterized for axial image point; however it appears everywhere in the field, and has the same magnitude (by definition).

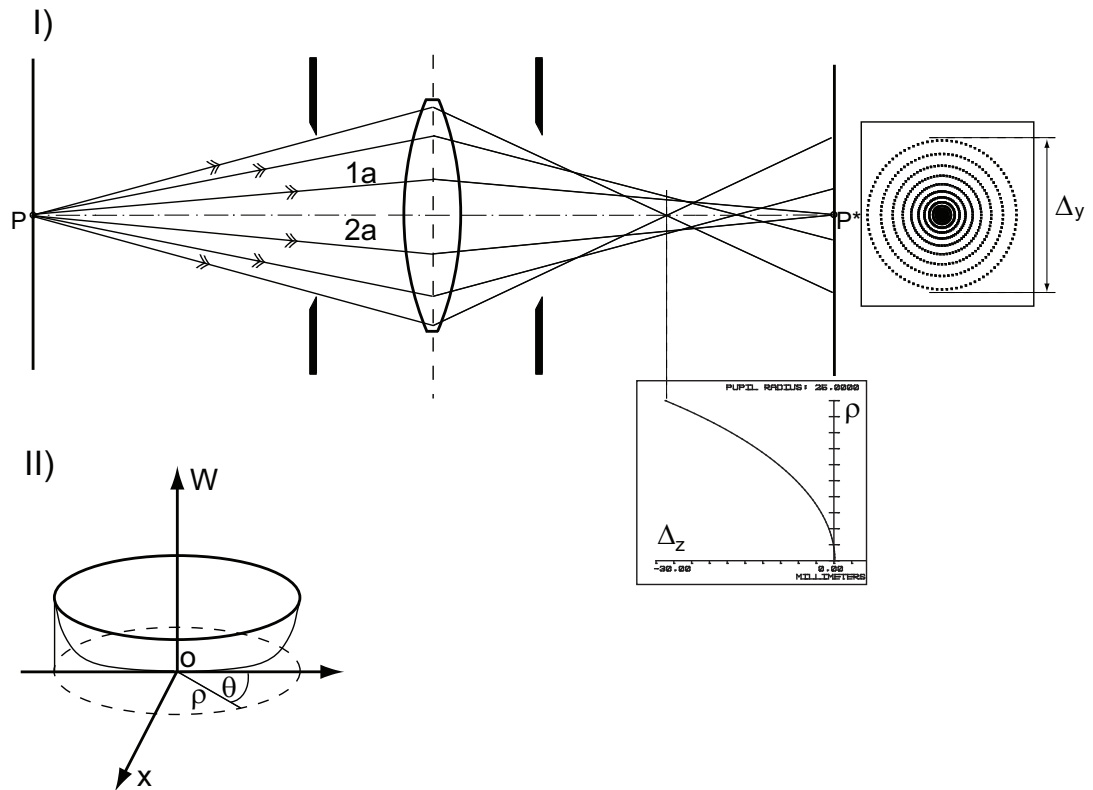


Figure 2.13: Spherical aberration. I) Sketch of the ray paths in the presence of spherical aberration in a meridional plane result in transversal and longitudinal spherical aberration. Two paraxial rays denoted as $1a$ and $2a$ are converging in the Gaussian image point P^* . The longitudinal spherical aberration Δ_z indicates how much the image point is spread along the optical axis, whereas the transverse spherical aberration Δ_y gives the linear size of point spread in the perpendicular plane. II) Spherical aberration wavefront shape.

For example a single lens with two spherical surfaces (r_1, r_2) made of glass with a refractive index n and placed in air is always affected by the spherical aberrations. However, the amount of spherical aberration will reach the minimum if ratio between two radii of curvature from two spherical surfaces undergo an expression written below:

$$\frac{r_2}{r_1} = \frac{n(2n+1)}{2n^2 - n - 4} \quad (2.26)$$

A classical example of compound lens with corrected spherical aberration is a doublet. All groups of aplanatic lenses are free from coma and spherical aberration, the eye is not the case. A paraboloidal mirror is also free from spherical aberration.

2.3.7 Secondary Aberrations and Seidel Series

The Seidel aberrations, or primary aberrations, are just a first step in describing aberrations of the system with rotational symmetry. Based on the same assumptions as in the case of Seidel ($x = 0$) we can derive higher-order aberration function [67]:

$$\begin{aligned}
 W(\rho^2, \rho y' \cos \theta, (y')^2) = & Fy^5 \rho \cos \theta \\
 & + Gy^4 \rho^2 \\
 & + Hy^4 \rho^2 \cos^2 \theta \\
 & + Iy^3 \rho^3 \cos \theta \\
 & + Jy^2 \rho^4 \\
 & + Ky^3 \rho^3 \cos^3 \theta \\
 & + Ly^2 \rho^4 \cos^2 \theta \\
 & + My \rho^5 \cos \theta \\
 & + N\rho^6.
 \end{aligned} \tag{2.27}$$

Similarly to Eq. 2.16, from Eq. 2.27 we can derive a few new terms describing higher-order aberrations. All coefficients in Eq. 2.27 (from F to N) are called Schwarzschild coefficients and represent secondary (or Schwarzschild) aberration theory. However, the five first terms ($F - J$) have the same shapes as the Seidel primary aberrations, but then there are four other terms ($K-N$) representing new families of wavefront shapes. We shall not go into details with Schwarzschild aberration function, although short description of new terms will be given. The sixth term with the K coefficient represents the arrow aberration with a form of $\rho^3 \cos^3 \theta$, which takes its name from a shape of the aberrated point spread function (*PSF*). The other three terms with L , M and N coefficients, called the secondary astigmatism, the secondary coma and the secondary spherical aberration respectively, exist as higher-order aberrations of their counterparts in the Seidel aberrations. Therefore these of higher-order aberrations have similar effects on imaging and their origin is related to their Seidel counterparts. The importance of the classical aberrations of Seidel and Schwarzschild is that they can be extended to a set of infinite series that is reduced to a pupil component for a given field position y' . This set of basis functions, called Seidel series, can be introduced as:

$$S_i(\rho, \theta) = S_n^m(\rho, \theta) = \rho^n \cos^m \theta \tag{2.28}$$

Table 2.1: Primary and secondary aberrations [67].

i	n	m	Seidel Series	Classical Aberration	Aberration Name
0	0	0	1		
1	1	1	$\rho \cos \theta$	Seidel	distortion
2	2	0	ρ^2	Seidel	field curvature
3	2	2	$\rho^2 \cos^2 \theta$	Seidel	astigmatism
4	3	1	$\rho^3 \cos \theta$	Seidel	coma
5	3	3	$\rho^3 \cos^3 \theta$	Schwarzschild	arrow
6	4	0	ρ^4	Seidel	spherical aberration
7	4	2	$\rho^4 \cos^2 \theta$	Schwarzschild	secondary astigmatism
8	4	4	$\rho^4 \cos^4 \theta$		
9	5	1	$\rho^5 \cos \theta$	Schwarzschild	secondary coma
10	5	3	$\rho^5 \cos^3 \theta$		
11	5	5	$\rho^5 \cos^5 \theta$		
12	6	0	ρ^6	Schwarzschild	secondary sphr. aberration
13	6	2	$\rho^6 \cos^2 \theta$		
14	6	4	$\rho^6 \cos^4 \theta$		
15	6	6	$\rho^6 \cos^6 \theta$		

where i orders the series, n stands for radial degree and m represents the azimuthal frequency. Table 2.1 presents the Seidel series up to the sixth order.

2.3.8 Zernike Power Series and the RMS Wavefront Error

The ocular aberrations may be decomposed into a number of basic shapes of sphere, cylinder, spherical aberration and coma-like as:

$$W(\rho, \theta) = \sum_{i=0}^{\infty} a_i F_i(\rho, \theta), \quad (2.29)$$

where a_i is the expansion coefficient of the i -th basis function F_i . Thus, a mathematical representation is convenient especially in the ocular aberrations case as those components are commonly occurring in the eye. In this work we shall use Zernike polynomials set (complete derivation in [65]), which nowadays is a standard for reconstruction of an aberrated wavefront in the eye [68]. These polynomials, introduced by the Dutch scientist Fritz Zernike in 1934 (also Nobel prize laureate for the invention of phase-contrast microscope in 1953), can be applied to describe mathematically wavefront

deviation from a reference sphere. Each polynomial describes specific deformation of the surface; their combined sum can produce a large number of more complex surface shapes.

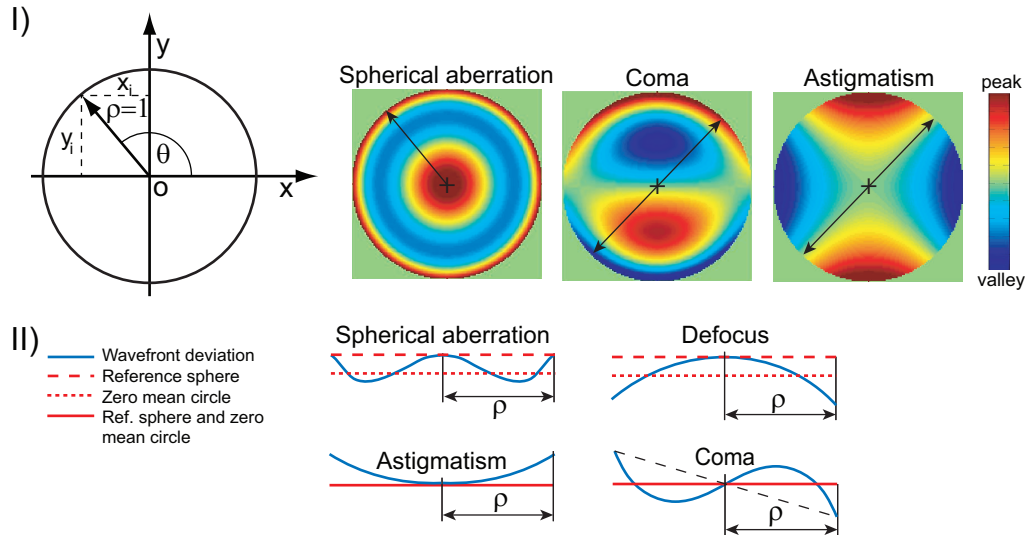


Figure 2.14: Deviation of the wavefront by using of Zernike polynomials. I) A radial point height ρ in the unit-radius circle and its angular circle coordinate θ , in the pupil plane of an eye, in which the wavefront is evaluated II) Reference sphere and zero mean circle for selected Zernike terms. On the right, wavefront deviations of a three chosen Zernike modes, shown as topography or phase maps.

There are several features of the Zernike polynomial that make them particularly useful. First of all Zernike polynomials define deviations from zero mean as a function of the radial point height ρ in the unit circle and its angular circle coordinate θ , which are located in the pupil, in which the wavefront form is evaluated (See case (I) in Fig. 2.14). The ρ and θ values, of each polynomial, change independently one from another, and hence polynomials are orthogonal over the circle of unit radius. Due to this property, these aberration forms are called orthogonal, or Zernike aberrations. In addition, they exhibit few very useful properties such as: the truncation or lengthening of an expansion of the ocular aberration of any eye does not change the remaining coefficients.

Secondly, in order to give a minimum variance across the pupil, the Zernike terms represent balanced aberrations. It means, that given aberration term is mixed with one or more lower-order aberrations in order to reduce its variance (note, that the Strehl ratio is higher for a smaller aberration variance). For a wavefront, zero mean is defined as a surface for which the sum of wavefront deviations to either side is

zero (that is important conceptual difference vs. standard wavefront error, which expresses deviations from reference sphere). Hence the polynomial, which is a product of its radial variable in ρ and angular variable in θ , has zero value at the intersection of the wavefront and its zero mean (See case (II) in Fig. 2.14). Zero mean differs from reference sphere for balanced primary spherical aberration and defocus, while coinciding with the reference sphere for balanced primary astigmatism and coma.

Another useful property is, because each polynomial represents its standard deviation in the Zernike expansion, the sum of the squares of the coefficients gives the variance of the wavefront deviation. Finally the Zernike terms are related to the classical Seidel aberrations (which are not balanced) used to describe optical aberrations. For a given surface $W(\rho, \theta)$ a complete mathematical description is provided by following [69], where A_{nm} and B_{nm} are the Zernike coefficients:

$$W(\rho, \theta) = A_{00} + \sum_{n=2}^{\infty} A_{n0} R_n^0(\rho) + \sum_{n=1}^{\infty} \sum_{m=1}^n R_n^m [A_{nm} \cos(m\theta) + B_{nm} \sin(m\theta)]. \quad (2.30)$$

The radial dependence of the Zernike polynomials is given by the following expression:

$$R_n^m(\rho) = \sum_{s=0}^{(n-m)/2} \frac{(-1)^s (n-s)!}{s! \left(\frac{n+m}{2} - s\right)! \left(\frac{n+m}{2} - s\right)!} \rho^{n-2s}. \quad (2.31)$$

The variables n and m are integer values and are known as the radial and azimuthal wave number, respectively. Using these radial polynomial, the coordinates have to be normalized so that the radius of the pupil is unity. Born and Wolf [65] define the Zernike polynomials as:

$$Z_n^m(\rho, \theta) = R_n^m(\rho) \cos(m\theta), \quad (2.32)$$

and

$$Z_n^{-m}(\rho, \theta) = R_n^m(\rho) \sin(m\theta), \quad (2.33)$$

using two indexes for every polynomial, referred to as the radial order n and angular order m . Throughout this thesis, we shall use the double index of Born and Wolf's notation $c(m, n)$ for the Zernike aberration coefficients and $Z(m, n)$ for the Zernike aberration polynomials.

The first 20 Zernike polynomials are shown in Figure 2.15. The zero radial and first radial order have no relevance for the aberrations in the eye. It is related to the fact, mentioned already, that the optical axis is not easy to define in the eye because the cornea and lens are not aligned and therefore, the line of sight is usually taken as the

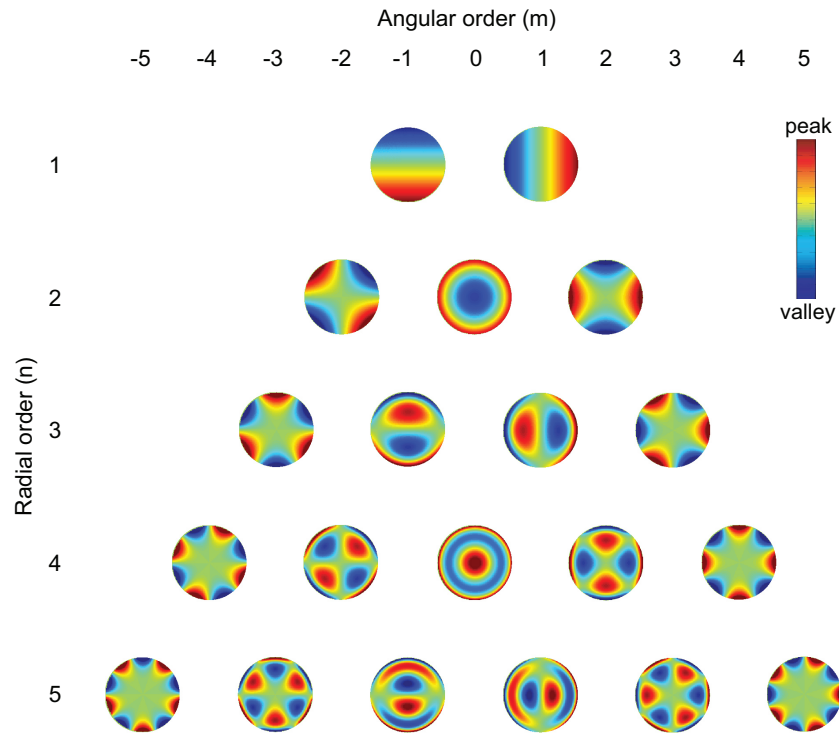


Figure 2.15: Representation of the first 20 Zernike polynomials as they appear in the pupil. Born and Wolf notation.

reference axis of the eye. Due to lack of rotational symmetry and the fact that the eye is very difficult to align, the y -tilt $Z(-1,1)$ and x -tilt $Z(1,1)$ terms, are usually removed from reconstructed wavefronts. Second-order terms correspond to the refractive errors (sphere and cylinder); these terms will be referred to as "lower-order" aberrations. It is important to point out that there are higher-order polynomials, which also contain lower-order term (defocus and astigmatism). This is due to balanced nature of Zernike polynomials. The 3rd, 4th and 5th row maps represent "higher-order" aberrations and some terms are similar to the Seidel aberrations coma and spherical aberration. However, because of lack of rotational symmetry in the eye, there are many other terms (with $\sin\theta$, $\sin 3\theta$, $\cos 3\theta$, and so on) that have no Seidel counterparts. Practically, in the expansion of the wavefront, every polynomial has a coefficient $c(m,n)$, which represents the weight of that polynomial in the wavefront. Thus Zernike coefficients and Zernike polynomials can describe any continuous wave aberration function over a circular pupil as:

$$W(\rho, \theta) = \sum_{m,n} c_n^m Z_n^m(\rho, \theta). \quad (2.34)$$

And again, keeping in mind that each coefficient c_n^m brings standard deviation value

of its corresponding aberration term and based on [23] we can write simple expression:

$$\Delta\phi = \sqrt{\sum_{m,n} (c_n^m)^2}, \quad (2.35)$$

where $\Delta\phi$ is known as the *RMS* wavefront error. The quantity of the *RMS* error indicates how much a wavefront fluctuates and thanks to the orthogonality of the polynomials it can be calculated as a whole, or as groups, for example only for the higher or lower-order terms. Table 2.2 presents first 20 Zernike polynomial terms up to 5th order .

Table 2.2: Zernike polynomial terms up to and including the 5th radial order [67].

i	n	m	Zernike Polynomial	Aberration name
0	0	0	1	Piston
1	1	-1	$2\rho \sin\theta$	Vertical tilt
2	1	1	$2\rho \cos\theta$	Horizontal tilt
3	2	-2	$\sqrt{6}\rho^2 \sin 2\theta$	Diagonal astigmatism ($\pm 45^\circ$)
4	2	0	$\sqrt{3}(2\rho^2 - 1)$	Defocus
5	2	2	$\sqrt{6}\rho^2 \cos 2\theta$	Horizontal astigmatism (0° or 90°)
6	3	-3	$\sqrt{8}\rho^3 \sin 3\theta$	Vertical trefoil coma
7	3	-1	$\sqrt{8}(3\rho^3 - 2\rho) \sin\theta$	Vertical coma
8	3	1	$\sqrt{8}(3\rho^3 - 2\rho) \cos\theta$	Horizontal coma
9	3	3	$\sqrt{8}\rho^3 \cos 3\theta$	Horizontal trefoil coma
10	4	-4	$\sqrt{10}\rho^4 \sin 4\theta$	Vertical quadrafoil
11	4	-2	$\sqrt{10}(4\rho^4 - 3\rho^2) \sin 2\theta$	Secondary diagonal astigmatism
12	4	0	$\sqrt{5}(6\rho^4 - 6\rho^2 + 1)$	Spherical Aberration
13	4	2	$\sqrt{10}(4\rho^4 - 3\rho^2) \cos 2\theta$	Secondary horizontal astigmatism
14	4	4	$\sqrt{10}\rho^4 \cos 4\theta$	Horizontal quadrafoil
15	5	-5	$2\sqrt{3}\rho^5 \sin 5\theta$	Vertical quantifoil
16	5	-3	$2\sqrt{3}(5\rho^5 - 4\rho^3) \sin 3\theta$	Secondary diagonal trefoil coma
17	5	-1	$2\sqrt{3}(10\rho^5 - 12\rho^3 + 3\rho) \sin 3\theta$	Secondary vertical coma
18	5	1	$2\sqrt{3}(10\rho^5 - 12\rho^3 + 3\rho) \cos 3\theta$	Secondary horizontal coma
19	5	3	$2\sqrt{3}(5\rho^5 - 4\rho^3) \cos 3\theta$	Secondary horizontal trefoil coma
20	5	5	$2\sqrt{3}\rho^5 \cos 5\theta$	Horizontal quantifoil

2.4 Measures of the Quality of Optical Systems

As we know aberrations can affect the quality of the image and in the real world there is no such thing as an aberration-free optical system. There are several optical metrics to measure the quality of optical performance of the system. Before we start reviewing on the quality evaluation methods it would be appropriate to say a few words about so-called diffraction limited image quality.

Diffraction

Due to diffraction on finite aperture, light from an object point is never converging to the corresponding image point. The actual image of a point source formed by a perfect optical system is blurred. The only one factor here limiting the quality of the image is diffraction and hence provides the reference for the best image quality achievable. Diffraction comes from the wave nature of light and occurs at the boundary of obstacles (aperture) in the light path that alter the amplitude and phase of an incident wavefront. The diffraction influences an image of a point source in such way that instead of perfect point, there is a bright central disc surrounded by a number of concentric rings. The result of diffraction depends, among others factors, on the shape and the size of the entrance pupil, however here we are dealing only with circular pupils (or elliptical for small off-axis angles). For an aberration-free system the central disc is known as the Airy disc, which contains about 84 percent of the energy [69]. The diameter $2R$ of the Airy disc represents the smallest blur diameter that an optical system can produce and is given by:

$$2R = 2.44\lambda \frac{f}{D}, \quad (2.36)$$

where f is the focal length, D is the pupil diameter and f/D is a measure of the light collecting properties of an optical system (f-number). The smallest blur that the optical system produces is one of the most important property of its quality performance. This ability of an optical system to distinguish details in the image it produces is called angular resolution. Figure 2.16 presents a sketch of the angular diameter ψ for two of object points A and B . It is assumed, that the eye can distinguish both points separately if the light intensity along the line, connecting the two central points of Airy discs, has a minimum where the light intensity does not exceed 0.735 of the maximum value. The above condition is true when the central peak of one image falls upon the first minimum of the other image. Using equation 2.36 we can derive an expression

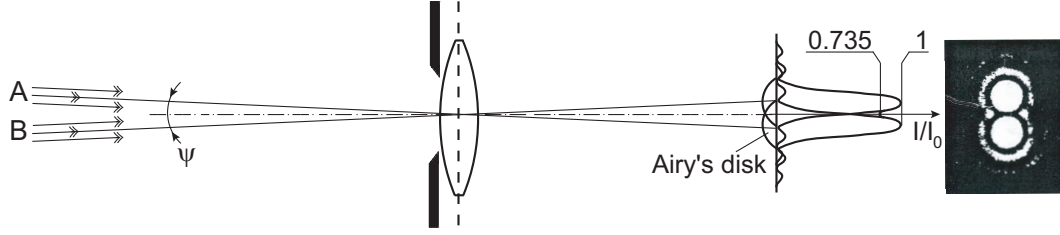


Figure 2.16: Angular diameter ψ of the two object points A and B is equal to the angular resolution of the eye. Following Rayleigh criterion, images of two points (A, B for instance) can be detected separately if the central point of an Airy's disk of one point falls upon an edge of the Airy's disk of the latter.

for angular resolution $\Delta\theta$ known as the Rayleigh criterion in radians as:

$$\Delta\theta = 1.22 \frac{\lambda}{D}, \quad (2.37)$$

For example, for an aberration-free eye of a 3mm diameter pupil size and a wavelength of $550\ \mu\text{m}$, a point-like object placed at infinity is imaged on the retina as an Airy disc of $4\ \mu\text{m}$ radius or $46\ \text{arc seconds}$ radius [16].

Point Spread Function

The intensity distribution, treated as the response of the system to a point source at infinity, is commonly called the intensity point spread function (PSF) and its shape indicates the image quality [70]. Aberrations of any optical system change the shape and size of PSF , which degrades the image quality. The effects of aberrations can therefore be characterized by calculating the PSF of the optical system. We can define it following [70], as:

$$PSF(x, y) = \frac{1}{\lambda^2 d^2 A_p} \left| \left| FT \left\{ p(x, y) \cdot e^{-i \frac{2\pi}{\lambda} W(x, y)} \right\} \right|_{f_x = \frac{x}{\lambda d}, f_y = \frac{y}{\lambda d}} \right|^2, \quad (2.38)$$

where FT is the Fourier transform operator, d is the distance from the exit pupil to the image, A_p is the area of the exit pupil, $p(x, y)$ defines shape, size, and transmission of the exit pupil, $\exp(-i(2\pi/\lambda)W(x, y))$ accounts for the phase deviations of the wavefront from a reference sphere, and finally $W(x, y)$ is the wavefront aberration function at the exit pupil.

Following the Rayleigh resolution criterion, it is easy to capture, that the width of

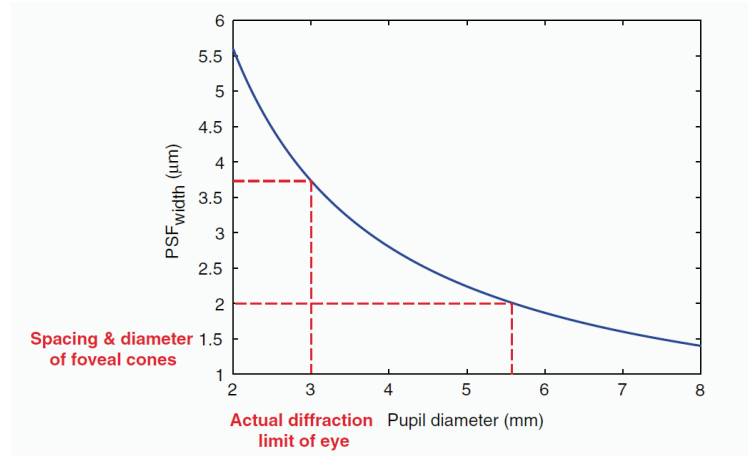


Figure 2.17: Variation in the width of the PSF as a function of pupil diameter, for a diffraction-limited eye and wavelength of 550 nm [71]. The width of the PSF decreases with an increasing of a pupil diameter and hence increases the resolution.

the diffraction-limited intensity PSF is effectively equal to the distance between the central peak of one image and the first minimum of the other image, described above. Here we can write:

$$PSF_{width} = 1.22 \frac{\lambda f}{nD}, \quad (2.39)$$

where λ is the wavelength, f is the focal length, n is refractive index and D is the pupil diameter. It is easy to see, that for a fixed wavelength increasing the pupil diameter, the PSF is getting narrower and the resolution is getting higher. This is illustrated in Figure 2.17 [71]. For a wavelength of 550 nm , in order to resolving the cone photoreceptors (separated by around $2\text{ }\mu\text{m}$ at the fovea [72]) the pupil diameter needs to be greater than around 5.5 mm . Nevertheless, the study of Liang and Williams has shown, that the eye reaches the diffraction limit for a pupil diameter of around 3 mm , but beyond this image quality is degraded by aberrations [9].

Strehl Ratio

We have already stated that the PSF of a diffraction-limited optical system (Airy pattern) can represent the irradiance of an optical system. However, the appearance even of a small amount of aberrations redistributes the energy lowering the central intensity of the PSF and thus degrades the image quality. Here we can implement another metric called a Strehl ratio [65–67], which is defined as the ratio between the normalized peak intensity of the actual PSF to that of the perfect PSF (aberration-free). An

approximate value of the Strehl ratio can be expressed as:

$$S = \exp\left(-\left(\frac{\Delta\phi}{\lambda}2\pi\right)^2\right), \quad (2.40)$$

where $\Delta\phi$ (the *RMS* wavefront error) and λ are expressed in *microns* [73, 74]. For the image quality assessment there is the Strehl or Maréchal criterion saying, that the Strehl ratio has to be greater than 0.8, which is then equivalent to the condition that the *RMS* wavefront error is less than $\lambda/14$. An optical system that fulfils this condition is referred to as effectively diffraction limited. For small aberrations the *RMS* wavefront error can be directly related to image quality using the Strehl ratio (see Eq. 2.40). However, for human eyes, the Strehl ratio is usually so low that a satisfactory correlation with visual performance is rather difficult to achieve.

Modulation Transfer Function

Another common measure of image quality is the modulation transfer function *MTF*, which describes how well an optical system transfers spatial frequencies (note: a point object contains an infinite number of spatial frequencies).

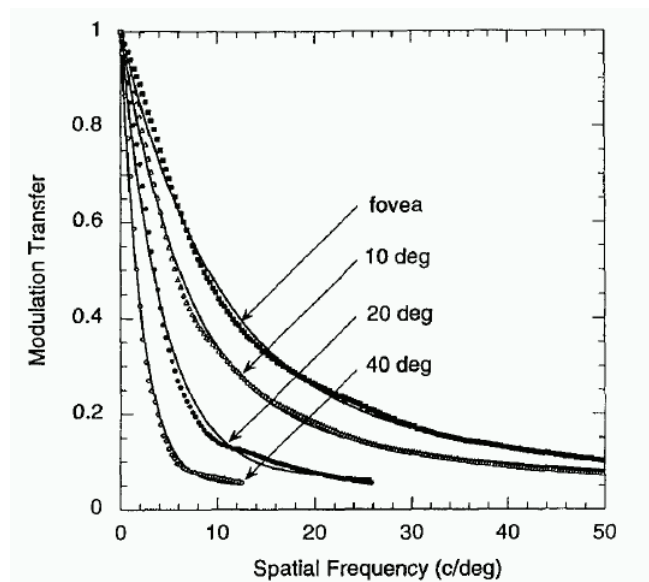


Figure 2.18: Example of modulation transfer function (*MTF*) of the human eye as a function of retinal eccentricity. *MTFs* at different field angles for a 3 *mm* pupil. The position of focus is that corresponding to the circle of least confusion, with no correction for oblique astigmatism. Figure taken from [75].

In the case of a human eye, increasing amount of ocular aberrations lowers the *MTF*, especially for large pupil diameters [9,76]. It was also reported, that the *MTF* significantly drop its value as retinal eccentricity increases [75]. Figure 2.18 shows an example of *MTF* as a function of retinal eccentricity for a 3 mm pupil [75]. Mathematically, the Fourier transform of the *PSF* is the optical transfer function *OTF*, the amplitude of which is the *MTF*.

$$MTF = |OTF| = |FT\{PSF\}|. \quad (2.41)$$

The number of different metrics for analysis of image quality is large, but the *PSF*, Strehl ratio and the *MTF* are commonly used to predict the outcome of an optical correction.

2.4.1 Ocular Aberrations in the Human Eye

Here we treat the eye as a finite optical system and, as we have already mentioned, the ideal case of any optical system does not exist in real world. When the image of a distant object is focused on the retinal fovea (with relaxed accommodation state), the eye is emmetropic. However, more frequently the eye is likely to produce an image either before the retina (myopic case, very common in young population) or after the retina (hyperopic case) and thus, the defocus error is developed within the eye. The axial length of the eyeball may play a significant role as it is postulated, that myopic eyes are longer compared to hyperopic eyes [77]. A second factor, that may move the image away from the retina, comes from difference in refractive power of the eye, which is too low or too high for hyperopic and myopic eyes respectively. Another type of refractive error (also denoted as lower-order aberration term in Zernike expansion), is astigmatism, which results in two foci lines due to different refractive power in two, mutually perpendicular, meridians. The astigmatism refraction error, so-called, "*with the rule*" astigmatism, arises when the vertical meridian of the corneal surface is steeper (i.e. with more optical power). It has been determined that this type of astigmatism is likely to appear in young population eyes [78]. In the latter case, when the horizontal meridian is more powerful, it is called "*against the rule*" astigmatism [23,77]. These two types of basic but very common optical defects (sphere and cylinder), are represented by the lower-order Zernike terms, i.e. $Z(2,0)$, $Z(2,-2)$ and $Z(2,2)$. Fortunately these errors can be easily corrected by including an appropriately selected lens with sufficient amount of spherical and/or cylindrical components.

Because the optical setup of the eye consists of different components, we can distinguish a few sources of ocular aberrations. One of the recent findings in physiological optics is that, some optical elements of the eye are balanced to produce an optimal improved image on the retina. A very robust example of this mutual adjustment is the balance between the contributions of the cornea and the internal optics of the eye. As we have already mentioned, the cornea, due to its toricity, is the main source for astigmatism which for the population average, reaches the value of slightly below of $0.5 D$ [79]. However this is the value of residual astigmatism, since the corneal astigmatism is partially compensated by internal optics of the eye. The work of Kelly *et al.* showed strong evidence of corneal astigmatism 0 or 90 degree ($Z(2,2)$ Zernike term) to be compensated by internal optics of the eye up to 41 percent [80], which is in line with previous findings by Artal and colleagues [81]. Here we shall keep in mind that the corneal astigmatism is not classical astigmatism, since the origin of classical astigmatism comes from the field dependency of this aberration term in rotationally symmetric optical systems. In 2009 Espinosa and Kasprzak came up with the hypothesis that the corneal astigmatism may play role in compensating the field-dependent astigmatism. Using a theoretical Kooijman eye model [59] for simulating of the oblique light incidence, they found the total astigmatism to be minimal for two points at both sides of the optical axis at ± 4.8 degree [78]. It is worth noticing, that previous findings stated only for one minimum at the nasal side visual field [82,83].

Spherical aberration arises from a sphericity of surfaces of the optical components of the eye. Just because of optical design of the eye, it can be easily seen that the cornea and the lens contribute the most to the total amount of spherical aberration. Important work of El Hage and Berny, done in 1973, has shown that, the crystalline lens serves as a compensatory element for corneal spherical aberration [84]. This is in good agreement with later work of Artal *et al.*(2001), where for young and healthy eyes, corneal aberrations were neutralized by immersing the eye in saline [81]. Another work by Kelly and colleagues (2004) confirmed again balancing role of the young crystalline lens on corneal spherical aberration (over 40 percent reduction), giving an average value of $0.114 \mu m$ Zernike spherical aberration coefficient (for 6 mm pupil diameter) for 30 young subjects [80]. Although the balancing mechanism works properly for most of young eyes, this may be interrupted by change in the lens shape and gradient index distribution as the crystalline lens changes with both age and accommodation. Effect of aging on the spherical aberration and other terms from higher-order group has been also well studied. The conclusion that combines the work of various authors is that spherical aberration increased significantly with age with shift towards more positive values, and there is non-negligible increase of other higher-

order aberration terms [85–87]. The influence of accommodation on higher-order aberrations in the eye has also been investigated. The results showed tendency of spherical aberration to change its sign from positive to negative during accommodation, whereas some other aberration terms like astigmatism and coma, demonstrated variable direction of change with accommodation [88,89].

Some ocular aberrations appear in the eye because of decentration or/and tilt of some optical elements like pupil, surfaces of the cornea and crystalline lens. This misalignment of the optical components results, for example, in presence of coma aberration. This term, consists of two components $Z(3,-1)$ and $Z(3,1)$ in Zernike polynomial notation, classically appearing when the rays of light come from off-axis positions entering the eye. Because of mutual decentration of the pupil and the crystalline lens, the optics of the eye cumulate an additional amount of coma, which dominates on-axis in order to compensate for off-axis coma contribution. Artal and colleagues presented a good compensation effect on corneal coma by the internal coma component. They stated, that the pupil decentration may play a significant role in coma balancing [81]. The work of Kelly *et al.*, shows the same tendency but only for a vertical coma component ($Z(3,-1)$) [80]. Such an existence of apparent fine tuning mechanism for some aberration terms, proposed by Kelly [80], has led number of authors to perform measurements of misalignments quantity of the eye's optical components. In 2006 Rosales and Marcos, using the Purkinje imaging optical setup, presented some results for the crystalline lens tilt and decentration based on 17 normal eyes from young population [90]. They found the lens to be tilted from -1.13 to $+2.8$ *degree* horizontally, and from about -1 to 2.58 *degree* vertically with mirror-symmetric tendency of the lens tilt in left and right eye of the same subject. Beyond that, some data on the lens decentrations has been introduced as well, showing the average horizontal decentration ranged from 0.09 to 0.45 *mm* and vertical decentration being between 0.09 and -0.22 *mm* [90]. In other recent work, Tabernero *et al.*, based on experimental data from 18 young and healthy subjects, found the lens decentration, with respect to the entrance pupil center, to be around 0.13 *mm* without any significant trend in orientation [91]. Moreover, the authors concluded with an idea of the eye acting like an aplanatic system where, for instance, the angle kappa (κ) compensates horizontal coma which is produced by the horizontal tilt of the crystalline lens.

Many researchers studied the optical effect of a pre-corneal tear film variation. It is well known, that this thin layer of tear liquid smoothes the corneal surface minimizing the light scattering effect, but on the other hand wavefront aberration measurements are affected by its quality. The tear film may vary due to different factors

such as: (a) normal physiology: diurnal fluctuations, menstruation, potentially diet, (b) environment : air-conditioning, air-pollution, contact lens wear and (c) pathological conditions: dry eye, medications. Hence, the optical effect of the tear film on vision is of great interest for eye modeling, corneal topography and eye aberrometry in general. In early work by Smirnov (1961), it was suggested, that the tear film may play a non negligible role for the inter-subject variability in the measurements of ocular wavefront aberrations [92]. Other work of Tutt *et al.*(2000) [93], where objective method for assessment of the retinal image quality was implemented, clearly showed the relation between the tear film break-up and image quality degradation [93]. Precise measurements of the tear film dynamics have recently been achieved. A number of studies, where different tear film metrology techniques were involved, seem to confirm previous findings with a strong evidence of the effect of the changes in tear topography on the optical quality of the eye. In work of Dubra *et al.* [94, 95], and Szczesna and Iskander [96], the lateral shearing interferometer was used to perform measurements of tear topography. On the other hand, non-interferometric methods also successfully passed the "exam" for the efficiency and precision of the tear film variation 'measurements: the Shack-Hartmann technique, implemented by Li and Yoon [97] or the curvature wavefront sensor, used by Gruppetta and colleagues [98].

From brief overview on possible sources of the ocular aberrations, the general picture of the eye as the complete optical system, because of its complexity, is such that it is not a simple optical system. Furthermore, decentrations, misalignments and tilts of the optical components raise a question for reasonable usage of classical Seidel aberration theory (suitable for systems with rotational symmetry) to describe the optical properties of the eye. Some authors came up with hypothesis stating, that in order to provide the best image quality on the fovea, lens tilt, angle κ or corneal astigmatism may combine, creating kind of self-adjustment mechanism of the eye [99]. However, at the opposite pole, some authors reject this idea of the eye's robustness [34]. Also the work of He *at al.* [100] suggested that we should rather be more careful with a statement about precise compensation mechanism within the eye. They measured 90 eyes from 45 young and healthy subjects using a topographic system and a psychophysical ray-tracing wavefront sensor. The conclusion which raised was that the balance between anterior cornea and the internal optics is a subject-dependent process in term of compensation and addition, and moreover, some crystalline lens aberrations may compensate the corneal aberrations but rather coincidentally. Since the human eye does not appear as a simple optical system, more work is required to fully cover all uncertainties of its optical properties.

2.5 Wavefront Measurement Techniques for the Human Eye

For many decades different approaches to wavefront sensing in the eye have been evolving into two classes: pupil plane and image plane based methods. Not to underestimate previous achievements in the study of the eye's optical properties, we can fairly say that Thomas Young was the first pioneer of the pupil plane wavefront sensing in the eye. Although degrading effects of optical aberrations on image quality were known already due to the limitations seen in telescopes or microscopes, Thomas Young introduced the concept of ocular aberration. After Young published his work "*On the mechanism of the eye*" in the beginning of 19th century [101], one hundred years later Alvar Gullstrand made a first step to the image plane wavefront sensing in the eye. However, only in 1961 Smirnov gave an idea about sampling the wavefront slope across the pupil to estimate the *PSF* and the corresponding aberrations of the optical system of the eye [92].

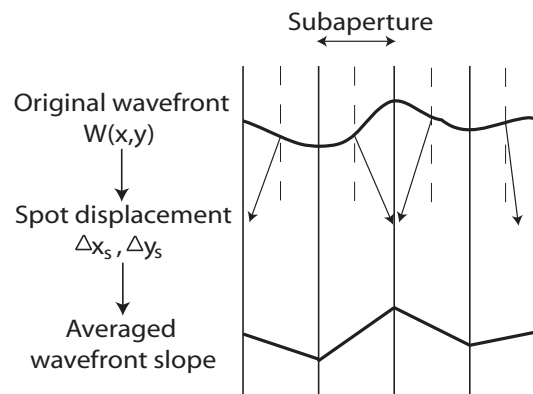


Figure 2.19: Principle of measuring ocular aberrations with a wavefront sensor. A wavefront sensor measures local wavefront slopes and provides sufficient information to reconstruct the complete wavefront shape from the measured slopes.

There is a common opinion that this approach given by Smirnov was the beginning of "*modern*" era in the wavefront sensing in the eye. Wavefront sensors (*WFSs*) can be categorized by whether the measurements are based on a subjective or objective method and whether the wavefront sensor measures the light that goes into the eye or comes out of the eye. In the latter case *WFSs* measure ocular aberrations in object space. However, all wavefront sensors developed for vision science and ophthalmology are based on the same principle mentioned already, which is an indirect measurement

of local wavefront slopes and reconstruction of the complete wavefront surface by integrating these slopes [102], as illustrated in figure 2.19.

2.5.1 Laser Ray-tracing

This technique was developed by Rafael Navarro *et al.* introducing an instrument to evaluate the slope of the wavefront by sampling the pupil with a narrow collimated incoming beam [103,104]. This narrow beam is directed into the eye through a range of positions in the pupil, sequentially (see Fig. 2.20). A mirror, or combination of two mirrors, must be repositioned between a single measurement to move the laser beam within the pupil. For each beam position in the pupil, the retinal beacon is re-imaged back through the whole pupil onto a CCD array. The centroids of the images are compared with that of the reference image that corresponds to the pupil centre in order to give transverse aberration of the beam. As a result, one obtains a "spot diagram" for the optical system of the eye, which can also be used to measure ocular aberrations off-axis. This technique can measure a wide range of refractive errors and aberrations (large dynamic range).

Unlike the "simultaneous" techniques, it does suffer from the possibility that centroids corresponding to different pupil locations can be confused due to pupil movement. Therefore it is essential to monitor the pupil position with respect to the instrument. Re-imaging the beam spots on the retina back through the full pupil might introduce

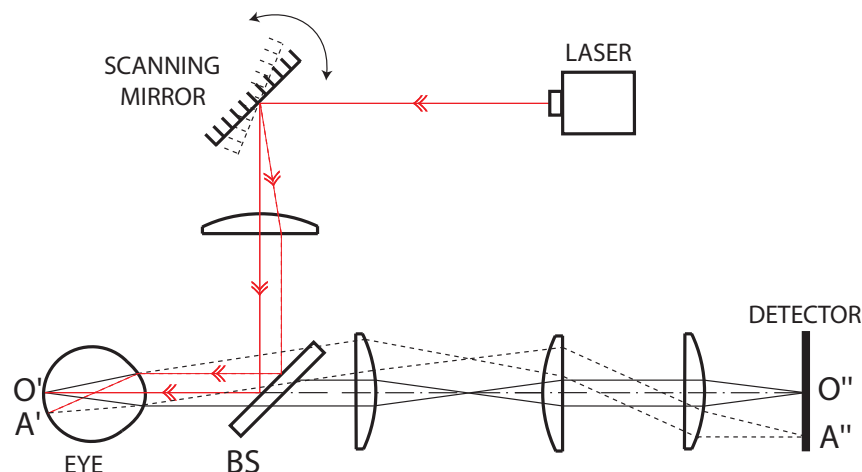


Figure 2.20: Schematic illustration of laser ray tracing aberrometry.

unwanted higher-order aberrations. To improve the image quality, one could slightly

reduce the pupil size by a diaphragm. If the pupil diameter is made so small that it is comparable to the beam size, then the effect of aberration cancelation of the beam traveling in double pass will ultimately limit this technique.

2.5.2 Spatially Resolved Refractometer

The spatially resolved refractometer (*SRR*), was developed by Webb and Penney [105, 106]. It is a subjective technique and consists of two light sources. The first one is a fixed source that acts as a reference (the light from which passes through the center of the pupil). The second source is a movable source the light from, which can be moved to a different location in the pupil. For each location of the movable source, the subject is asked to look at a target, while a light beam is projected into the eye at a specific sample position (similar to the laser ray-tracing method). Due to local aberrations the beam is deflected away from a focal point. The task for the subject is then to change the position of the movable light source on the retina (manipulator linked to an adjustable mirror) until it is aligned with the reference spot formed by the fixed light source. The same task is repeated at different locations of the movable source in the pupil plane and for each locus the incident beam has to be realigned by the subject. The local wavefront tilt can be derived then from incident beam-position correction given by the subject.

The disadvantage of this technique is of course fact that the overall performance depends on the subject's ability to precisely complete the task. The advantage is, that a measurement is achieved by a single optical pass.

2.5.3 Tscherning Aberrometer

Marius Tscherning, who developed this method at the end of the 19th century, used the planoconvex lens that projects an image of the grid on the retina (known as aberroscope). The distortion of the image of the grid after it passed through the optical system of the eye was an approximate evaluation of the ocular aberrations (mainly focus error, astigmatism and spherical aberration).

The example of modern version of Tscherning aberrometer (*TA*) is the one from Mierdel *et al.* [107]. A grid mask in front of the eye allows radiation to pass through only certain pupil positions (Fig. 2.21). As for the laser ray-tracing technique, the illuminated retina is re-imaged through the whole pupil. Provided aberrations are not very high, it is possible to identify which image point corresponds to what particular

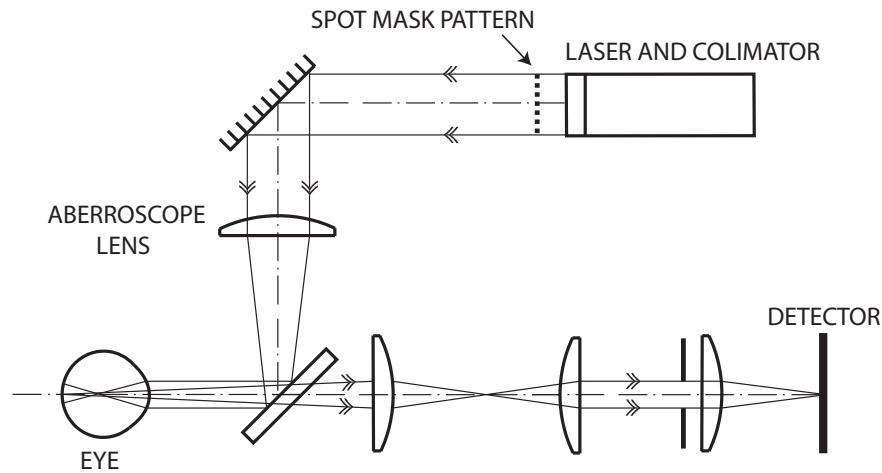


Figure 2.21: Schematic diagram of Tscherning aberrometry.

pupil position. To help reduce the problem for excessive amount of aberrations, the optical power of the aberroscope lens can be increased. Transverse aberration are determined by comparing the image positions with those of a reference schematic eye, which might induce some image scale errors because a real eye will have different image size compared to the paraxial image size in a schematic eye. Distortion present in a real eye might not be well represented by the schematic eye, which could limit the accuracy of the TA .

2.5.4 The Pyramid Wavefront Sensor

The pyramid wavefront sensor is relatively recent wavefront sensing technique, which has been developed by Roberto Ragazzoni in 1996 [108]. He proposed a setup that uses four-faceted glass pyramid with the analyzing beam rotating around its tip. This enables registration of four pupil images that are combined to estimate local wavefront slopes. In 2002 it was modified and applied to the human eye by Iglesias *et al.* [109]. One of the major modification was that they used an extended source instead of oscillating sensing beam, which was used before at the tip of the pyramid. It allows to vary the dynamic range by adjusting the amplitude of oscillation in the beam (or angular size of the source).

Figure 2.22 presents a schema of the principle of pyramid wavefront sensing technique. An aberrated wavefront (presented in red) is focused by a lens ($L1$) onto the tip of the pyramid prism and re-imaged into 4 sub-pupils at the detector by a lens ($L2$) [110]. Unlike in the case of non-aberrated wavefront, the distorted wavefront

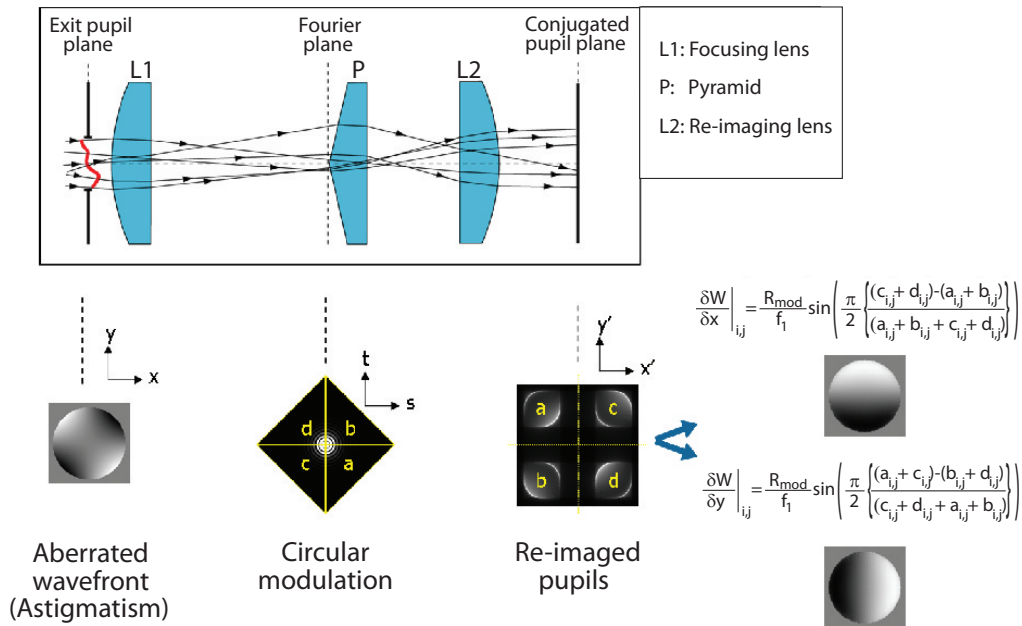


Figure 2.22: An example of operating regime of the pyramid P wavefront sensor with an aberrated wavefront (astigmatic mode) propagating through the optical system. Courtesy of S. Chamot and S. Chiesa [110].

results in non-zero intensity difference in the sub-pupils. The pixel-by-pixel intensity difference leads to obtain the local wavefront slope for the pupil element related to the pixel element.

The tip of the pyramid has to be very well manufactured, which is a technically hard to achieve due to very shallow angle (1-2 *degree*). Overall, as it has been recently reported, the pyramid wavefront sensor is a versatile instrument, which after very careful consideration of alignment and settings, performs an aberrations correction to the level of 0.1 μm RMS [111].

2.5.5 Shack-Hartmann Wavefront Sensor

In the beginning of 19th century Hartmann devised a method for measuring the ray aberrations of mirrors and lenses simply by inserting a metal disk perforated with holes near the pupil, which would isolate rays of light so they could be traced back [112]. Rays that go the "wrong" way are called aberrated rays, and so the Hartmann screen is a technique for measuring ray aberrations. Seventy years later Shack and Platt improved Hartmann screen by replacing the holes with an array of tiny

lenses [113]. Since that time a large number of papers have been published in this topic which demonstrated the efficiency and reliability of the Shack-Hartmann wavefront sensing technique. The work of Liang *et al.* from 1994, is the initial point for applying the Shack-Hartmann (*SH*) sensor in the eye [114]. Thanks to simplicity of *SH* wavefront sensor and ability to make fast and precise measurements of the ocular aberrations, shortly it became the preferred instrument for wavefront sensing in the eye.

Basically the sensor consists of a 2D array of lenslets with a focal length f , placed in the plane conjugated to the pupil of the eye, and the detector at the focal plane of the lenslet array. Each lenslet effectively samples the local gradient of the wavefront across the entire pupil of the eye. In the case of an optically perfect eye, a plane wavefront will produce a regular array of spots at the focal plane of the lenslets (Fig. 2.23), but the spots produced by an aberrated wavefront will in general be displaced from their unaberrated position (Fig. 2.24).

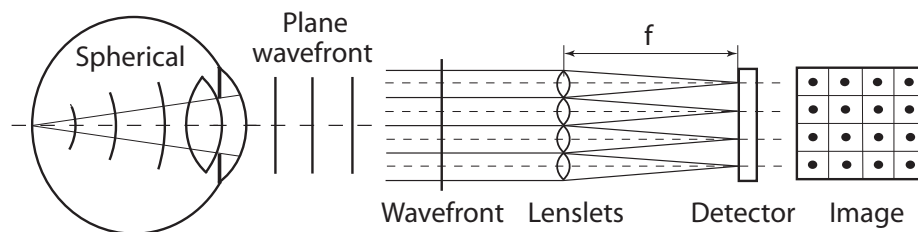


Figure 2.23: The Shack-Hartmann wavefront sensor (*SHWFS*) at a plane conjugated to the pupil measures the wavefront slope at discrete locations. For an aberration-free eye a regular array of spots will be formed at the focal plane.

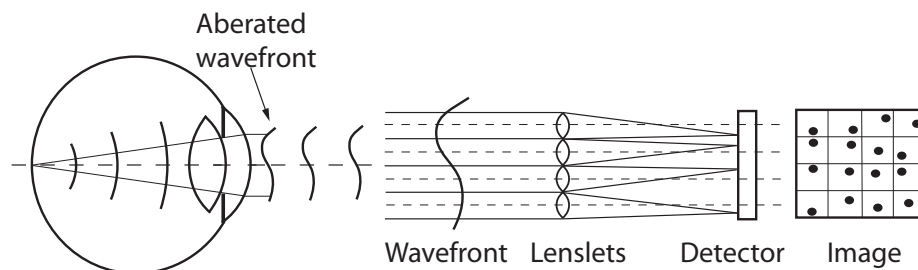


Figure 2.24: Aberrated wavefront comes out from the eye and enters the *SH WFS* and hence an irregular pattern of the *SH* spots is produced on the detector.

The displacement of each spot is proportional to the wavefront slope at the location of that lenslet in the pupil. A centroiding algorithm is used to locate x - and y - coordinates of the spots. The positions of the spots in the *SH* image are used then to

calculate the slopes of rays from the lenslet array in order to determine the wavefront aberration. The slopes and the wavefront are related as follows:

$$\frac{\delta W(x,y)}{\delta x} = \frac{\Delta x}{f}$$

and

$$\frac{\delta W(x,y)}{\delta y} = \frac{\Delta y}{f}. \quad (2.42)$$

In the Eq. 2.42 $W(x,y)$ is the wavefront with x and y being a horizontal and vertical coordinates on the pupil. Displacements of the spots on the detector, in respect to their reference locations, are represented by Δx and Δy and f is the distance between the *SH* lenslet array and the detector [115]. It shall be noticed here, that an alignment procedure and calibration method for the *SH* detector are critical for system operation in the open loop [9, 116].

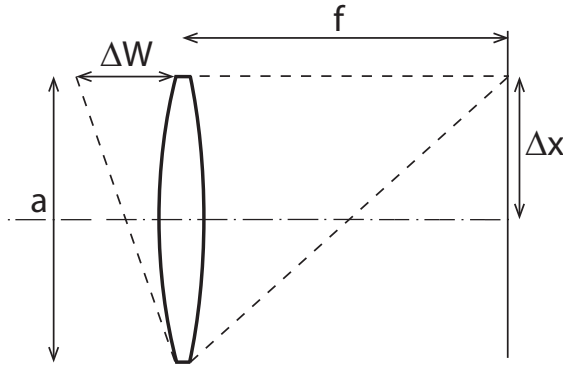


Figure 2.25: Relationship between the wavefront slope across single lenslet and the shift in the position of the *SH* spot [71].

Figure 2.25 illustrates a single lenslet with the diameter (a) and its focal length (f). The lenslet measures local wavefront slope, and according to a conventional algorithm, each spot is allocated within a virtual aperture directly behind its corresponding lenslet and equal to the size of the lenslet. This is so-called the dynamic range of the *SH* sensor and describing what is a maximum distance for single spot to the edge of its virtual aperture. Based on Eq. 2.42 we can estimate what is the maximum measurable wavefront slope:

$$\Delta W_{max} = \frac{a^2}{2f}. \quad (2.43)$$

The minimum slope, that can be measure (i.e. sensitivity of the sensor) is given by:

$$\Delta W_{min} = \frac{\Delta x_{min} a}{f}. \quad (2.44)$$

Designing of the *SH* wavefront sensor is always matter of balancing between a number of factors that play important role in general measurement performance of the sensor. From Eqs. 2.43 and 2.44 is clear to see, that for a given lenslet diameter (a), decreasing the focal length increases the dynamic range but decreases the measurement sensitivity. Furthermore, for a given focal length, decreasing the lenslet diameter decreases the dynamic range but increases sensitivity. Therefore the dynamic range of the *SH* wavefront sensor and its measurement sensitivity are inversely proportional to each other [71].

The *SH* sensing can be used as a part of an adaptive optics system to monitor and correct aberrations in the eye [9]. Another advantage of this technique is that it is quite robust to changes in eye position, as the software algorithm can be used to determine the pupil centre accurately, especially for the case with high sampling in the pupil. Spot overlapping due to high amount of aberrations or defocus is a major concern, that is, the instrument may have a limited dynamic range. One of the method to increase the dynamic range proposed recently by Charles Leroux is to gradually enlarge the number of spots participating in wavefront error estimation with the central (anchor) spot being fixed due to the double pass compensation [117].

2.5.6 Combined Wavefront and Corneal Topographer

Combined Shack-Hartmann (*SH*) aberrometer and corneal topographer seem to be evolutionary next step in the area of wavefront sensing in the human eye. Following the study of Zhou *et.al*, when they validated such a combined aberrometer [118], and work of Daniel Neal [119] we can list a number of advantages, that merge with this technique. First of all, the corneal topography measurements are integrated on same measurement axis as a *SH* aberrometer, which is the line of sight in the latter case. This is the recommended reference axis for predicting foveal image quality [120]. The *SH* instrument, because it measures both tangential and sagittal slopes of the cornea, is free from the "*skew-ray*" error, whereas in Placido's disk based topographers skew rays are not directly captured.

Figure 2.26 presents an optical layout of an exemplary set up of combined corneal to-

pographer and aberrometer based on Shack-Hartmann wavefront sensing [119]. This setup, contains a full gradient topographer, enables the separation of those aberrations of the cornea and from those of the rest of the eye, which is particularly important in terms of using experimental data for the eye modeling purpose. Moreover, such a combination of wavefront sensor with corneal topographer, allows the study of the aberrations of the crystalline lens, which could lead to better design and evaluation of intraocular lenses. Such a systems were validated, and a high accuracy in measuring corneal and whole eye wavefront aberrations was reported [118, 121]. Although satisfactory results have been already presented, there is still room for future work to be done.

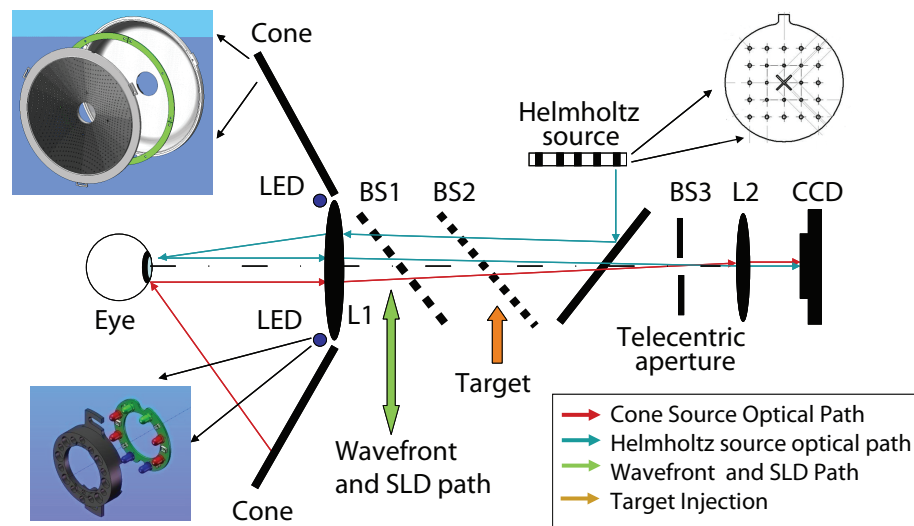


Figure 2.26: Optical layout of *iDesign*TM topographer as an example of combined corneal topographer and aberrometer based on Shack-Hartmann wavefront sensing. Courtesy of Daniel Neal [119].

Chapter 3

On-axis and Off-axis Aberrations of the Human Eye

In Chapter 2, we introduced the background for the study of the optical properties of the eye, giving a short description of aberration theory and its mathematical representation, as well as wavefront measurement techniques for ocular aberrations. Here, in Chapter 3, we explore the impact of different types of ocular aberrations in the central 10 *degree* of visual field (see Fig. 3.1), using a dedicated aberrometer that measures the total wave aberration in terms of the first 20 Zernike polynomials. The strength of each aberration term is assessed as a fraction of the total *RMS* wavefront error. We analyse the contribution of the lower-order and higher-order aberrations for the horizontal and vertical meridians in 25 young healthy human eyes. We found that astigmatism and field curvature (field dependent focus error) have the largest contributions to the field-dependence of the wavefront error. Our experimental findings show the significance of astigmatism and field curvature contribution to ocular aberrations and their rapid change even at small off-axis angles (3-5 *degree*). We emphasize the importance of correcting these field aberrations in the future retinal imaging instruments.

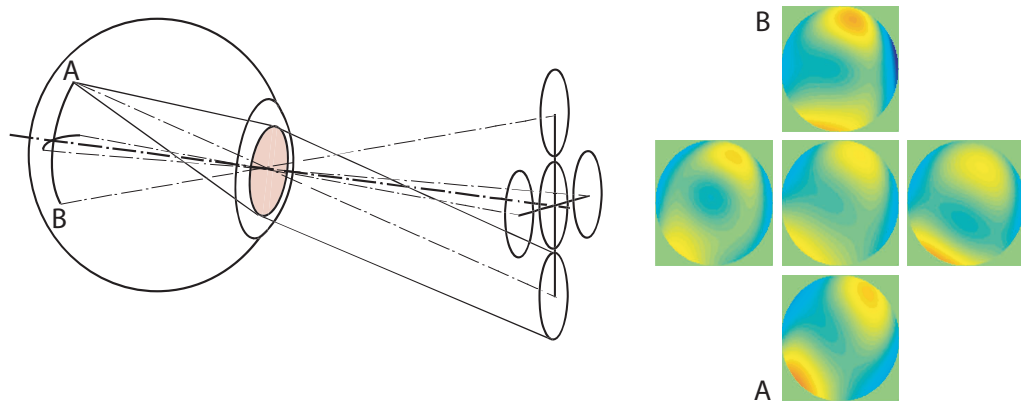


Figure 3.1: Schematic optical layout of the human eye with five probing beams and corresponding phase maps that show the amount of wave aberrations measured in the eye.

3.1 Literature Review

The human eye suffers from various ocular aberrations which, apart from degrading image formation on the retina, can limit some other visual functions such as contrast sensitivity [122] and detection acuity [123]. There are different types of aberrations including lower-order and higher-order errors and furthermore both types depend upon a variety of factors. Applegate *et al.* gave a description of higher-order aberrations as a function of pupil diameter and age [87]. They measured 146 eyes (divided into six age-groups), using a custom built Shack-Hartmann (*SH*) wavefront sensor. A complete review on comparison various number of studies on aberrations and myopia has been given in 2005 by Charman [124]. Some other work has been done to evaluate the distribution of the ocular aberrations within a large population of healthy eyes. The population studies, among the others, include those of Porter *et al.*, where 218 human eyes (measurements over 5.7 mm pupil diameter) from 109 normal subjects were investigated [125], Thibos and colleagues, who studied 200 cycloplegic eyes (eyes with paralyzed accommodation) and calculated the wavefront aberration for a 6 mm pupil size [126], the work of Castejón-Mochón *et.al*, where the wavefront aberration was measured over a 5 mm pupil for 108 eyes from young and healthy population [127]. All the above population studies were performed using an aberrometry technique based on *SH* principle. The conclusion common to the above population studies is that there is high inter-subject variability of the wave aberrations although the average amplitudes of the higher-order terms (except for spherical aberration term) tend to oscillate around zero. Another common conclusion is that

the strongest contribution to the total *RMS* wavefront error comes from the second order Zernike aberrations [126, 127]. Some other conclusions arose like for example the existence of mirror symmetry between the left and right eyes [9, 125]. The recent work of Plainis and Palikaris from 2008 is a confirmation of previous population studies as they found that an average of 393 eyes (age range of 33 ± 5 years) is zero for all Zernike aberration terms except for spherical aberration and oblique-oriented trefoil coma [128].

There have been a few studies to analyze ocular aberrations across the field. Navarro *et al.* investigated a wide field of view (± 40 degree in horizontal and vertical meridian) [129]. They found that the lower-order aberrations have the major impact on the total *RMS* wavefront error. Shortly afterwards, Atchison and Scott published a paper which showed that the contribution of third-order Zernike aberrations to the *RMS* aberration increased up to four times from the center to the edge of a 40 degree field [130]. In contrast, the contribution of fourth- to sixth-order Zernike aberrations varied little across the visual field. A recent study by Lundström *et al.* showed the impact of different degrees of optical correction on acuity in the peripheral field [131]. The data they collected indicates that the Zernike terms at larger angles were defocus and astigmatism (with- and against-the-rule). Atchison *et al.* [132], published a study where the refraction and aberrations of the eye of 8 subjects were measured across the horizontal central 10 degree visual field. Their results showed evidence for some subtle changes in refraction (under a cycloplegic conditions) across the horizontal central 10 degree, however a correlation between these changes and retinal thickness was excluded. The need for correct foveal alignment during measurements was emphasized. Furthermore, in terms of the distribution of higher-order aberrations within the central visual field only horizontal coma was found significantly varying within the field. Another recent work by Mathur *et al.*, where a central visual field (42x32 degree (horizontal/vertical)) of 5 young emmetropic eyes were investigated, proved consistency with the Seidel theory of measured quadratic field dependence of the astigmatism coefficients and linear field dependence of the coma coefficients. However, defocus in the form of field curvature did not follow theoretical predictions [133]. One of the latest studies covering the age-dependent aspect of ocular aberrations across the horizontal field revealed that the horizontal coma undergoes significant change with age and in addition, spherical aberration shows a positive shift with increasing age [134, 135].

The interpretation of the field aberrations is difficult because of the complex nature of ocular aberrations. This is due to the lack of rotational symmetry of the eye, irregular

shape of the cornea, pupil decentration, and the crystalline lens and its gradient-index structure. Furthermore, the cornea and the lens themselves display tilts and mutual decentrations which cause a deviation of the visual axis from the optical axis of the eye (i.e. angle alpha (α)) which is approximately 5 *degree* horizontally and 2 *degree* vertically [132].

The knowledge about how aberrations of the optical components of the entire eye are distributed across the visual field, leads us to an important subject: the anisoplanatism of the human eye. This topic is extremely relevant for conventional adaptive optics (AO) and its performance. The first complete AO system was built in 1997 by Liang *et al.* [136]. Although the AO technique enables us to gather high-resolution retinal images, it can be done only over small field called the "*isoplanatic patch*" [137]. This implies limitations for AO systems, since a clear image of the retina for instance, can only be obtained over a narrow field for which a correction was implemented. When going away from this point on the retina, we leave the isoplanatic patch of relatively constant amount of aberrations and enter to another region where we deal with different wavefront degradation, so the image is distorted. Only few studies have been done so far on the anisoplanatism of the human eye. In 2008 Bedggood and colleagues published a paper when they reported the isoplanatic patch to be around 0.8 *degree* at the fovea [138]. The same year brought another publication by Dubinin *et al.*, where the angular size of the zone of constant wavefront aberrations was presented as varying from 1.5 to 2.5 *degree* [139]. It would be fair to say here, that this topic still requires more work to be done and we shall discuss this aspect later in this Chapter.

A relevant matter to point here is that the general use of Seidel aberration theory in non-rotational symmetric systems might not be applicable in the human eye case. The main objective of Chapter 3 is to investigate the field dependence of the ocular aberrations within young population over a 10 *degree* field of view. Using Zernike coefficients to describe the wavefront error for a 6 *mm* pupil we do not make any paraxial approximation as in the earlier calculations of the peripheral astigmatism [45, 140]. It is worth noting that we are concerned about the difference between the on-axis and off-axis values for astigmatism and defocus. This is of great importance for optical design of ophthalmic imaging instruments for the central 10 *degree* field.

3.2 The Experiment

3.2.1 The Optical Setup

We have measured the wavefront aberrations in the pupil plane with an aberrometer incorporating a Shack-Hartmann (*SH*) sensor and equipped with a system that controls the pupil position and fixation channel featuring nine field points across vertical and horizontal meridians.

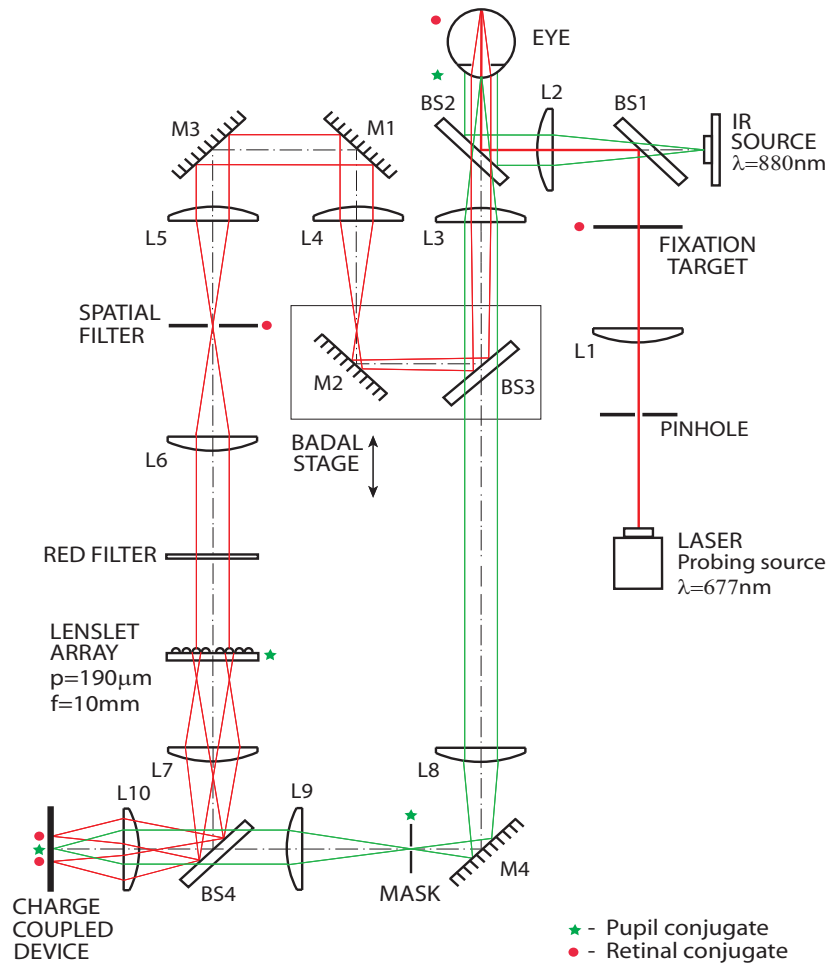


Figure 3.2: Schematic diagram of the aberrometer optical layout used in the experiment. Rays of light shown in red are going through the sensing arm, whereas green rays show an optical design of aligning arm of the aberrometer. Notation: L1-focusing lens, L2-collimating lens, BS2-pellicle beamsplitter, L3-Badal focusing lens, BS3,M2-Badal pick-off mirrors, L4-Badal collimating lens, M1,M2,M3,M4-plane mirrors L5,L6-pupil re-imaging lenses, L7-S-H pattern re-imaging lens, L8,L9-alignment channel re-imaging lenses, BS4-dichroic beamsplitter, L10-focusing lens.

Figure 3.2 presents the sketch of the aberrometer layout. The instrument was designed and built by Matthew Sheehan in the Applied Optics Group at National University of Ireland Galway and more technical details can be found here [141,142]. We give only a brief overview of the instrument highlighting its major and most important properties.

Pupil Alignment Channel

The pupil alignment channel (green rays sketched in Fig. 3.2) allows the pupil centre to be determined independently of the SH spots. After alignment, the pupil centre defines the origin of the polar coordinate system to which the Zernike polynomials are fitted. The pupil alignment channel uses an 880 nm infrared LED to illuminate the iris of the eye. The magnification of the alignment channel is 0.66 and this magnification value was selected to balance the concerns of creating the largest field of view possible, maximizing image resolution. The instrument works with pupil diameters ranging from 6 mm to 10 mm. The pupil centre is found by analyzing the image of the iris with an edge-detection algorithm. The edge-detection algorithm is used then in built-in pupil tracker which, after the pupil is aligned with the optical system, recognizes the pupil edge and follows lateral movements of the pupil (the red circle in Fig. 3.3). In post-processing procedure Zernike polynomials are recalculated for different positions of the pupil as the pupil might slightly drift during measurement changing coordinates of its center.

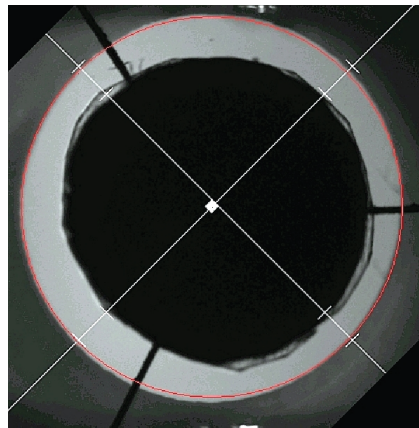


Figure 3.3: The image of the entrance pupil of the eye in the alignment channel.

Sensing Channel

In the sensing channel (rays path showed in red on the Fig. 3.2), the laser source (wavelength 677 nm) is used to form a collimated, narrow beam entering the eye and creating a reference spot on the retina. The diameter of the laser beam is around 1.5 mm and the power level does not exceed $1.5\ \mu\text{W}$. The light reflects and scatters back from the surface of the retina and comes back to the instrument, through the dilated pupil, bringing information about aberrations of the eye's components. After the laser beam leaves the eye it passes a Badal stage, which creates an additional positive or negative sphere to correct the defocus term of the eye. Next, the probing beam goes through Shack-Hartmann wavefront sensor (*SHWS*), and finally hits the *CCD* detector. The aberrated wavefront is reconstructed by using a least squares fit to obtain the Zernike coefficients. The optical design includes a lenslet array rotated by 45 degree around the optical axis. This increases the dynamic range in those meridians where astigmatism is typically expected in the eye. The lenslet array is conjugate to the subject's pupil with a *CCD* detector on its focal plane. The spatial sampling of the apparatus is 16 lenslets across a 6 mm pupil diameter (190 micron pitch).

The novelty of this design is the simultaneous acquisition of the image of the pupil and the *SH* spots pattern by using only one detector (*CCD*). This is obtained by incorporating a "spider" mask, which blocks all unwanted infra-red light reflected from the retina but permits the recording grid of *SH* spots and tracks the pupil edge (see Fig. 3.4, and Fig. 3.2). Reconstruction of the aberrated wavefront is achieved by using the Zernike circle polynomials, which are obtained with a least-squares fit.

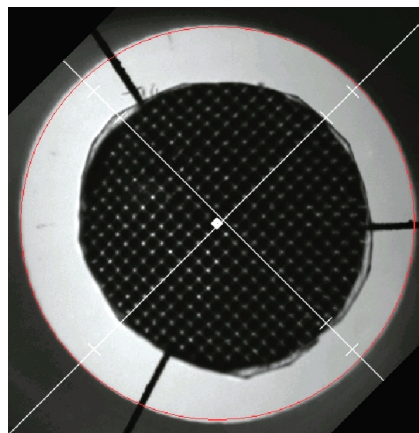


Figure 3.4: The image of the *SH* pattern in the pupil plane.

Calibration of the Aberrometer

Our Shack-Hartmann sensor based aberrometer, built by Matthew Sheehan [141], was verified by measurements of 60 normal eyes from young population [142]. The results were compared to these obtained from one of the commercial aberrometers (Zy-Wave) in terms of measured set of Zernike coefficients. Comparison between residual higher-order *RMS* wavefront values and standard deviation error of recorded Zernike coefficients of the experimental wavefront sensor (*WFS*) and the ZyWave aberrometer was then performed. Comparative analysis provided confidence in repeatability of the experimental *WFS* measurements and demonstrated results similar to those achieved by a commercial instrument.

Before the experiment was carried out, additional methods of validation were implemented. Firstly, the optical setup of the aberrometer was calibrated with phase plates, kindly supplied by Prof S. Bará. The phase plates with fixed amount of Zernike aberrations, (more technical details can be found [143]), were measured by using an interferometric technique, as well as with the experimental aberrometer setup. The commercial interferometer (Fisba Optik), based on the Twyman-Green technique, measures the reference phase plate in a double-pass regime at a wavelength of $632.8 \mu\text{m}$. In the double-pass method, one has to divide the measured wavefront by 2, in order to make it comparable with the aberrometer measurements. A physical stop was added to the phase plate to assure that the interferogram is obtained for the same region as with an aberrometer (over a 6 mm pupil diameter). The software of the Fisba interferometer allowed us to calculate the Zernike aberration polynomials up to 5^{th} order using the same definition of Zernike polynomials as it is standardized in [68], and used in this thesis for presenting ocular Zernike wavefront aberrations. Figure 3.5 presents results of the calibration procedure in the form of the interferogram and wavefront map of the measured phase plate no. 1, which represents the amount of aberrations present in a typical eye. The plot presented in Fig. 3.5 shows the amplitude of the first 18 Zernike aberration coefficients (tip/tilt removed), used for the reconstruction of the wavefront, as the comparison between both measurement techniques. One can see that the amplitude and sign of all Zernike coefficients, are in good agreement although there are few points where the two curves do not match exactly.

Two Zernike aberration coefficients that differ the most in amplitude are: oblique astigmatism $c(2,-2)$ with $0.053 \mu\text{m}$ difference, horizontal/vertical astigmatism $c(2,2)$ with $0.065 \mu\text{m}$ difference and vertical coma coefficient $c(3,-1)$ with $0.066 \mu\text{m}$ difference. These mismatches corresponds to a *RMS* error of $\lambda/11$ at a wavelength of

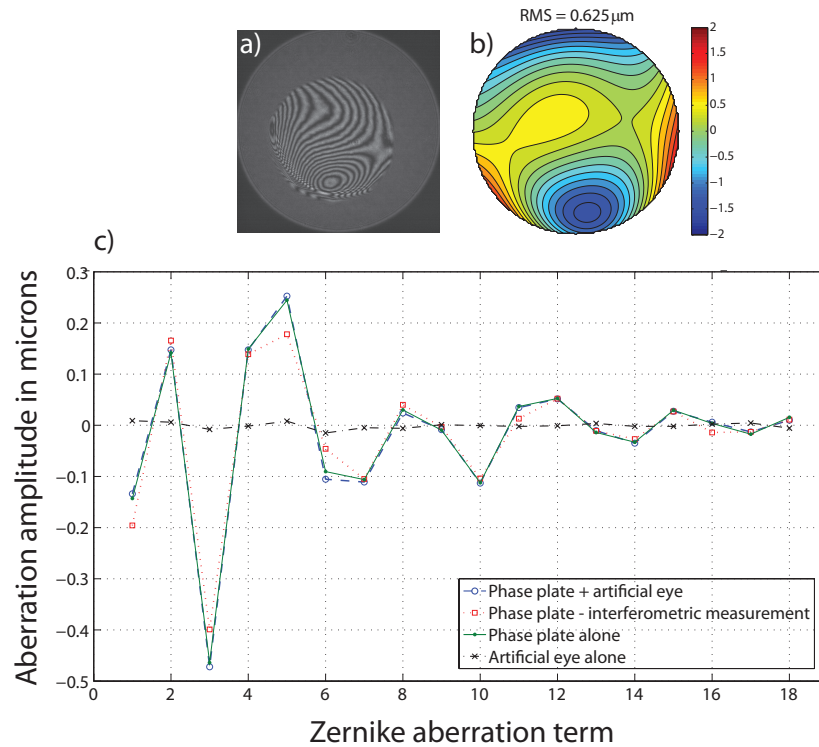


Figure 3.5: Results of the calibration of the system. a) An interferogram of the phase plate no. 1, obtained with a commercial double-pass interferometer b) Measured wavefront of the phase plate no. 1 from the aberrometer, over 6 mm pupil (tip/tilt removed) c) Amplitude of Zernike aberration coefficients obtained from interferometry measurement and from the aberrometer measurement. For the sake of clarity, error bars have been omitted.

$0.677 \mu\text{m}$, which can be regarded as typical error budget for an aberrometry measurements [144]. This can be attributed to small rotational misalignment relative to each sensor. We neglected a fact of varies wavelength of used instruments, since small wavelength difference (44.2 nm), and nearly stationary nature of higher-order aberrations in the near infrared region [145], should not give any noticeable offset. Measurement of the phase plate no. 1, which represented typical ocular aberrations of the eye, required incorporation of the phase plate to an artificial eye (AE), which serves as a reference during alignment. The artificial eye contains of diaphragm (pupil), achromatic doublet lens $f = 50 \text{ mm}$ (optics) and a piece of white paper as reflection medium (retina). The values of Zernike coefficients ($2^{\text{nd}} - 5^{\text{th}}$ order) of the AE were then subtracted from coefficients obtained from the phase plate and the AE measured together (blue, dashed line in Fig. 3.5) in order to obtain coefficients for the phase plate only (green line in Fig. 3.5). An averaged RMS wavefront error of the AE is

equal to $0.025 \pm 0.001 \mu m$, which corresponds to a *RMS* error of $\lambda/27$ at a wavelength of $0.677 \mu m$, which indicates a small level of intrinsic aberration noise of the instrument.

These type of errors often appear when comparing two (or more) sensors as an effect of mismatch between coordinate systems. In order to numerically cancel such alignment errors between wavefronts represented by the Zernike polynomials a new method has been developed recently [146].

Repeatability Test of the Aberrometer

It is important to study the systematic error that might occur when measuring ocular aberration in a real subject after consecutive realignment procedures (subject is realigned with the instrument after each measurement). The human eye, as a living part of our body, exhibits some fluctuations of the parameters such as: intra-ocular pressure, axial length, corneal shape, accommodation and ocular aberrations. Some parameters are related to blood pressure, heart beating frequency, the tear film variability on the cornea surface or overall condition of the body. These factors may affect the eye-ball with different frequency or time scale. Logically, all the changes within the eye should impact the overall performance of the optical system of the eye. Some work has been done on evaluation of microfluctuations of the accommodation and aberrations. Within a short period of time, experimental data shows a maximum frequency of fluctuation of 5 Hz [147], and similarly for the long period of time (days, months, years) aberrations indicate a significant lack of stability [88]. According to the recent findings of Leahy *et al.* [148], the statistical nature of the fluctuations in accommodation were shown to be dependent on the mean level of accommodative effort.

In addition, other sources of errors are present during the wavefront measurements as a result of head or eye movements or misalignment of the eye with respect to the optical axis of an aberrometer. It can affect the final results, decreasing repeatability and thus the reliability of any eye-testing apparatus. The repeatability of any sensing system is the ability to repeat its own results or, very often, it is defined as the variation in measurements on the same subject, under the same condition in the same measurement session. In order to evaluate repeatability of our instrument, we measured the right eye of subject no. 18 under cycloplegic condition. The subject was asked to fixate his eye on the central point of the fixation target and, after alignment, 20 single frames (wavefronts) were taken over the time period of 3 *seconds*. This rep-

resents one single trial, which we call a single measurement of the eye's wavefront error. After each single measurement, subject was realigned and the procedure was performed again until the total number of single measurements of 12 was reached.

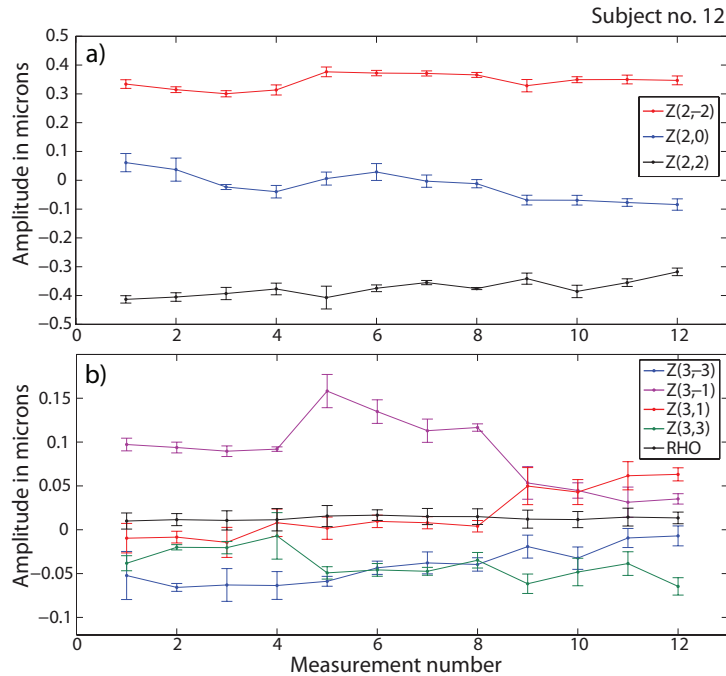


Figure 3.6: Repeatability test on the aberrometer. Amplitude in microns measured over 12 single measurements ± 1 SD of subject no. 12, under cycloplegic condition. Plot Note: the scale differs between case (a) and (b).

Figure 3.6 shows how a single Zernike coefficient fluctuated over 12 single measurements. Case (a) presents a plot for lower-order terms. The three Zernike coefficients have a fluctuation of amplitude: the defocus aberration coefficient ($c(2,0)$) varies within $0.15 \mu\text{m}$ and two components of astigmatism ($c(2,-2)$ and $c(2,2)$) do not exceed $0.1 \mu\text{m}$ of the fluctuation range. Note, the Badal optometer was set to minimize the defocus term, before the test was carried out. From the higher-order aberration (case (b)), we show four single terms, fluctuating significantly, and the remaining higher-order terms (RHO) with minimum oscillation around zero. Vertical coma coefficient $c(3,-1)$ exhibits the largest variation of $0.13 \mu\text{m}$, whereas horizontal coma coefficient $c(3,1)$ and both components of trefoil coma $c(3,3)$ and $c(3,-3)$ indicate oscillation within the range of $0.08 \mu\text{m}$. Here we shall be aware, that all measurements were performed on a real eye, and therefore suffers a number of complicating factors (such as temporal fluctuations in aberrations, tear film or alignment mismatches).

Table 3.1 presents mean values for all 18 Zernike coefficients up to the 5th order and the coefficient of variation (c_v) for each coefficient used in the test. The standard deviation (SD) of the 12 repeated measurements was also determined. In order to obtain the c_v for individual Zernike coefficient the SD of the mean were divided by the mean and multiplied by 100 to give a percentage [149]. The percentage of the c_v shows variation for each Zernike coefficient in respect to the mean value. In order to minimize fluctuations of the Zernike coefficients due to the consecutive realignment, subject's eye realignment procedure during a measurement session was limited to a necessary minimum.

Table 3.1: Subject no. 18, right eye. Repeatability of 12 single on-axis measurements after consecutive re-alignment.

Zernike coeff.	Magnitude of aberration Mean \pm $SD[\mu m]$	c_v [%]
c(2,-2)	0.344 \pm 0.013	3.8
c(2,0)	0.043 \pm 0.021	49
c(2,2)	0.375 \pm 0.017	4.5
c(3,-3)	0.044 \pm 0.012	27
c(3,-1)	0.088 \pm 0.010	11.4
c(3,1)	0.018 \pm 0.012	67
c(3,3)	0.040 \pm 0.010	25
c(4,-4)	0.014 \pm 0.012	85
c(4,-2)	0.020 \pm 0.009	45
c(4,0)	0.073 \pm 0.007	9.6
c(4,2)	0.017 \pm 0.010	58
c(4,4)	0.055 \pm 0.009	16.4
c(5,-5)	0.024 \pm 0.011	46
c(5,-3)	0.028 \pm 0.007	25
c(5,-1)	0.012 \pm 0.006	50
c(5,1)	0.051 \pm 0.008	16
c(5,3)	0.022 \pm 0.007	32
c(5,5)	0.007 \pm 0.009	128

3.2.2 The Experimental Procedure

In our study, 25 healthy eyes from young population (12 female, 13 male) without any optical abnormalities, were measured. The subjects ranged in age between 23 and 34

years had a mean value of 27 years. Spherical refraction in our population is in the range from 0 D to -2.25 D (with a mean of -0.55 D) and up to 0.75 D in cylinder (see Table 3.2 for details). All subjects have not undergone any kind of refractive surgery (healthy eyes). Prior the experiment each subject went through a pre-screening test at the University College Hospital, Galway to check on their vision and ocular condition. The project was granted ethical approval by the National University of Ireland, Galway Research Ethics Committee.

Table 3.2: Subjects record for right eye (OD).

Subject number	Year of birth	Gender [M or F]	Refraction spherical [D]	Refraction cylinder [D]
1	1983	M	-0.75	+0.25
2	1983	F	0	+0.5
3	1983	F	-0.75	+0.75
4	1978	F	-0.25	+0.25
5	1984	M	-1.75	+0.25
6	1980	F	-0.25	+0.25
7	1980	F	-0.5	-1.0
8	1978	M	-1.25	+0.25
9	1984	F	-1.0	0
10	1974	M	-1.0	+0.75
11	1983	F	-2.25	+0.5
12	1984	M	0	0
13	1983	F	0	0
14	1978	M	-0.25	-0.5
15	1983	F	-0.5	0
16	1980	M	0	+0.75
17	1979	F	-0.75	-0.5
18	1983	M	-1.5	-0.5
19	1979	F	0	0
20	1985	F	-0.25	-0.25
21	1982	M	0	+0.5
22	1978	M	-0.25	-0.25
23	1983	M	0	0
24	1985	M	0	-0.25
25	1978	F	0	0

One drop of 1 percent Tropicamide was administered to the subject's right eye in order to dilate the pupil and to paralyze the accommodation. After 15 minutes each subject

was positioned against the chin-rest and forehead-rest and aligned with the wavefront sensor. The subject did not wear any contact lenses or glasses. In the optical layout of our aberrometer, the sensing beam is always pointing at the same point on the retina when the eye is well aligned with the system. To obtain an off-axis measurement subject is asked to fixate their eye at one point on a fixation target as shown in Fig. 3.7. A small ring in the fixation target corresponds to 3 *degree* and the peripheral ring corresponds to 5 *degree* with respect to the central point. This arrangement enables us to measure wave aberrations of the eye within 10 *degree* (horizontally and vertically) of the field of view with respect to the line of sight.

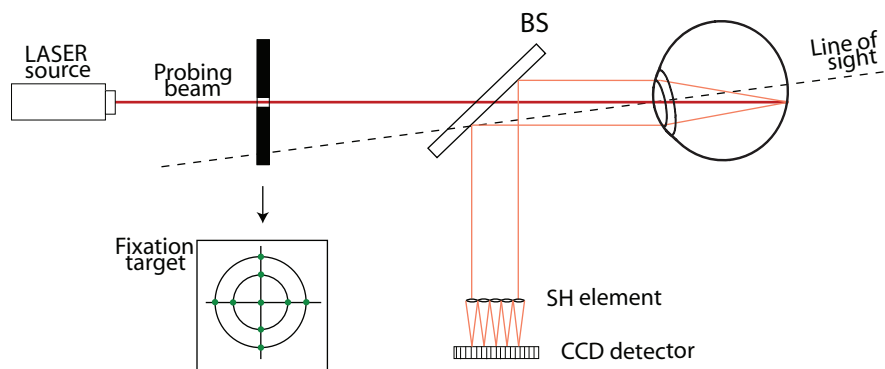


Figure 3.7: Schematic layout of the off-axis measurement procedure. The probing beam creates a reference spot of light at the center of the fovea when the eye is aligned with the optical axis of the aberrometer. In order to obtain off-axis measurements, a subject is asked to fixate at each of 8 field points displayed on the fixation target.

At the start of the experimental session, the Badal optometer is set for the best sphere to minimize the defocus aberration term on-axis. Once the eye is aligned with the aberrometer the pupil tracking system locks on the image of the iris and follows the lateral movements of the eye. This arrangement is necessary to ensure that the aberrated wavefront is always measured with respect to the center of the pupil. We measure the wavefront in the pupil plane of the eye at 9 different points in the field including the on-axis reference measurement. Three single measurements are taken for each field point to reduce the optical effect of the tear film. One single measurement consists of 20 single frames taken with a given exposure time for a CCD camera. The exposure time for a single frame depends on quality or brightness of the SH spot; generally it is around 80 *ms*, hence on average a single measurement lasts around 3 *s* (additional 1.5 *s* for recording (acquiring) the frames into the system). Measurements with a blink during the frame grabbing process or with eye movements, that exceed the range of the pupil tracker, were excluded from the study. To improve fixation skill

each subject had an opportunity to practice their ability to fixate properly at a different target point. In the following section we present data for 25 eyes measured with our method under the same conditions.

3.3 Experimental Results

Before we present our experimental results we shall describe the standards for reporting ocular aberrations in the eye, that we use in this thesis. The recommendation of the Optical Society of America (OSA) standards state that wavefront aberrations shall be reported from the examiner's point of view as it is outlined in Fig. 3.8. When detecting the wavefront in the exit pupil of the subject, positive phase/wavefront values represent a phase-advanced wavefront and similarly, negative values represent a phase-retarded wavefront. According to the OSA standards, we shall use Zernike polynomial coefficients for describing ocular aberrations for the wavefront conjugated to the pupil plane and with the reference axis defined along the line of sight [120].

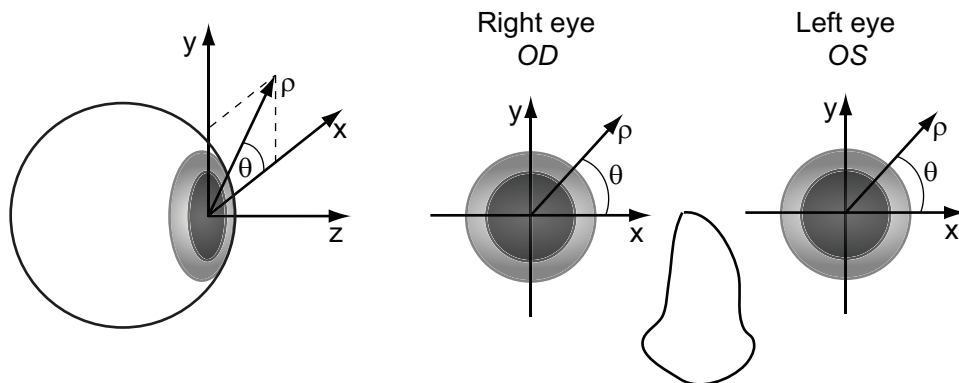


Figure 3.8: Conventional right-handed coordinate system for reporting ocular aberrations. Examiner's view of subject. Oculus dexter (OD) is a Latin term meaning "right eye" and oculus sinister (OS) is a Latin term meaning "left eye", both Latin terms are in common use in ophthalmic nomenclature.

3.3.1 Young Population Study

Figure 3.9 presents the mean value of each Zernike coefficient (obtained from the 3rd up to the 20th Zernike coefficient in microns as tip and tilt are removed from calculation) with its sign across a 25 measured eyes as a detailed composition of the

wavefront aberrations measured at five field points in horizontal and vertical meridians. For clarity we show only a central (reference) 0 degree point and a four other field-points correspond to a peripherals 5 degree field of view (we did not plot the data for 3 degree visual field to keep this illustration less crowded). This type of averaging (where the sign of the coefficients was taken into account), for any aberration showing small variation around zero leads to compensation in their average estimation i.e. tending towards Zernike mean. For a quantitative illustration, an average of the absolute values of each Zernike coefficient (for a 6 mm pupil diameter) across the population was calculated and plotted on Fig. 3.10.

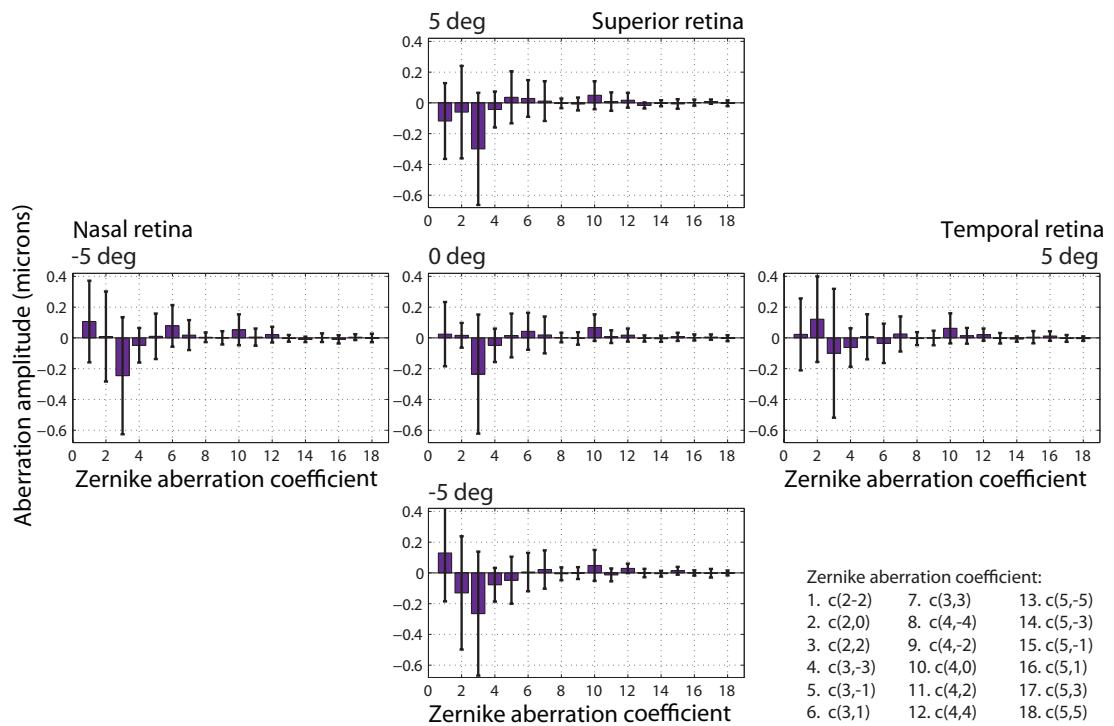


Figure 3.9: Population study of 25 young eyes. Mean values for each Zernike coefficient (given in microns for a 6 mm pupil diameter) of the 25 measured eyes, up to 5th level. Error bars are ± 1 standard deviation. Note, that Zernike defocus aberration was corrected by the Badal optometer on-axis.

From Figs. 3.9 and 3.10 it is clearly seen, that the major contribution to the total amount of the wavefront error comes from three types of refractive errors: defocus $Z(2,0) = \sqrt{3}(2\rho^2 - 1)$, second order astigmatism (90 - 180 degree with-the-rule astigmatism) $Z(2,2) = \sqrt{6}(\rho^2 \cos 2\theta)$, and oblique astigmatism (45 - 135 degree against-the-rule astigmatism) $Z(2,-2) = \sqrt{6}(\sin 2\theta)$, where ρ is the normalized radial coordinate in the pupil and θ is the azimuthal angle measured counter clockwise from

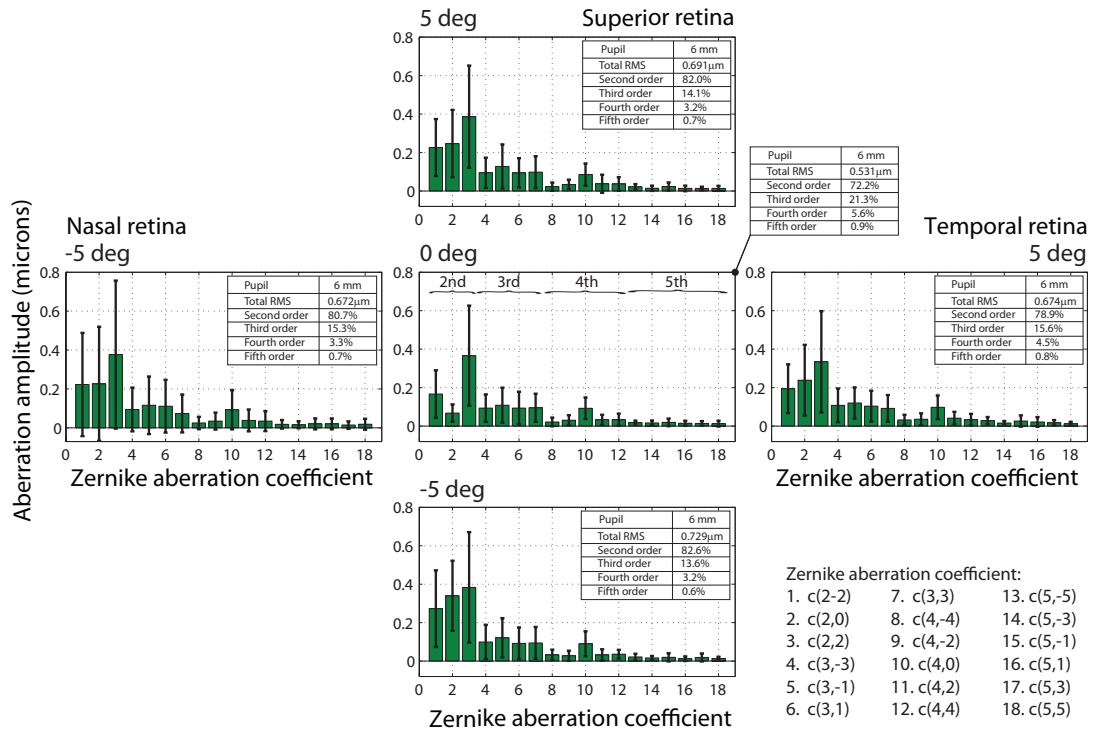


Figure 3.10: Population study of 25 young eyes. Mean absolute values of the Zernike coefficients from the 2nd to the 5th order (given in microns for 6 mm pupil diameter). Error bars are ± 1 standard deviation. Note, that Zernike defocus aberration was corrected by the Badal optometer on-axis. Percentages (given in tables) were obtained by averaging the percentage of each subject for each coefficient.

the horizontal axis (+ x axis). The θ angle is known as the "meridian" in ophthalmic optics. Large magnitude of the Zernike $c(2,2)$ aberration coefficient indicates a predominant with-the-rule astigmatism in the population. The negative value of $c(2,2)$ (see Fig. 3.9) is a typical situation in the eye where the corneal surface is steeper along the vertical meridian than along the horizontal meridian. This has been reported earlier [125, 142, 150].

Within the higher-order aberrations the averaged vertical coma coefficient $c(3,-1)$ appears to be close to zero in the horizontal meridian, whereas the horizontal coma $c(3,1)$ shows little variation around zero in the vertical meridians. There are other significant higher-order terms. Some of them do not vary much with the field angle such as spherical aberration coefficient $c(4,0)$ and one of the trefoil coma component $c(3,-3)$ with approximately the same absolute mean value as $c(4,0)$ and horizontal trefoil coma component $c(3,3)$. Although, the horizontal trefoil coma varies a lot in sign from subject to subject and hence its influence is diminished in the averaged values

in Fig. 3.9. The presence of the nearly constant trefoil coma component indicates that the origin of this aberration lies in proximity to the pupil. The crystalline lens with its specific Y-like fibre cell organization [151] might be responsible for this effect [126].

In order to define the weight of each Zernike coefficient in the total *RMS* wavefront error, we calculated a percentage factor, c_j using formula below:

$$\frac{c_j^2}{\sum_i^{18} c_i^2} \times 100. \quad (3.1)$$

The value in denominator represents the variance of the ocular wavefront aberration obtained for first 18 Zernike coefficients (tip and tilt removed). Calculated percentages were obtained by averaging the percentage of each subject for each coefficient. The data of the percentage and mean total *RMS* value are shown in tables in Fig. 3.10. The tables show the distribution of the mean-total *RMS* across 10 *degree* visual field and the impact of each Zernike order, given in percentages, on the total *RMS* wavefront error. Similar to Thibos *et al.* [120] we regrouped Zernike coefficients and hence 2nd order terms represents the lower-order aberration with index from 3 to 5, and higher-order aberrations are distributed to the three orders such as 3rd order (index 6 to 9), 4th order (index 10 to 14), and finally 5th order (index 15 to 20).

From Fig. 3.11 it can be clearly seen that the total *RMS* increasing its value as going off-axis (both meridians), and this is what one could expect from field decomposition of ocular aberrations. As we have already mentioned lower-order aberration terms give the strongest contribution to the total amount of ocular aberrations (2nd order terms mimic the distribution curve for the total wavefront error across the field). Moving of axis second-order terms (especially both components of astigmatism) increase its amplitude and hence there is clear increase of the total wavefront error. The 3rd order terms do not change dramatically with the field angle, however they contribute about 15 *percent* to the total amount of the *RMS* across the field (see Fig. 3.10). The 4th order terms have very little impact, and in fact the spherical aberration coefficient $c(4,0)$ is only one significant term within this group (see Fig. 3.10). As we have stated before, the spherical aberration does not change with the field by definition. The 5th order term have no impact for the total amount of wavefront ocular aberration. All observations presented above clearly support the previous studies [125–127, 129, 142, 150].

In our analysis of ocular aberrations, we are going to consider only those groups of Zernike coefficients, which significantly contribute to the total wavefront error. These

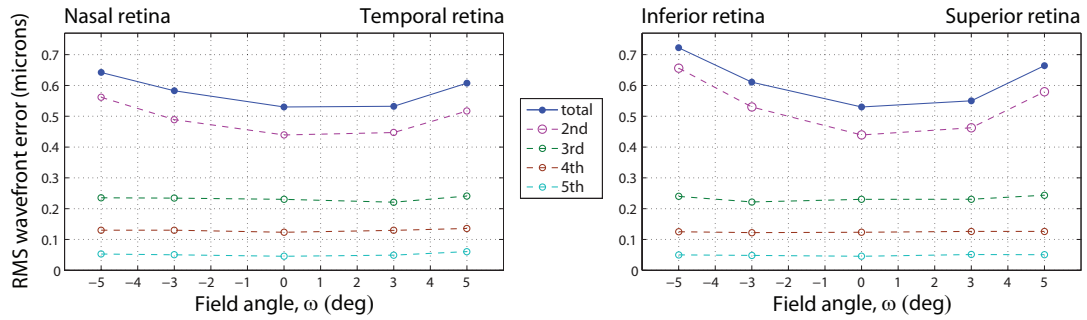


Figure 3.11: Mean *RMS* wavefront error (in microns) in 2nd to 5th orders for 25 eyes across the horizontal (nasal - temporal retina) and vertical (inferior - superior retina) visual field. Pupil size 6 mm. Zernike defocus aberration has been corrected on-axis. For the sake of clarity, error bars have been omitted.

include defocus $c(2,0)$, and three other aberration groups with paired components such as astigmatism $((c(2,2))^2 + (c(2,-2))^2)^{1/2}$, coma $((c(3,1))^2 + (c(3,-1))^2)^{1/2}$ and trefoil coma $((c(3,3))^2 + (c(3,-3))^2)^{1/2}$. For completeness we also present a spherical aberration coefficient $c(4,0)$ as its value is significantly distinguished within other 4th order aberrations terms.

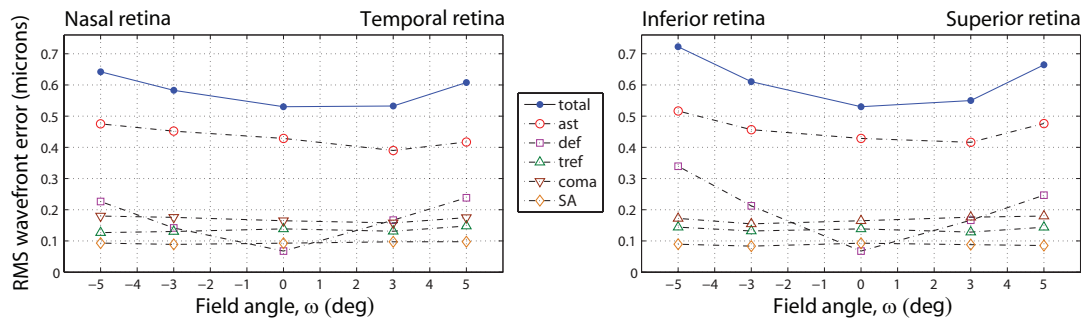


Figure 3.12: *RMS* wavefront error estimated as an average value of 25 eyes for major aberration groups across the horizontal (nasal - temporal retina) and vertical (inferior - superior retina) visual field. Pupil size 6 mm. Chosen abbreviation: **total** - total *RMS* wavefront error, **def** - Zernike defocus coefficient $c(2,0)$, **SA** - Zernike spherical aberration coefficient $c(4,0)$. Note, that Zernike defocus aberration has been corrected on-axis. For the sake of clarity, error bars have been omitted.

As a first step we shall look at the averaged *RMS* values of these aberrations estimated for 25 eyes for each field point. This type of averaging deals with absolute values of Zernike coefficients. Using absolute values reveals the main contributors to the total wavefront error shown as blue curves in Fig. 3.12. It can be seen that the astigmatism is a dominant aberration across the central visual field and it defines the shape of

the total *RMS* curves. Defocus term also influences the shape of the total *RMS* curve but to a smaller extent compared to astigmatism. Nevertheless the defocus term was minimized on axis and therefore its contribution is reduced, yet it still remains to be the second largest aberration at 5 *degree*. In optical systems working off-axis, this aberration corresponds to field curvature. In the eye, the variation of the defocus term across the visual field is primarily dictated by the shape of the retinal surface.

Due to the large inter-subject differences, the total *RMS* wavefront error on-axis varied among the subjects, with a standard deviation (*SD*) of $0.23 \mu\text{m}$. The typical value of the total *RMS* error off-axis showed similar level of inter-subject variability. In light of this, averaging aberrations at each field point independently does not provide any substantial insight into relative changes in aberrations occurring between field points.

At this stage in our analysis we shall consider a different way of presenting the average wavefront across the visual field. For each eye we subtract the wavefront measured on axis (using it as a reference value) from the other wavefront obtained off axis prior to estimating the average of 25 eyes. This should allow us to see the field dependence of aberrations more clearly or in other words, their field differences in amplitude in respect to the line of sight. Figure 3.13 presents this method of obtaining new, residual wavefronts and corresponding *RMS*.

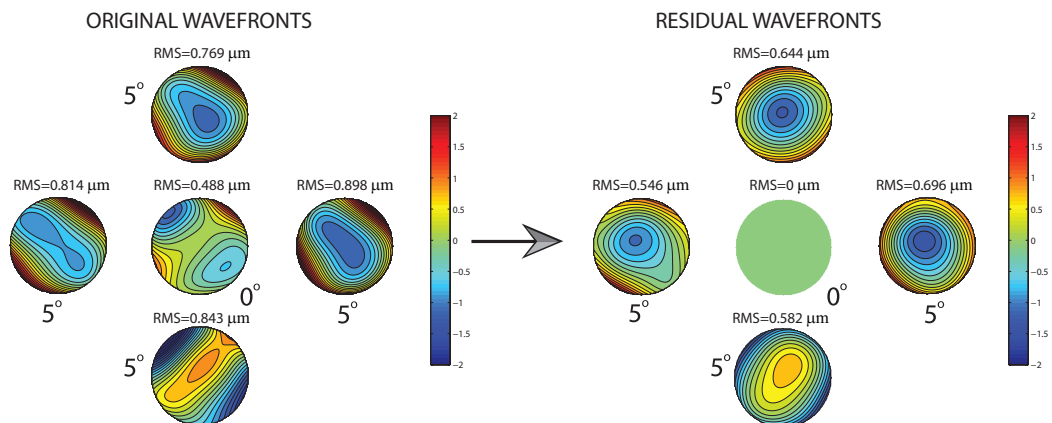


Figure 3.13: Subject no. 14. Residuals wavefronts obtained from original wavefronts, measured across horizontal and vertical meridian of the central visual field. For clarity, phase-maps for 3 *degree* are not presented.

Our plots presented in Fig. 3.14 clearly show the field dependence of aberrations and their contribution to the off-axis total *RMS* wavefront error. Similarly to the previous case, the second-order (defocus and astigmatism) are the major contributors here. The *RMS* value for astigmatism estimated as a combination of two coef-

ficients $((c(2,2))^2 + (c(2,-2))^2)^{1/2}$ (total astigmatism) increases significantly when going from the center to the field periphery. Comparing distribution of the total RMS wavefront error in both meridians, one can see that it has a slightly bigger value in the inferior region of the retina. It is because the defocus term and total astigmatism play slightly bigger role in this area of visual field of view. However in the horizontal meridian they demonstrate almost symmetric distribution around line of sight axis. This still may be a consequence of averaging, which leads to compensate of differently distributed values of the RMS across the field of view.

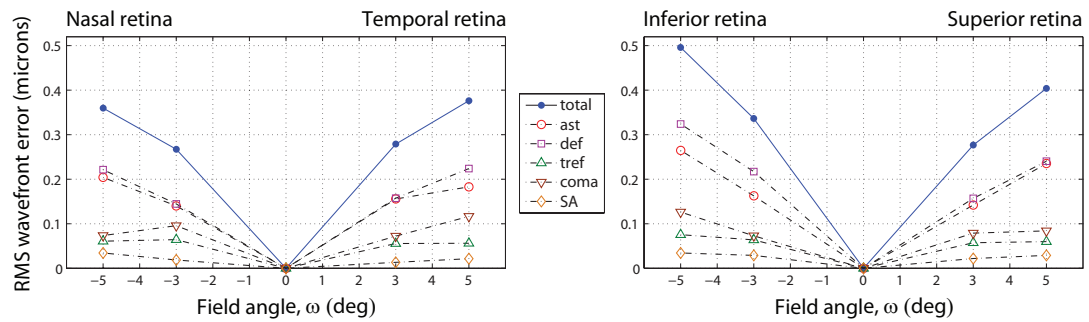


Figure 3.14: Distribution of the average RMS wavefront error in the horizontal and vertical meridian estimated with respect to the central field point. For each subject on-axis phase map was used as a reference and subtracted from other field points prior to averaging. For the sake of clarity, error bars have been omitted.

Subject Dependent Types of Field Distribution of Ocular Aberrations

As it has been already mentioned and reported before, because of high inter-subject variability in amplitude and/or sign for some of Zernike aberration coefficients, it might be difficult to create a reasonable conclusion based on mean values of the RMS. In order to distinguish different patterns of aberration distribution we shall look more closely for each subject separately.

From Figs. 3.11 and 3.12 one can clearly see, that the mean value of Zernike defocus and astigmatism are much greater, compared to other terms, and hence the coefficients from 2nd order have the strongest impact for a total RMS distribution. From our observation on different field distributions of lower-order terms, we are able to distinguish three types of different total RMS variation across the visual field. Figure 3.15 presents three different "types" of the RMS field distribution across the horizontal meridian. Those are "flat" or "non-varying" variation, "quadratic" variation, and "non-symmetric" or "odd" variation. Each group consists of three typical representa-

tive eyes for a particular aberration distribution. Each plot, apart from showing the curve for the total *RMS* wavefront error, presents also the horizontal distribution of Zernike defocus coefficient $c(2,0)$, total astigmatism $((c(2,2))^2 + (c(2,-2))^2)^{1/2}$, and total amount of coma-like coefficients from the 3rd order $((c(3,1))^2 + (c(3,-1))^2) + (c(3,3))^2 + (c(3,-3))^2)^{1/2}$ across the central visual field. Aberration coefficients for other Zernike orders has not been included in the plot due to their negligible impact to the total ocular aberrations (note, that spherical aberration coefficient $c(4,0)$ has a distinct weight within 4th order terms, however we have already showed its constant distribution for the field for each measured eye).

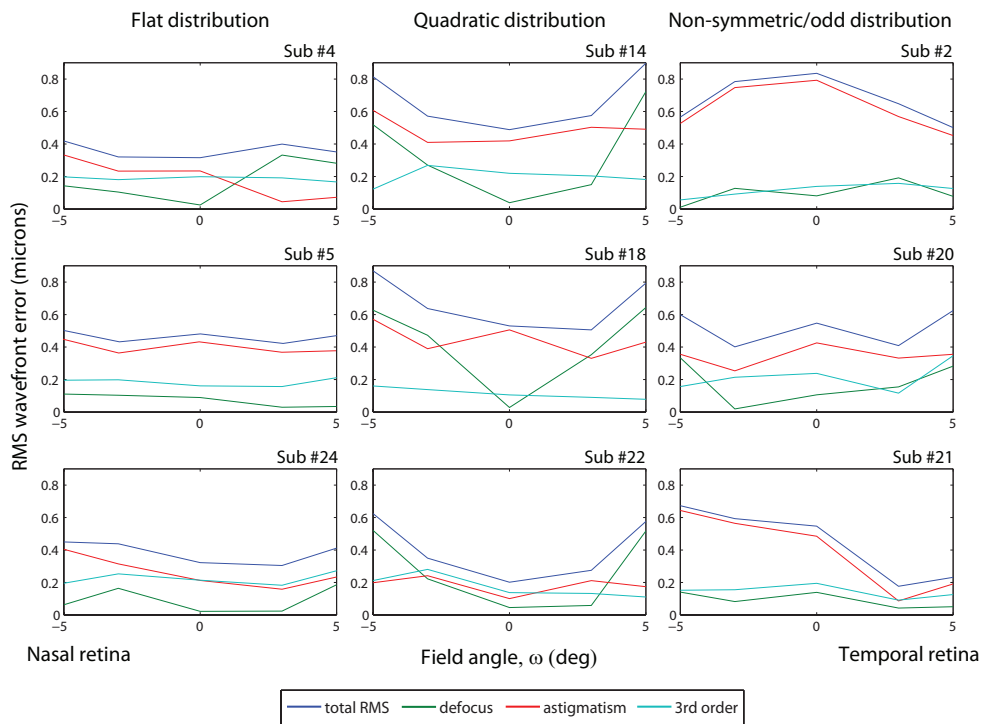


Figure 3.15: **Horizontal** field of view. Measured *RMS* wavefront error as a function of the field angle. Nine eyes represent three types of the total *RMS* variation across the horizontal visual field, such as "*flat*", "*quadratic*", and "*non-symmetric*" or "*odd*". For the sake of clarity, error bars have been omitted.

It can be clearly seen that for eyes with "*quadratic*" distribution (subjects no. 14, no. 18 and no. 22) the main component, which shapes the *RMS* curve (blue line in Fig. 3.15) in the periphery is defocus aberration $c(2,0)$ (green line in Fig. 3.15). This may be due to the strong presence of field curvature, which, at this stage, is the component of the total defocus amounts across the field. Note, that besides strong influence from the $c(2,0)$ term for the total *RMS* and its quadratic distribution, it is not possible to unam-

biguously determine the distribution of total astigmatism. It appears differently for 3 representative eyes for the quadratic distribution group, dropping twice for a minimum value at -3 and $+3$ *degree* of the field angle (subject no. 18), taking a minimum on-axis (subject no. 22) and finally being non-regular across the horizontal visual field (subject no. 14). For the remaining cases, the defocus term does not appear in a such regular pattern.

The "*flat*" (or non-varying) category (subjects no. 4, no. 5 and no. 24) is characterized by non-varying (or less varying) distribution of the wavefront error for all measured Zernike orders. The defocus term seems not to be a dominant factor since there is significant influence from total astigmatism (red line in Fig. 3.15) on the final shape of the total *RMS*. It would be worth noting here, that for our "*flat*" distribution group, the amplitude of measured aberrations is not the case here. In other words, the amplitude of the total wavefront error has no effect here, since the total *RMS* may be relatively large (oscillating around $0.7 \mu\text{m}$ across the field for subject no. 11, to around $1 \mu\text{m}$ for subject no. 13), but still not exhibits much variation across the field.

The third group of "*non-symmetric*" or "*odd*" distribution (subject no. 2, no. 20 and no. 21) is slightly more difficult to describe. Surprisingly the minimum for the total wavefront error is not necessarily located on-axis, which for all plots correspond to the line of sight. For two subject from the third type (no. 2 and no. 21) the total astigmatism is obvious dominant factor but it reaches its minimum not at the center, but somewhere in the periphery ($+3$ *degree* at the temporal retina for subject no. 21, and -5 *degree* nasally and $+5$ *degree* temporally for subject no. 2). It may indicate a large influence of the corneal astigmatism that may come from the corneal toricity. However both subjects no. 2 and no. 21 indicate a lack of symmetry in the combined astigmatism, subject no. 20 shows some symmetry in the total astigmatism distribution, but again, it exhibits non-symmetrical distribution for other presented *RMS* curves of the defocus term and 3^{rd} order aberration terms. It is in fact very interesting case, when the value of the *RMS* of total astigmatism dropped down twice for -3 *degree* nasal retina and $+3$ *degree* temporal retina, whereas the minima for defocus and 3^{rd} order aberration fall on both sides of the reference axis at -3 *degree* and $+3$ *degree* respectively. It may indicate that at some points along the field, there is possible correction of the field-dependent astigmatism (classical case of astigmatism aberration) and corneal astigmatism. A common field "*behavior*" for three presented representative groups is the distribution of 3^{rd} order aberration terms. Their value of the total *RMS* not varying much across the field, oscillates around $0.2 \mu\text{m}$.

In order to analyse these *RMS*s distribution types along a horizontal meridian, as

before, we subtract on-axis wavefront from off-axis field points for each subject in our representative set. Figure 3.16 presents results as residual *RMS* values for, total, defocus, total astigmatism and 3rd order terms as a function of horizontal field angle ω .

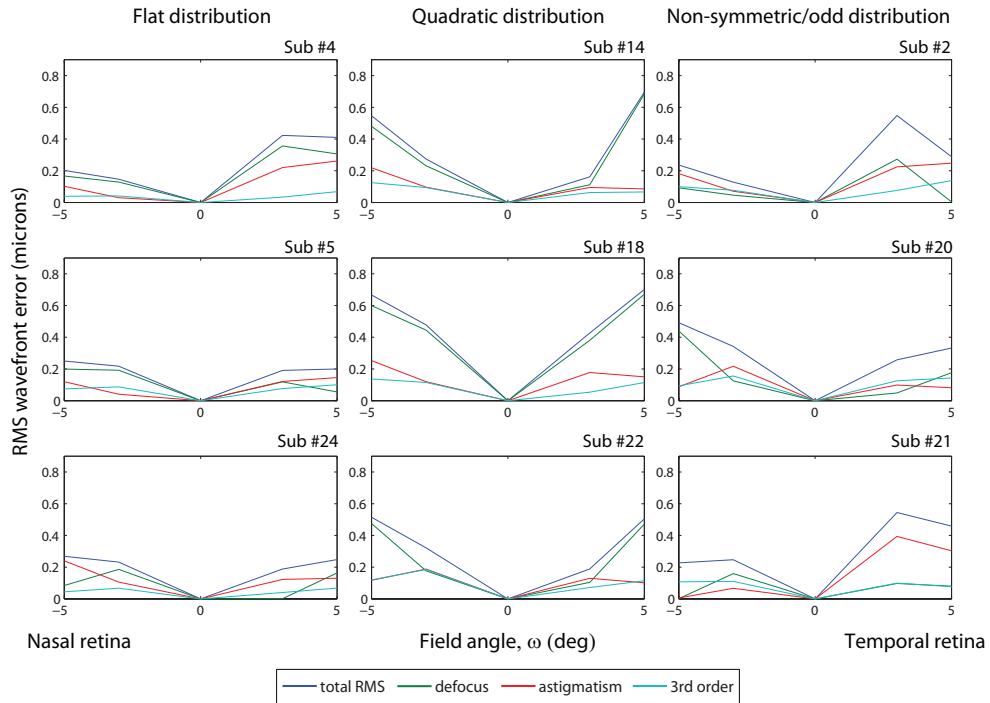


Figure 3.16: **Horizontal** field of view. The residual *RMS* wavefront error as a function of the field angle for the three observed groups. The residual *RMS* values are the results of the subtracting the center wavefront from each field point. For the sake of clarity, error bars have been omitted.

After the on-axis reference subtraction and averaging, we can still distinguish our three groups and it illustrates, that for different field distribution we might observe different residual patterns of ocular aberrations (or on-axis correction). The "flat" distribution group indicates noticeable or regular pattern of correction (or in other words the residual wavefronts are likely to be lowered, in terms of the total *RMS*, when subtracting the on-axis (reference) wavefront). Besides the peripheral-temporal side of the retina for a subject no. 4 (+3 to +5 degree), all remaining field points for other eyes are significantly reduced at periphery of our visual field (from about 1.5 μm to 0.25 μm). Zernike terms from the 3rd order for this group are reduced to the level being below 0.1 μm so they will not produce any noticeable image degradation on the retina. The "quadratic" distribution group displays a tendency to hold the shape

of the total wavefront error distribution curve. Here one can see the influence of field curvature (*FC*). The *FC* keeps its amplitude across the field and mimics the total *RMS* curve. The total residual astigmatism is lowered in its amplitude and hence the total wavefront error is reduced from $0.2 \mu\text{m}$ to $0.1 \mu\text{m}$ at the field periphery. The third group of eyes with "*non-symmetric*" distribution shows more variation or irregularities after subtraction. Due to lack of symmetry along the line of sight, residual wavefronts may stay unchanged in terms of the amplitude of the total residual *RMS* (as can be seen *+3 degree* temporal field for subject no. 2), or even gains an additional amount of aberration (see *+3 degree* temporal field for subject no. 21). Here, similar to the "*flat*" category of eyes, field curvature and field dependent astigmatism are inter-mixed along the meridian shaping the final curve of the total residual *RMS* wavefront error. It is worth noting, that the 3^{rd} order terms vary more with the field in this group of eyes.

Similar to the horizontal meridian we shall describe a vertical field of view using the same representative eyes as previously. Figure 3.17 presents 9 plots of the total *RMS* wavefront error (in microns) as a function of a vertical field of view. One can see, that the vertical meridian is more likely to promote a quadratic distribution of the total wavefront error. Comparing to the previous situation from Fig. 3.15, it is easy to see, that some eyes "*jump*" to another distribution category, which again may prove the non-symmetrical nature of the optical system of the human eye. Some subjects (no. 14, no. 18, and no. 22), appear again in a quadratic manner distribution enlarged by two other eyes (subject no. 4, and no. 24), that came from the "*flat*" distribution group in a horizontal meridian. Two eyes (subject no. 2, and no. 20), being previously in "*odd*" category have been moved to a "*flat*" or non-varying group of the total *RMS* distribution. And again in general, the total astigmatism seems to play a main role in shaping the total *RMS* curve, even in some cases of quadratic-distribution examples.

Subtracting central wavefront from other off-axis field points (in the vertical meridian), gives residual aberration distribution plotted on Fig. 3.18. And similar to the horizontal field case, the field curvature is dominant aberration for residual wavefronts of "*quadratic*" group. (except for subject no. 24, who shows more contribution from the total astigmatism *RMS*). Subjects no. 2, and no. 20, however located in the non-varying group of the total *RMS* in the vertical meridian, exhibit some odd variation (but still symmetrical) of the *FC*. This results in a dominant or strong role of the *FC* in residual wavefronts of these two subjects, while the amount of the total astigmatism (just because its non-varying behavior across the field, see Fig. 3.17) is, in general, lowered after subtraction. Terms from the 3^{rd} order aberration show very

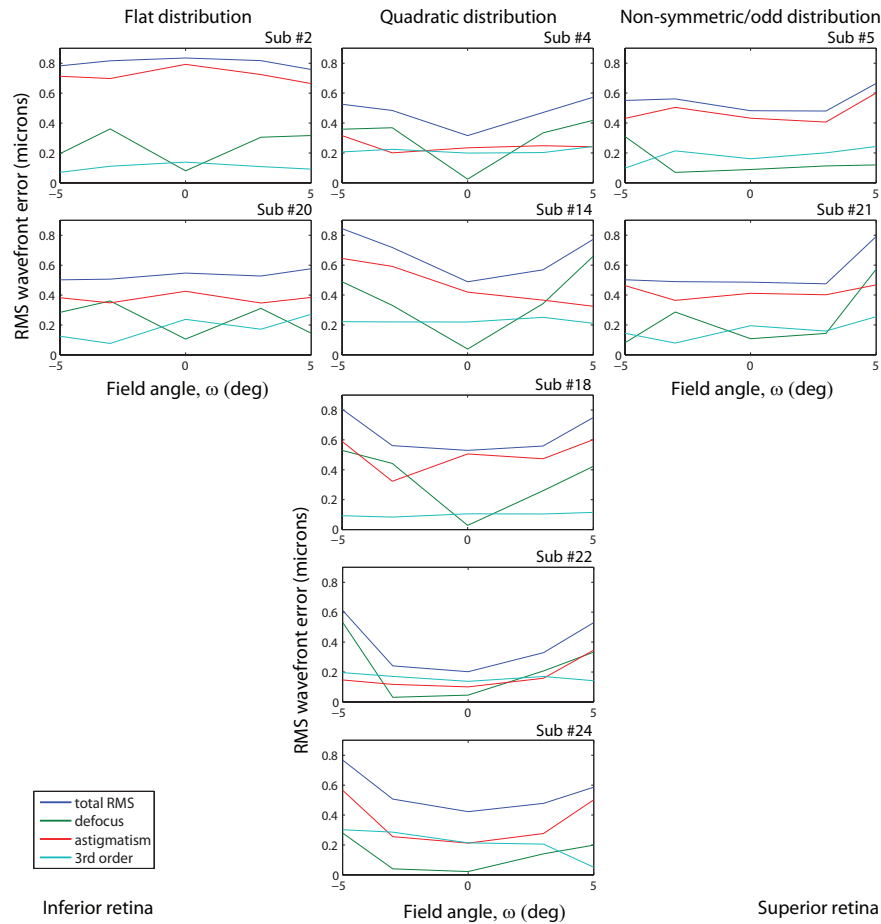


Figure 3.17: **Vertical** field of view. Measured *RMS* wavefront error as a function of the field angle. Nine eyes (from Fig. 3.15) represent three types of the total *RMS* variation across the vertical visual field. For the sake of clarity, error bars have been omitted.

low magnitude in general, being below or oscillating around $0.1 \mu m$ in *RMS*. This level may vary between subjects and for some cases raise its amplitude to the value of $0.2 \mu m$ or even slightly more (subject no. 2, no. 20, no. 21, and no. 24). We shall emphasize again the change of the field aberration pattern distribution for some subjects, when changing the meridian, which indicates the lack of rotational symmetry and hence general complexity of the optical system of the human eye.

As a summary of aberration distribution along a horizontal and vertical meridian we shall group all remaining eyes from our population study in previously distinguished types. Figure 3.19 depicts a mean wavefront errors obtained after averaged a number of eyes qualified to each group with different distribution of the total *RMS*. It shows mean variation of the wavefront error for the field curvature, and for grouped Zernike

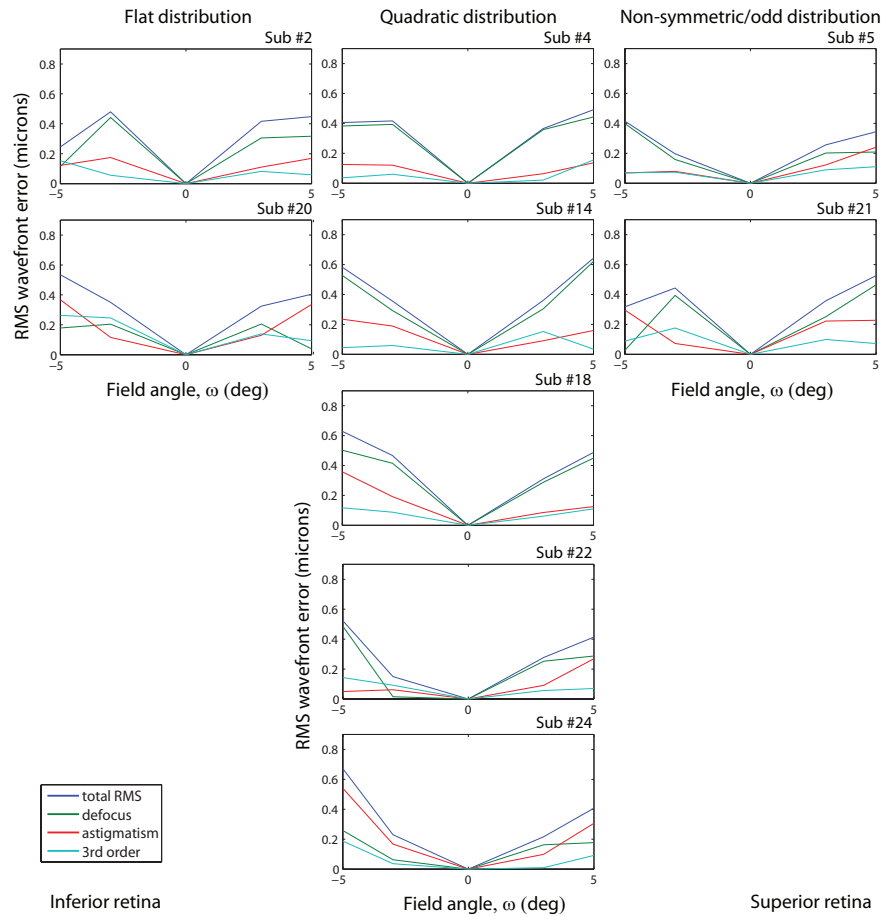


Figure 3.18: **Vertical** field of view. The residual *RMS* wavefront error as a function of the field angle for the three observed groups. The residual *RMS* values are the results of the subtracting the center wavefront from each field point. For the sake of clarity, error bars have been omitted.

aberration terms such as: total astigmatism and total *RMS* of the 3rd order Zernike terms.

For statistical matter it is worth to note here, that within our 25 young eyes, and for **horizontal** meridian: 5 we qualified as flat *RMS* variation across the field, next, 10 with strong influence from the field curvature as quadratic distribution of the *RMS* curve, and finally 10 remaining, indicating lack of symmetry along reference axis or odd (unlike) variation across the horizontal meridian. As we have already mentioned, **vertical** meridian is more "*symmetric*", which means more eyes have been recognized with a quadratic distribution of the total *RMS*. And consequently as in the horizontal meridian, "*flat*" or non-varying group contains 6 eyes, 15 eyes form a "*quadratic*"

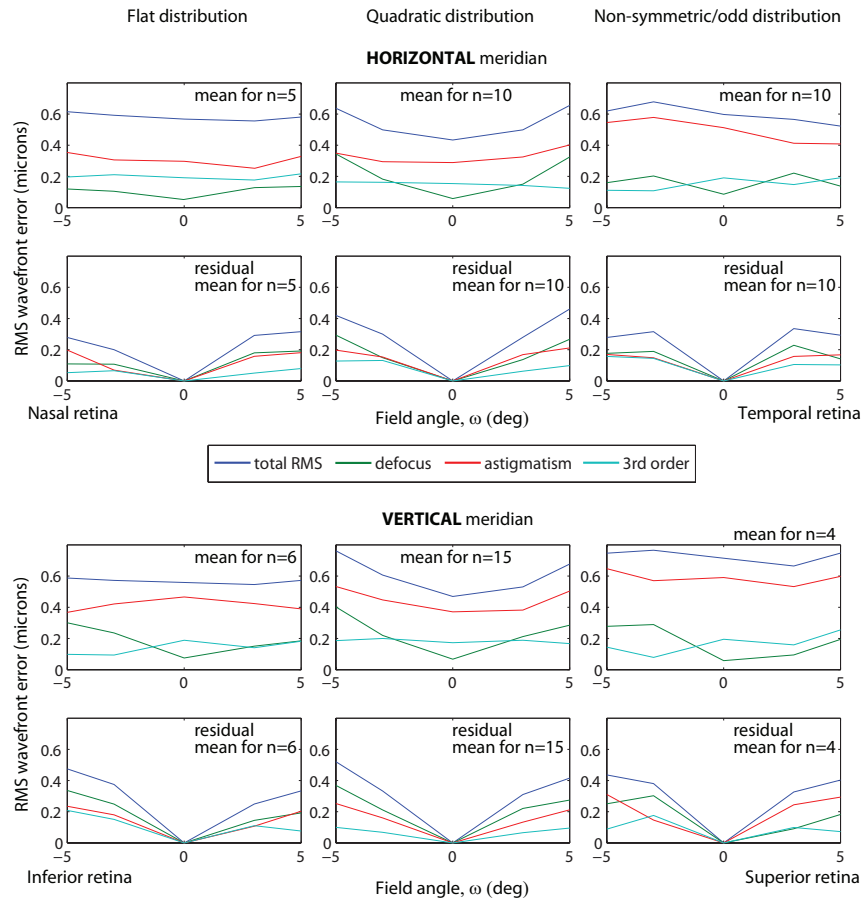


Figure 3.19: **Horizontal** and **vertical** meridians. Group mean *RMS* wavefront error for all eyes in the study divided into the three observed groups. The n is a number of eyes indicate a field distribution for particular group. For the sake of clarity, error bars have been omitted.

distribution group, and only 4 eyes we could qualify to the "odd" or non-symmetric group.

The nature of field curvature is such, that it varies as a quadratic function of field position. In some eyes there is clear tendency for such a behavior (even if we forced the field curvature aberration to reaches its minimum in the center of our visual field by Badal adjustment). Some other eyes indicate rather non-varying or non-symmetric distribution of field curvature, but here we shall keep in mind, that we only study the central visual field (but still very important for retinal-imaging techniques). A small region on the retina could be not enough for complete describing the aberration field pattern for some cases (especially those with less-varying distribution). After subtraction (or correction on-axis), the field curvature aberration usually tran-

spires its weight, which is very often crucial for a total amount of wavefront error. Although we were able to catch some patterns or symmetries, just because we analyse the "*whole*" eye ocular wavefronts we can not clearly distinguish aberrations that come from cornea. This could be done in the future as the knowledge about possible mutual corrections between the cornea and the inner optics of the eye still needs to be validated.

3.4 Estimation of the Isoplanatic Patch

In this section we aim to roughly estimate an isoplanatic area for the young human eye, based on our experimental data. In astronomy, this area is usually defined as a region of the field where the variation of the root mean- square (*RMS*) wavefront error between any two points does not exceed 1 *rad* [152]. Following this definition, and as we discussed in our previous publication [60], in our case this is equivalent to $\lambda/2\pi = 0.108 \mu m$. Therefore, we shall consider the isoplanatic patch as an area in the visual field, where the *RMS* wavefront error does not exceed 0.11 μm with respect to the central value of the patch (this is equivalent to Strehl ratio being reduced to $1/e = 0.37$). This boundary value of the *RMS* is more realistically achievable criterion over a 6 mm *pupil*, compared to the Maréchal criterion, which locates value of the *RMS* wavefront error below the value of $\lambda/14$ for diffraction limited systems. We shall use this definition of the isoplanatic patch. Rotationally symmetric optical systems exhibit symmetric distribution of field aberrations that can be characterized in annular zones of the field [52], whereas for the optical systems, that lack any type of symmetry, *e.g.* the human eye, the characterization of image quality involves larger number of field points. Knowing the isoplanatic patch could help to find the optimal number of reference points required for modeling the imaging properties of the system. In the case of system reconstruction, one should position the probing sources within the angular distance comparable with the size of the isoplanatic patch.

We are aware, that for non-symmetrical optical systems such a human eye, the shape of the isoplanatic patch may be irregular (instead of being circular like in symmetrical systems), and hence the number of meridians and sampling points, that examine the field of view should be much greater. However, we measured the 10 by 10 *degree* visual field only in two meridians, and with 3 and 2 *degree* of increments, we shall be able to give an estimate size of the isoplanatic regions for our 25 young subjects. We estimated the sizes of the isoplanatic regions for each eye using residual wavefronts, which are a results of subtracting of the foveal (reference) wavefront from wavefronts

measured at all eccentricities. This method can be found in previous studies [153–156]. Subtracting the reference, on-axis wavefront can be regarded here as a result of perfect adaptive optics (AO) correction, when the corrector is conjugated to the pupil. Table 3.3 below, shows the patch diameters (given in field angle ω degree) for the total RMS, field-dependent astigmatism (RMS of sum of two Zernike astigmatism coefficients $c(2,-2)$ and $c(2,2)$) and field curvature (focus error off-axis). It contains the results for each group of eyes we discussed in the previous section, along two meridians. It also presents the mean isoplanatic patch size calculated for all subjects investigated in our young population study.

Table 3.3: Assessment of the isoplanatic patch, ± 1 SD.

Distribution group	HORIZONTAL FIELD OF VIEW			VERTICAL FIELD OF VIEW		
	total RMS (deg)	Ast (deg)	Defocus (deg)	total RMS (deg)	Ast (deg)	Defocus (deg)
Quadratic	2.30±0.73	4.54±1.39	5.53±2.62	2.16±0.79	5.14±1.63	4.23±2.64
Flat	2.75±0.19	6.05±0.81	4.98±1.40	2.50±1.10	5.56±2.55	4.08±1.95
Odd	2.55±1.29	5.17±1.53	4.76±2.61	1.75±0.29	3.36±0.90	4.95±2.44
ALL	2.47±0.93	5.01±1.42	5.16±2.36	2.13±0.81	4.90±1.81	4.31±2.39

Our results are comparable with previous findings, estimated for 6 mm pupil size and used of foveal wavefront subtracting method. Maida *et.al*, found the patch diameter laying between 1 and 2 degree, however they measured only two subjects, which is rather poor indication for a good statistics [153]. Tarant and Roorda [156], performing the Maréchal criterion for a 5 subjects, gave the patch dimension being between 1.80 and 2.64 degree in diameter [138]. Dubinin *et.al*, calculating the mean square wavefront error being less than 1 rad^2 as a isoplanatism criterion, over a 4 mm pupil for 4 subjects, evaluated the isoplanatic region as 1.5 to 2.5 degree. From the table above, it can be clearly seen, that the individual aberrations groups have larger isoplanatic patch, it is for example around 5 degree for defocus (field curvature) and field-dependent astigmatism. This wide isoplanatic region dimension for astigmatism and field curvature is rather surprise, however we shall still keep in mind, that, we investigated young eyes with moderate amount of refractive errors and with Badal correction set prior to measurement. Another reason for such a large patch diameters (for field-dependent astigmatism and field curvature) comes from a fact, that we took a criterion larger

than a classical Maréchal, which in our case would give the *RMS* to be less than $0.048 \mu m$, for the wavelength of $\lambda = 0.677 \mu m$. It is also relatively easy to see the differences between each of the groups of different *RMS* distribution along the field. As we assumed in the previous section, eyes within the non-varying (flat) distribution group are characterized by a larger area of insignificant *RMS* variation with respect to the central value. Even though we estimated the isoplanatic region only for four directions in the field (two meridians), it again proves a highly asymmetric nature of the human eye optical system.

Chapter 4

Assessment of the Tear Film Contribution to the Total Ocular Aberration

Ocular aberrations have recently been studied using improved aberrometers based on the Shack-Hartmann wavefront sensor that provides much higher accuracy than other techniques. The purpose of this study was to measure the changes of ocular aberrations on the visual axis after a single blink, which is directly related to tear film variation. The accommodation of the eye was paralyzed by 1 *percent* drop of Tropicamide to avoid changes in ocular aberrations due to crystalline lens refocusing. The optical effect of the tear film on vision is of great interest for eye modeling, corneal topography and eye aberrometry in general. The data was collected for 5 young eyes without any corneal abnormalities. Numerical analysis of each single Zernike coefficient (up to 5th order) was performed to study the variations of its amplitude after blinking.

4.1 Literature Review

The tear film is the most anterior optical surface. Since it gives a large refractive index step from air to the tears (from 1 to around 1.333 [157] or even 1.337 [21]) it is of a great importance for performance of the optical system of the human eye. Figure 4.1 is a graphical visualization of the variation of the refractive index along the optical axis coordinate in the rotationally symmetric model of the human cornea and tear film proposed by Barbero [158].

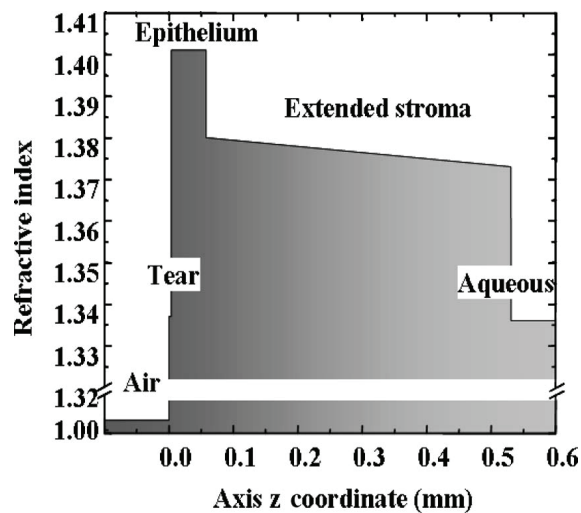


Figure 4.1: Refractive index along the optical axis coordinate (in millimeters) in the cornea model. The y axis of the graphic is broken from 1.02 to 1.32 for better visualization. The illustration adopted from [158].

The tear film is a three layer structure composed of mucus, aqueous (main component) and lipid as the most external layer as presented in Figure 4.2 based on [157]. Their role is to provide a smooth optical layer on the rough and irregular surface of the cornea. Thickness of the tear film is typically $3 - 8 \mu\text{m}$ [22]. These three layers may vary due to different factors such as:

- (a) normal physiology: diurnal fluctuations, menstruation, potentially diet;
- (b) environment : air-conditioning, air-pollution, contact lens wear;
- (c) pathological conditions: dry eye, medications, post refractive surgery condition.

The above factors increase the irregularity of the tear film; and even for healthy eye the tear film layer is not stable between consecutive blinks. This lack of stability of

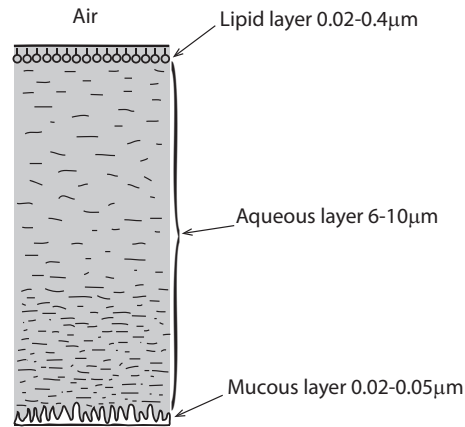


Figure 4.2: Schema of the three layers, which form the pre-corneal tear film. Lipid layer - coats the aqueous layer by providing a hydrophobic barrier. It retards evaporation and prevents tears spilling out. Aqueous layer - mainly built with water. It helps in spreading of the tear film and promotes the control of infectious agents and osmotic regulation. Mucous layer - built with mucin. It coats the corneal epithelium layer providing a hydrophilic layer. It also helps in even distribution of the tear film.

the tear film layer, appears as local changes in thickness or disruptions, that introduce aberrations into the optical system of the eye. Furthermore, complete break-up in the tear film exposes the rough corneal epithelial surface and may increase optical scatter. It is not difficult to predict the degrading role of these effects for retinal image quality and it has been already reported [22, 93, 95–98, 159–161].

However the nature of the tear film entails some difficulties in exact understanding of its influence for entire optics of the eye, it is possible to observe its usual behavior after it is redistributed by the eyelids. After single blink a tear film require some time to provide a smooth and continuous layer over the cornea. This process is widely known as "*build-up*" and was first observed by the János Németh *et al.* [160]. Using a high-speed videotopographic measurement technique, they found the tear film build-up time to be approximately 3 to 10 *seconds*, which is in fact a wide range. After this time, the tear film layer undergoes a degradation process clinically called tear film "*break-up*" [162, 163]. The break-up in tear film surface is schematically presented in Fig. 4.3.

Many researchers have been studying the nature of the tear film, its topography and influence on the optical properties of the eye. Li and Yoon, using the Shack-Hartmann (*SH*) wavefront sensor (that is more suitable to tear film detection than corneal topographers), observed variations in wavefront caused by increasing irregularities in the

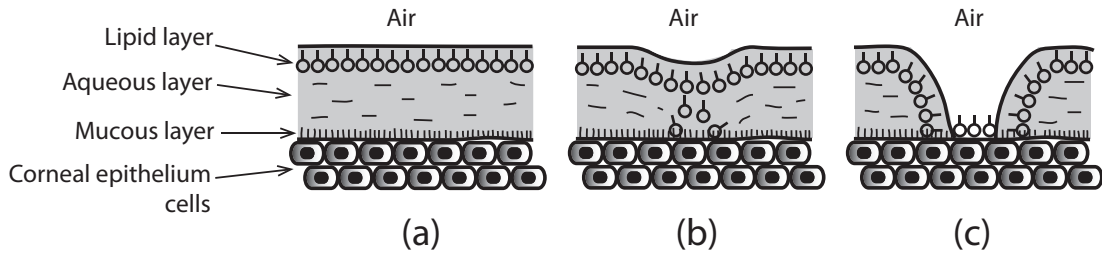


Figure 4.3: Schematic illustration of tear film evolution on the corneal surface: (a)- tear film stability phase is characterized by the uniform distribution of tear, (b)-thinning of the tear film, diffusion of lipids to the mucous layer (c) - tear film break up, pre-corneal surface is not coated any more. Rough cornea and scatter can effectively degrade the image quality on the retina.

tear film [97]. An earlier study by Thibos *et.al* demonstrated that the *SH* wavefront sensing technique is sensitive enough to examine the optical changes induced by the pre-corneal tear film fluctuations [115]. Measurements have also been made using lateral shearing interferometry [22, 95]. Dubra *et.al* concluded, after his study of 21 subjects, that the tear topography may significantly degrade the image resolution in the scale of seconds after perfect static aberration correction with deformable mirror [95]. Very recent study by Szczesna and Iskander, demonstrated a high quality of interferometric measurement of the tear film and uncovered even more phases of its distribution over the cornea [96]. According to their work, it is possible to characterize up to five different phases of tear film surface kinetics: (1) initial fast tear film build-up phase, (2) further slower tear film build-up phase, (3) tear film stability, (4) tear film thinning, and (5) tear film disruption (after a detected break-up). Work of Gruppetta *et.al*, where they used a curvature sensing setup, confirmed variation in optical quality due to the tear film [98]. Our aim, which joins all the studies mentioned, was to measure the changes of ocular aberrations on the visual axis after consecutive blinking, which is directly related to variations in the tear film distribution on the cornea. The optical effect of the tear film on vision is of great interest for eye modeling, corneal topography and eye aberrometry in general.

4.2 Experimental Procedure

The data was collected for 5 young subjects with healthy eyes measured and recorded at 12 Hz. Their age was between 26 and 29 years and had a mean value of 27.5 years. Spherical refraction was in the range from 0 D to 1 D and up to 0.75 D in cylinder.

One drop of Tropicamide 1 percent was applied to the eye in order to dilate the pupil and paralyze accommodation. For each series of measurements after a blink, the eye was aligned with the optical axis of the aberrometer, the Badal stage was adjusted for the best sphere and the pupil tracking system was following horizontal and vertical movements of the eye (see Fig. 4.4, (A,B) case for reference). This arrangement ensured that the aberrated wavefront was always measured with respect to the center of the pupil. Each measurement was performed immediately after the blink, and consisted of 20 frames within 12 seconds of non-blink interval, which gave approximately 0.6 seconds intervals between consecutive frames. This was sufficient to estimate the standard deviation (*SD*) after a single blink. A series of 10 measurements (trials) taken after 10 blinks provides an estimation of the *SD* for multiple blinks. Single frames (wavefronts), with a blink appearance before the time of 12 seconds were excluded from our analysis set. Each subject had an opportunity to practice its ability to hold stable fixation at the central point on the fixation target. The diameter of the measured pupil was 6 mm. Figure 4.4 presents two single frames (A,B) of the subject EUG captured 2.35 seconds and 11.57 seconds after the blink respectively. It is clearly seen, that after a certain time interval the tear film breaks-up, the surface is disrupted and hence the quality of *SH* spots is degraded.

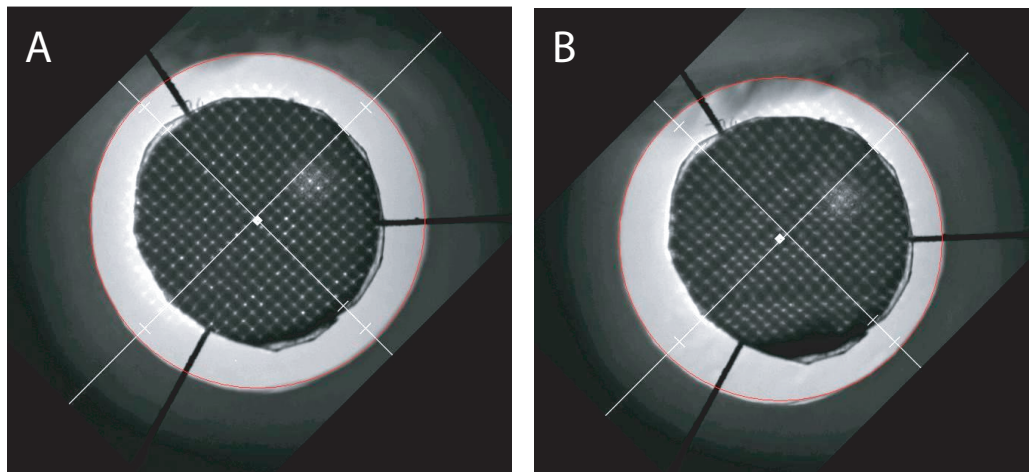


Figure 4.4: Image **A** presents a Shack-Hartman (*SH*) spots pattern for subject *EG* after about 2 second from a single blink. Image **B** shows a *SH* pattern degradation after about 12 second from a single blink. Note, that pupil tracker recorded about 0.22 mm pupil horizontal drift, which is less than 4 percent of the pupil diameter (note, that the *CCD* is rotated at 45 degree to the horizontal meridian of the eye in order to achieve a better sampling and larger dynamic range for astigmatism [142]).

The nature of the experiment is such, that besides the optical effect of tear film variation, it also takes into account several different factors. These are mainly various eye movements, that may cause unwanted misalignment during data collecting process. Eye movements have the potential to affect the reliability of data. The eye movements can significantly degrade the quality of measurement and they are usually categorized according to their temporal characteristics:

- **Ocular tremor** (sometimes called physiological nystagmus). Tremor, however aperiodic, is a wave-like motion of the eyes. It oscillates with a frequency range from 90 Hz to 150 Hz and has a low amplitude of 0.025 μm to 2.5 μm . Although the ocular tremor movement is measurable its contribution to the maintenance of vision is rather not clear.
- **Ocular drifts**. These are slow motions of the eye, during which the object of fixation can move across a dozen number of photoreceptors (about 1 *arcmin* per 0.2-1 *second*). The drift movements, generated by the oculomotor system, play an important compensatory role in maintaining accurate visual fixation in the absence or poor performance of microsaccades (see next).
- **Microsaccades** (also called "*flicks*" in early studies). They are small (about 25 *ms* duration, can move retinal image across 5 *arcmin*) jerk-like movements occurring during voluntary fixation. However, their possible role is to correct displacements in eye position produced by drifts, the accuracy of potentially correction from microsaccades is limited [164].

In order to ensure, that our experimental data does not show significant influence from other factors (like the eye or/and head movements), two post-processing steps has been made to prevent inaccurate data points that affect the tear film measurements. Firstly, the number of trials ($n = 10$) with no obvious movements of the center of the pupil or another undesirable factors (sudden blink) judged by the examiner at the measurement process, were chosen for further analysis (note that total number of experimental trials for each subjects to around 20). Secondly, for each of 20 wavefronts within a single trial, a pupil centre displacement distance d was found calculated as:

$$d = \sqrt{(x^2) + (y^2)}, \quad (4.1)$$

where x and y are coordinations determining position of pupil centre relative to a centre of CCD in the horizontal (x) and vertical (y) meridians in the entrance pupil plane

of the human eye. Knowing the distance of displacement of the pupil centre and the total *RMS* wavefront error for each of 20 frames along the 12 *seconds* trial, calculation of a correlation coefficient (r) (Pearson's coefficient) was performed. The correlation coefficient is a quantitative measure of mutual relationship when comparing sets of data. In other words, it tells us whether any relationship exists between pupil displacement and the total *RMS* and how strong it is. The r coefficient does not depend on the units or the choice of variables, and always lies in the range (1,1). Following Bland [149], we can express r for any pair of observations, denoted by (x_i, y_i) :

$$r = \frac{\sqrt{\sum(x_i - \bar{x})(y_i - \bar{y})}}{\sqrt{(\sum(x_i - \bar{x})^2) + (\sum(y_i - \bar{y})^2)}}. \quad (4.2)$$

A square of r is known as coefficient of determination. For two linearly related variables, r^2 provides the proportion of variation in one variable, that can be explained by the variation in the other variable. For instance, if $r^2 = 0.25$ or 25 *percent* it means that approximately 25 *percent* of the variation in the variable y can be explained by the variation in the variable x . It is basic statistical tool, yet it is sufficient for the first step for eliminating most of inaccurate measurements.

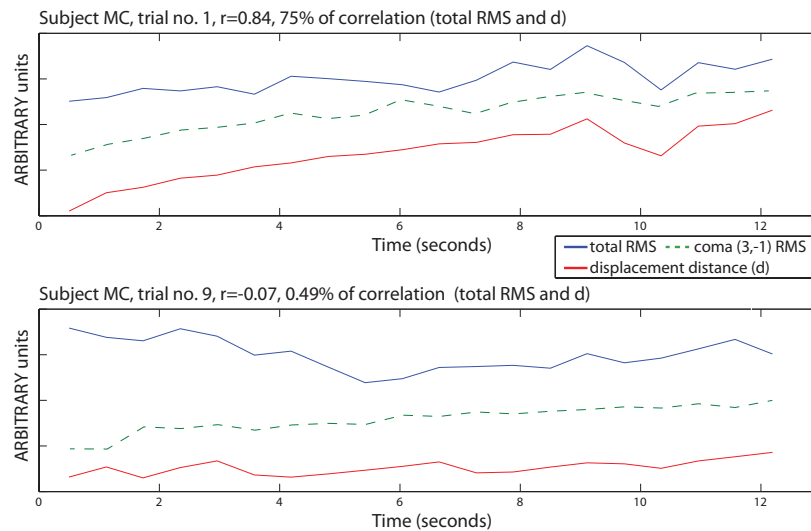


Figure 4.5: An example of the correlation assessment between distribution of the total *RMS* (blue line) and pupil displacement d (red line). For better illustration, the Zernike vertical coma coefficient $c(3,-1)$ distribution is also shown.

Figure 4.5 presents an example of a correlation assessment between the distribution of the total *RMS* (blue line) and displacement distance of the pupil centre d (red line) from the *CCD* centre. It also shows the distribution of vertical coma coefficient

$c(3,-1)$ (dashed line) in respect to both curves (note, that arbitrary units are used for an illustrative purpose, units of the coma and total *RMS* wavefront error were measured in microns, whereas the displacements of the pupil centre is shown in millimeters). The Zernike vertical coma coefficient $c(3,-1)$ curve was plotted additionally, since its variation in amplitude is often a good indicator for pupil displacement. The correlation coefficient for aberration coma and the pupil displacement d was also checked for all cases, but it likely appeared significant together with not negligible correlation between the total *RMS* and d . Both presented trials for Subject *MC* were taken under the same conditions after a precise alignment of the pupil centre with the optical axis of the instrument. In the first case of trial no. 1, it is clearly seen that the value of r is not negligible (being 0.84 positive) and both distributions are well correlated (75 percent). This observation disqualified the data set from trail no. 1, since all wavefronts would be affected mainly by the drift of the pupil centre. Although, the trial no. 1 was lost for this subject, trial no. 9 showed a minimum correlation between both distributions. In this case, the correlation coefficient appeared much smaller and there is no significant signs of mutual correlation of the total *RMS* and pupil displacement d .

The second "qualification" was focused on a single wavefronts within already qualified trails. Here we adjusted sensitivity for the pupil centre movements by creating a tolerance range of $\pm 250 \mu\text{m}$ from the "zero" position (the initial central point, is the pupil centre aligned with the centre of the *CCD* detector) in the horizontal and vertical directions. This aims to reduce effects occurring from the random motions of the eye (eye drifts [164]) during measurements. The $250 \mu\text{m}$ tolerance is approximately 4 percent of the 6 mm pupil diameter. Figure 4.6 illustrates this "sensitivity window". All solid dots correspond to a position of the centre of the pupil recorded for each single wavefront ($n=20$) measured along 12 second time. Red dots represent positions of the pupil centre outside the tolerance range and hence wavefronts associated with those points were removed from further analysis. The choice of this sensitivity window of $\pm 250 \mu\text{m}$ arose from the fact that for even an experienced subject, keeping their eye within the required range was not straightforward. Decreasing dimensions of our "window" even to $\pm 200 \mu\text{m}$ would result in additional removing more than 15 percent of data, which in total would give almost 50 percent (averaged) of data waste.

Our two steps evaluation process eliminated 321 frames (wavefronts) were removed from the total number of 1000 measurements points collected for all subjects in order to do more reliable analysis (5 subject, 10 trials each, 20 wavefronts within single trial). This gave us about 68 percent of remaining data that is used in the following analysis.

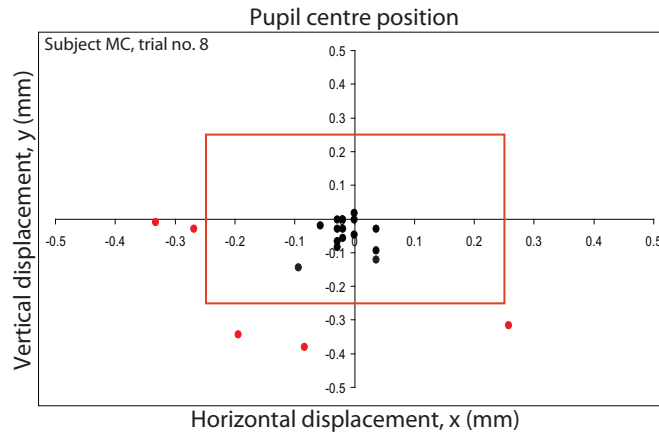


Figure 4.6: An illustration of the "tolerance" window for the center of the pupil displacement. The red dots correspond to the rejected measurements, since the pupil center drifted too far from the initial center of the coordinate system.

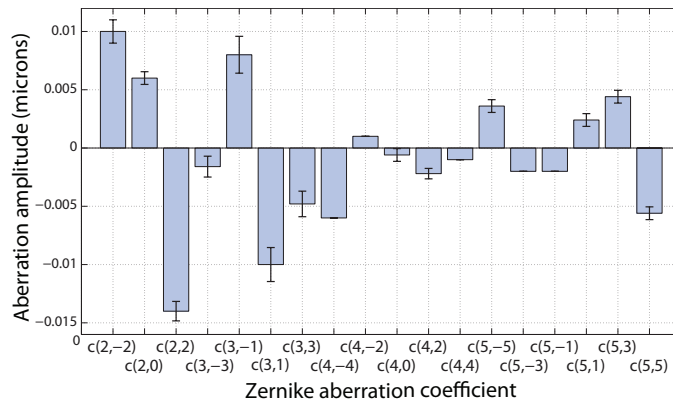


Figure 4.7: Mean values of Zernike aberration coefficients ($n = 100$ wavefronts) obtained from an artificial eye for a 6 mm pupil diameter. Error bars are $\pm 1\text{ SD}$.

We are aware that all changes within gathered wavefronts were caused by some other factors, but we assume, that we measured the optical effect of the tear film fluctuations on the corneal surface with sufficient certainty. Figure 4.7 presents a noise level for our instrument. It shows an averaged values of 18 Zernike coefficients obtained with a consecutive measurements of an artificial eye (AE). As in the previous Chapter, the AE consists of a diaphragm, achromatic doublet lens $f = 50\text{ mm}$ and the piece of white paper acting as a reflection medium. The averaging includes data collected over 5 single measurements (100 single wavefronts) from which a standard deviation error (SD) was calculated. The mean total RMS error is equal to $0.025 \pm 0.001\ \mu\text{m SD}$, which we regard as noise level of the aberrometer. Small values of the SD error,

approximately 0.001μ for the 2^{nd} and the 3^{rd} order Zernike aberrations, indicate reasonably good repeatability and stability of the aberrometer itself.

A significant effort has been made to find interactive pattern between the optical system of the human eye and cardiopulmonary or respiration systems of the human body. As an example it is worth referring to recent work of Michael Muma and Robert Iskander [165]. By using nonstationary measures of signal coherence, they found some moderate interactions between the respiration, and weak coherence between the blood pulse and the eye's aberrations. However, the influence of cardiopulmonary system on aberration dynamics of the human eye has been found to be high [159], there is still some obscurity regarding the weight of the mutual interactions between these two factors as Hampson *et.al* showed rather weak correlation [166]. With the selection process, described above, we assume that in our selected data the strongest contribution to the ocular aberration fluctuation, within 12 *seconds* time period, comes from the tear film.

4.3 Experimental Results

Figure 4.8 shows a distribution of the remaining *RMS* wavefront error ("x" - data point markers) along the 12 *seconds* time period after a single blink. A single data point represents the *RMS* of each individual wavefront reconstructed with the Zernike polynomials up to 5^{th} order. The list of experimental trials qualified for further analysis is always given for a particular subject, however the total number of single data points within one full trial is not always equal 20. The blue curve shows the variation of averaged total *RMS*. At this stage, we cannot analyse our experimental data, since here we present only original or "*raw*" data after data collection and reliability assessment processes. We shall keep in mind here, that using only total value of the *RMS* is not sufficient to describe the optical effect of the tear film variation. Nevertheless, Fig. 4.8 gives an idea about how the *RMS* may vary along the time axis. It also shows the total number of data points gathered for each subject. For instance, the mean distribution curve of the *RMS* for Subject *MC* is characterized by the lowest number of data points, which may cause the data to be less reliable compared to the rest subjects from our study. However, before we make our final judgement we shall look more into the details of our results.

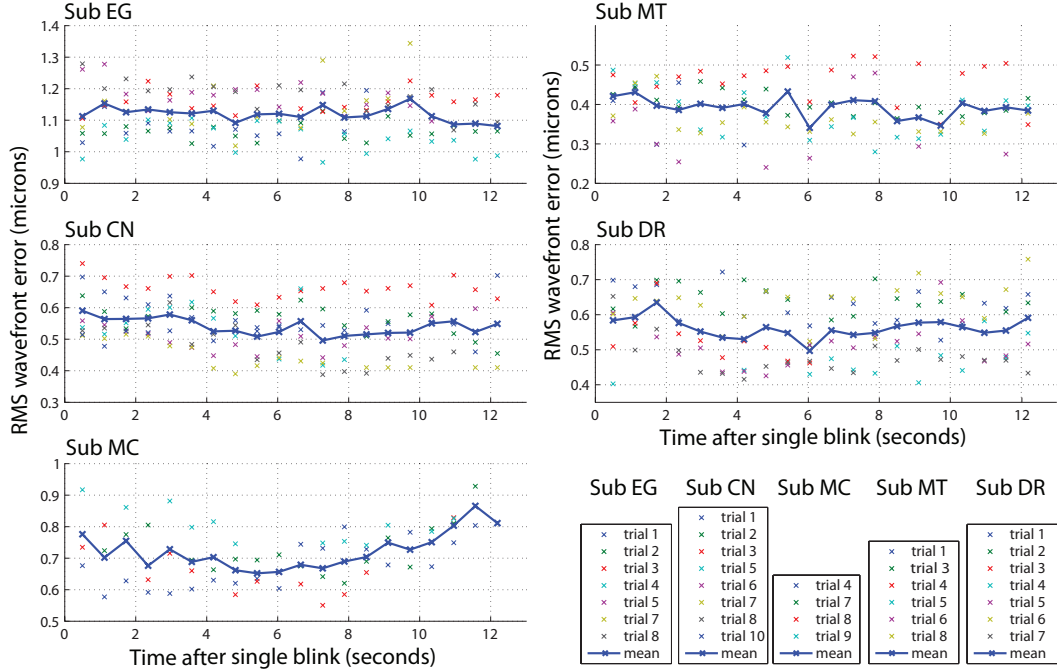


Figure 4.8: Distribution of the selected data points (wavefronts), and the mean total RMS wavefront error along the 12 *seconds* time period after a single blink for 5 subjects. The RMS wavefront error for a single data point was estimated including Zernike terms up to 5th order. The mean RMS (mark as blue, thick curve) is an averaged value of each trial RMSes for particular time point. Note, that the scale in the vertical axis (RMS in microns) is different for each subject.

In order to find evolution of the tear film wavefront RMS, we computed the residual wavefront map W_R for each data point. To do so, firstly we define the reference wavefront phase map W_{Ref} for each trial. The reference aberration wavefront W_{Ref} is the averaged wavefront of all single frames qualified for a given trial within 12 *seconds*. Next, the residual wavefront maps were obtained by subtracting the reference wavefronts from each single experimental wavefront W_i independently of its position on the time scale. A simple expression, that describes this step in data analysis is given below:

$$W_R = W_i - W_{Ref} \quad (4.3)$$

Computing the residual wavefront map allows us to follow the changes in aberrations induced by the tear film variation. Figure 4.9 illustrates graphically the results of subtracting W_{ref} for Subject *EG*. Looking at the residual wavefronts W_R one can easily see the variation of the RMS caused by the evolution of the tear film on the corneal

surface. Note, that for clarity, only 8 phase maps from the total of 20 are shown, but still we are able to observe the gradual increase in the residual *RMS* with time.

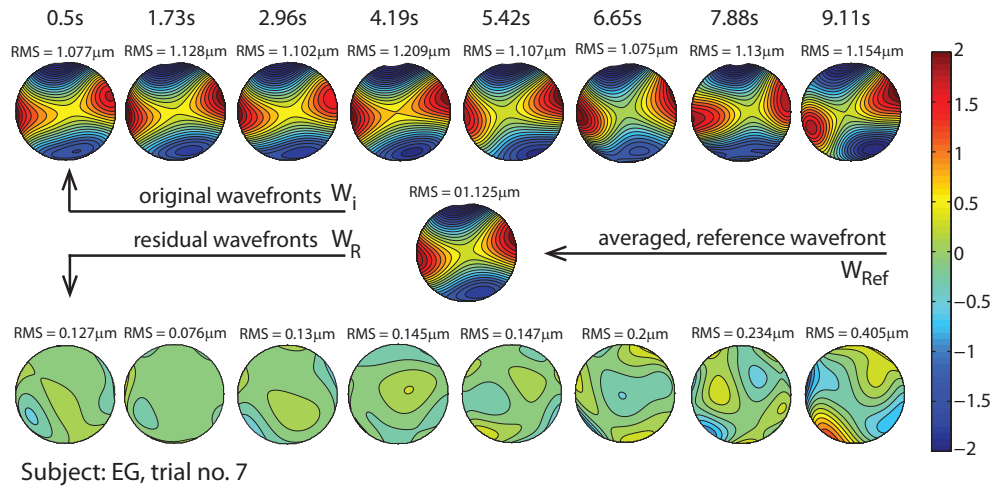


Figure 4.9: Set of phase maps of Subject *EG* (trial no. 7). Averaged (reference) wavefront W_{ST} was subtracted from original wavefronts W_i in order to find residual wavefronts W_R . Note, that for clarity, only 8 phase maps from the total of 20 are shown and the capture time is displayed for each pair of W_i and W_R . All wavefronts were reconstructed by 18 Zernike aberration polynomials (9tp/tilt removed) over a 6 mm pupil diameter.

Figure 4.10 presents effects of subtraction for all subjects in our experimental group (some curves may be incomplete due to the selection process). Although at first sight it may appear as a random distribution, we shall be able to distinguish its essential phases at this stage. Considering the evolution of the residual *RMS* value for single trials one can easily see an increase of the wavefront error immediately after the blink. This may be associated with the build-up time of the tear film. After certain period of time, which varies within subjects, a tear film break up phase takes a place, which results in increasing of the residual wavefront error *RMS*. Although Fig. 4.10 allows us to track variation of the individual trial, it does not give a clear evidence about the influence of the tear film on the intrinsic aberrations of the eye. Thus, our next step is to find a mean values of the residual *RMS* from data points assigned to the same time interval after a single blink.

Results presented in Fig. 4.11 show a typical variation of the residual *RMS* wavefront error for 12 seconds after a rapid blink. This method of obtaining the mean values of *RMS*, calculated directly from single data point wavefront *RMSes*, leads us to use the absolute values of each Zernike coefficient and thus, a maximum amplitude of

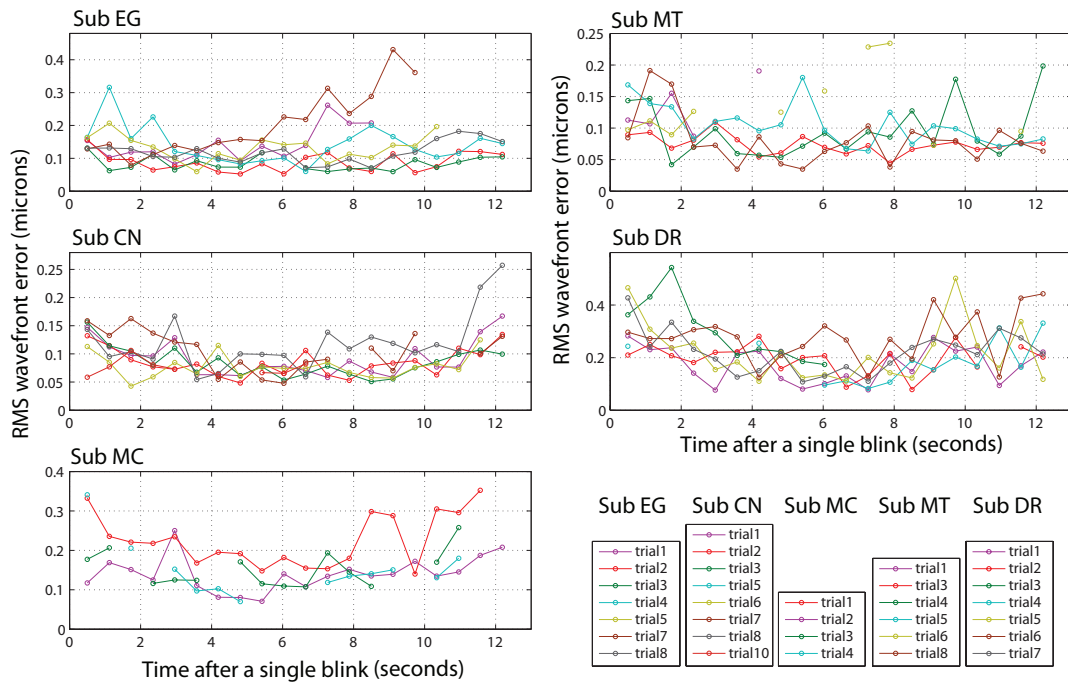


Figure 4.10: Evolution of the residual *RMS* wavefront error for single trials (data series) over 12 seconds for each subject after single blink (point "0" on the time axis). As a result of subtraction, each new "residual" trial is shown with a different colour. Note, that the scale in the vertical axis (*RMS* in microns) is different among the subjects.

averaged *RMS* value may be observed for each eye. Our results presented in Fig. 4.11 indicate that the tear film affects the amount of total ocular aberrations and its contribution to the overall *RMS* value varies from eye to eye. Similarly to our previous considerations we are able to identify noticeable changes in the distribution of the mean (absolute) *RMS* error. All our measured eyes exhibit an initial drop of the amount of residual aberrations. Furthermore, as a consequence of build-up time, the region of the lowest value of the wavefront error, which correspond to the stability phase of the tear film, may be observed. After these two phases of the tear layer distribution on the front corneal surface, the tear film disruption take a place. Evidently the time duration for each phase varies from eye to eye, but we can give the averaged time during which, the *RMS* error of the residual wavefront reaches its minimum. It is on average 5.0 ± 1.6 seconds (*SD*) after a rapid blink. We are also able to approximately identify the averaged stability time T_S as from 3.0 to 6.4 ± 0.8 seconds (*SD*). This is in line with previous findings of Németh *et.al*, who found the corneal surface to be more regular between 3,2 and 11.0 seconds after a blink [167].

In order to illustrate some other findings from the data analysis, we shall consider the

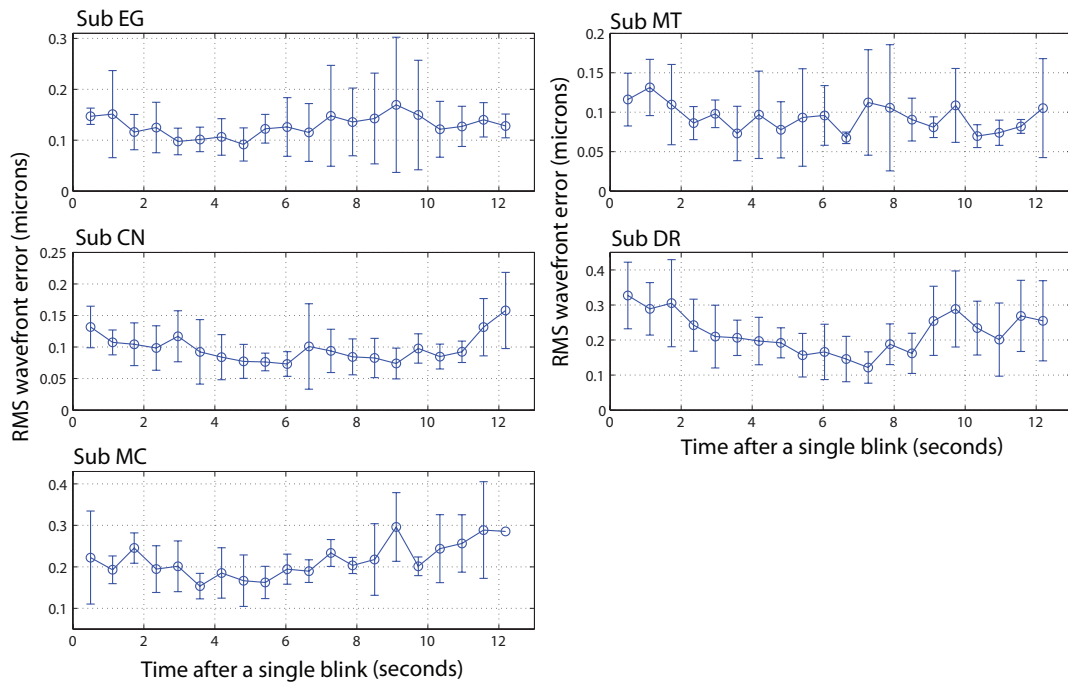


Figure 4.11: Evolution of the mean residual *RMS* wavefront error over 12 *seconds* for each subject in our experimental group, ± 1 *SD*. Note, that presented mean values of the residual *RMS* were obtained by averaging the *RMS* values from Fig. 4.10, for each point on the time axis. It means, that here we deal with absolute values of each Zernike coefficient in order to obtain a maximum amplitude of mean wavefront.

next stage. At this point we shall look for evolution of single Zernike coefficient or Zernike aberration families. When examining the distribution of Zernike coefficients, we assumed that all movements of the eye are minimized and the eye accommodation is fully paralyzed and hence the variations in ocular aberrations can be attributed to the tear film. This is, however, an optimistic assumption, since we are already aware of a number of dynamic factors in the eye. On the other hand we believe that the strongest influence on changes in the total *RMS* of ocular aberrations comes from the tear film. Figure 4.12 shows three Zernike aberration orders from the 2nd to 4th and evolution of the mean *RMS* wavefront shown as a thick blue curve. It is important to point out that we average each Zernike coefficient at the same location in time, and hence we include the information about the sign differences between Zernike aberration coefficients. It results in lower values of the mean *RMS* compared to those in Fig. 4.11(absolute *RMS* values).

In order to evaluate image degradation in the eye due to the tear film, we show the theoretical level of diffraction limit (black, dashed line). This limit helps to assess the

image quality and it is known as Maréchal criterion (1947). It states that the optical system is usually referred to as a diffraction-limited one when $RMS \leq \lambda/14$. It means, that below this level (*i.e.* $0.048\mu m = \lambda/14, \lambda = 0.677\mu m$) the dominant factor in degrading the image quality is diffraction of light. It also corresponds to 0.8 of Strehl ratio.

Figure 4.12 gives an idea how different Zernike aberration orders are fluctuating along 12 seconds of measurements after a single blink. It can be seen, that, not surprisingly, very strong contribution to the total amount of residual wavefront error RMS, comes from the 2nd Zernike aberration order. The Zernike aberration coefficients from the 3rd, and 4th fluctuate with a comparable amplitude along the level close to the one of diffraction limit. The aberration terms from the 5th were not plotted, since its significance for the total amount of aberrations is negligible.

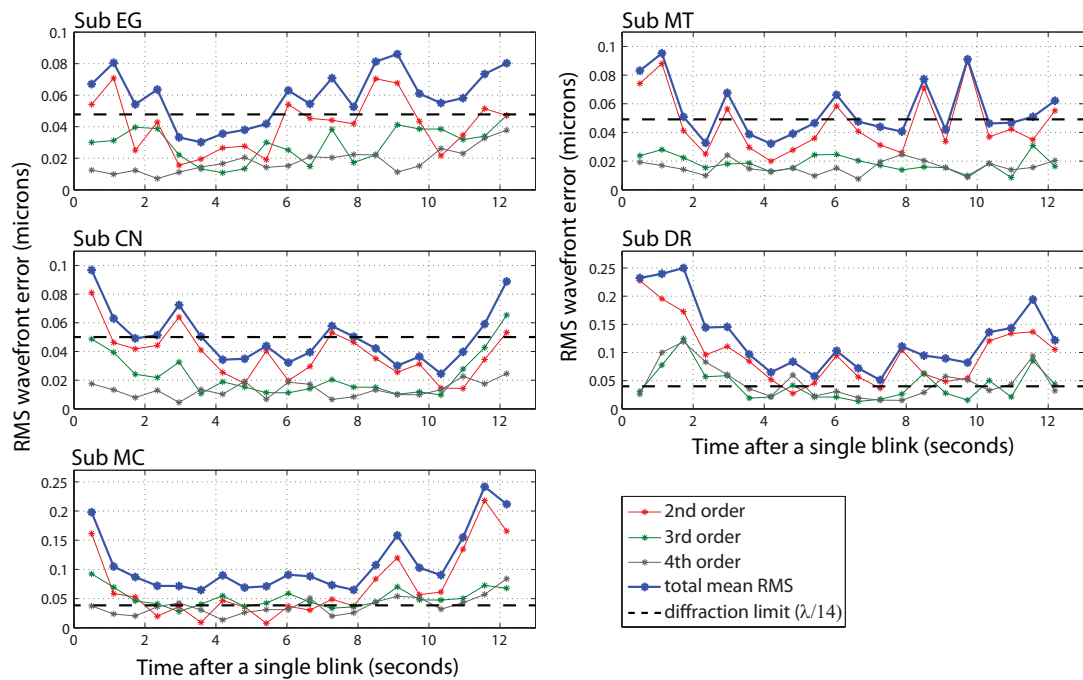


Figure 4.12: Evolution of residual Zernike aberration coefficients (orders 2nd, 3rd, and 4th) during 12 seconds after a single blink. Here, each Zernike coefficient was averaged preserving its sign. The black, dashed, horizontal line corresponds to the diffraction limit for the wavelength of 677 nm, used in experiment. For the sake of clarity, error bars have been omitted.

As we have already mentioned, the Zernike coefficients from the 2nd order determine the weight of aberrations induced by the changes in the tear film topography. Figure 4.13 illustrates variation of the Zernike aberration defocus coefficient $c(2,0)$,

and combined terms of the 2nd order Zernike astigmatism family (i.e. $((c(2, -2))^2 + c(2, 2)^2)^{1/2}$).

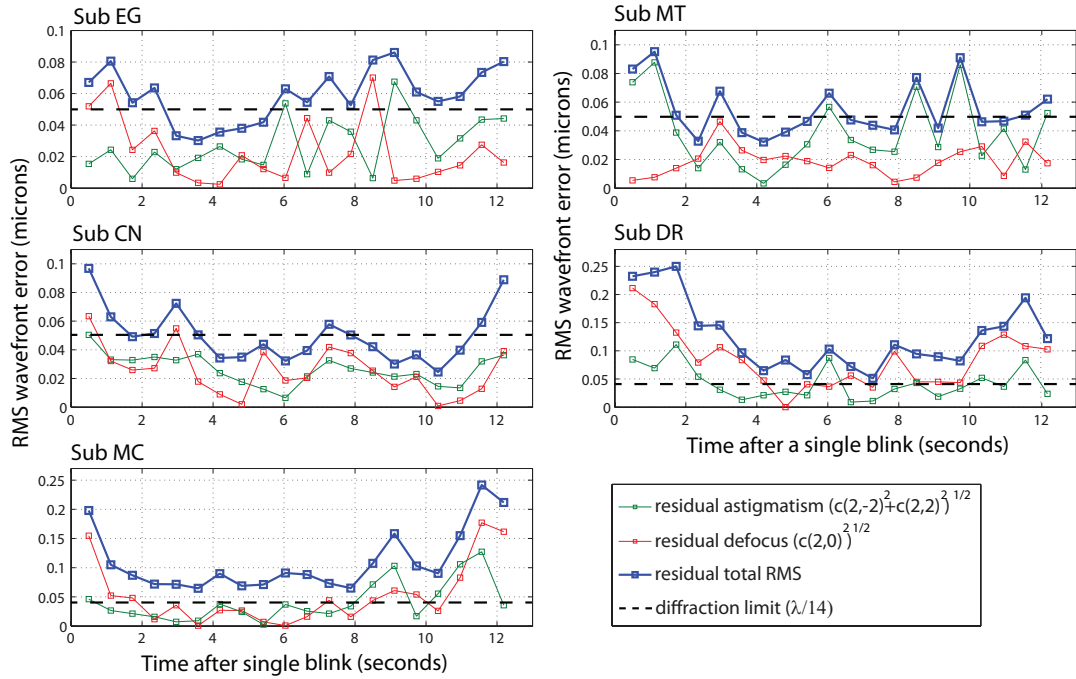


Figure 4.13: Distribution of the residual mean Zernike lower-order aberration coefficients: defocus, and a combined astigmatism family including Zernike astigmatism coefficient $45^\circ - 135^\circ c(2,-2)$ and $90^\circ - 180^\circ c(2,2)$, during 12 second after a single blink. The black, dashed, horizontal line corresponds to the diffraction limit for the wavelength of 677 nm, used in experiment. For the sake of clarity, error bars have been omitted.

This gives an idea how these aberration term are evolving after the tear film is redistributed by the preceding blink. We can observe various evolution patterns of Zernike defocus and astigmatism and compare their amplitudes to the diffraction limit level. In the case of Subject *EG*, lower-order terms exhibit large variation after 6th-second of measurement, indicating, that the tear film break-up process has started after this point. Using the same vertical scale we can compare this distribution with two other subjects *MT* and *CN*. Subject *MT* shows more variation from combined astigmatism terms after possible break-up time, whereas subject *CN* displays less variation in terms of lower order terms, being below the diffraction limit. Compared to subject *DR*, subject *MC* shows more stable pattern between 1st and 8th second, whereas in the case of subject *DR*, Zernike defocus aberration plays a main role above the line of 0.048 μm . We are aware that because of limited number of subjects in this study, the

clear statement about the distribution patterns of the Zernike 2^{nd} order aberrations is not possible (similar to the findings of Shizuka Koh *et.al*, and their higher-order aberrations distribution pattern [168]). Which of the 2^{nd} order Zernike coefficient is more susceptible to the tear film fluctuation? There is no simple answer to this owing to high inter-subject variability and relatively small sample (5 subjects).

It has been shown that even relatively small-amplitude, higher-order, irregular aberrations (*HOA*) found in normal healthy eye significantly degrade the image quality on the retina [9, 147, 159]. Higher-order aberration terms are also found to fluctuating as a results of optical changes in the tear film [93, 98, 115, 161, 163, 168, 169]. Moreover, the study of Zhu and Iskander showed some strong relations between higher-order terms and the cardiopulmonary system [159]. Some authors, for instance Zhu *et.al*, concluded their study with a statement that measurements of the higher-order aberrations may give an answer about tear film dynamics and its effect on the quality of vision [168]. In light of this, we shall look for residual values of higher-order terms.

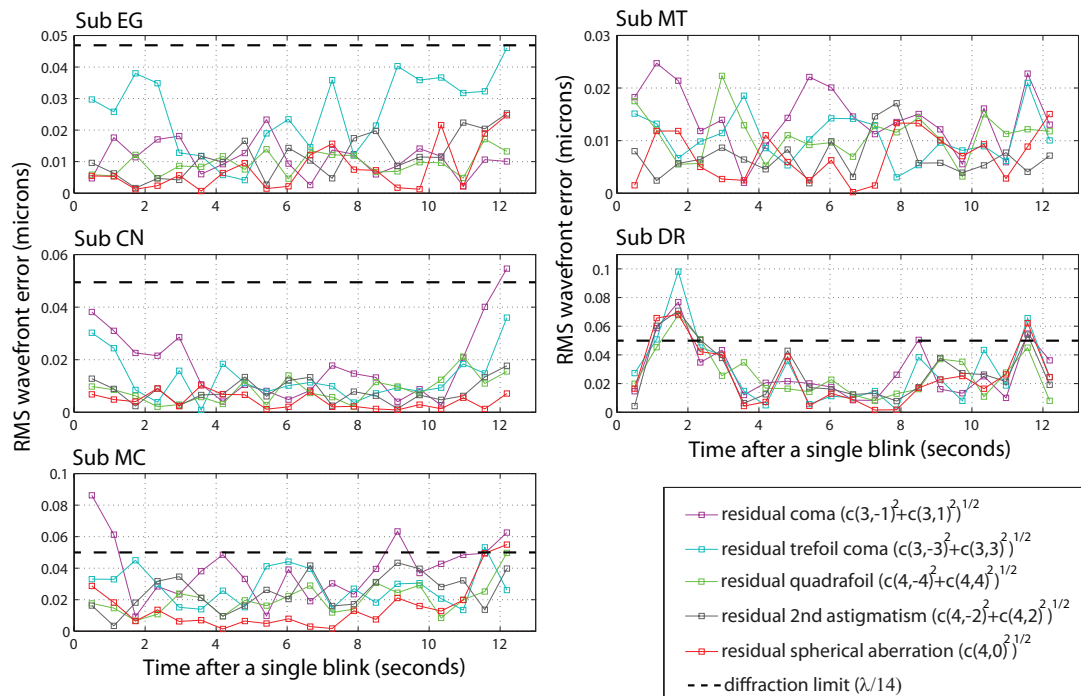


Figure 4.14: Distribution of the combined, residual mean Zernike higher-order aberration coefficients: coma, trefoil coma, quadrafoil, 2^{nd} astigmatism, and spherical aberration, during 12 seconds after a single blink. The black, dashed, horizontal line corresponds to the diffraction limit for the wavelength of 677 nm, used in experiment. For the sake of clarity, error bars have been omitted.

Figure 4.14 depicts higher-order Zernike coefficients grouped in the families of the same kind of aberration. We picked the higher-order terms only up to 4th order, since Zernike aberration coefficients from the 5th order are likely to oscillate close to the "zero" level in amplitude. At first sight, a decomposition of the higher-order terms looks more random than lower-order distribution in Fig. 4.13. It is due to the fact that they are more sensitive to the changes caused by the tear film distribution on the corneal surface (e.g. local changes in thicknesses of tear or refractive index changes between optical surfaces). Although, it is not easy to give a full interpretation of experimental data based on Fig. 4.14, we shall be able to spot some characteristic details. Subject *EG* shows a dominance in amplitude from a trefoil coma group and significant drop of all presented terms at about 4th second after a single blink. Subject *CN*, with a similar amplitude of the *HOA*, indicates even longer time interval between the build-up and brake-up time. In this case, a coma-like group mainly enveloping the other higher-order terms. Subjects *MT* and *MC* do not display any significant tendency, whereas subject *DR* attracts our attention due to highly ordered distribution of the *HOA* along the 12 second period.

In order to see more clearly how the higher-order Zernike aberrations fluctuate in amplitude, we use Figure 4.15. It shows the residual *RMS* of the *HOA* for each eye, which helps to understand a general behavior of these terms, after a tear film is redistributing on the front surface of the cornea. Here again we calculated the mean results from an absolute values of the *HOA RMS*, which is useful indication of the total *RMS* wavefront error at a given point in time. The *SD* values illustrate variation of the *HOA* residual *RMS* between experimental frames. It is easy to spot a sinusoidal distribution for subjects *MT* and *DR* in time. Perhaps it is not representative observation, nevertheless the Zernike coefficients from the higher-order group show characteristic decomposition, which can be related to the changes in the tear film topography. Furthermore, a sudden rise of the *SD* error may indicate a lack of stability of the layer of tear. This is in line with previous results of Koh *et.al*, which clearly showed, that the *HOA* after tear film break-up were significantly increased compared with those prior to tear film break-up [163].

Figure 4.16 shows the group average standard deviation (*SD*) of each Zernike coefficient (up to the 5th order) and their standard error of the mean (*SEM*). This shows which of the single Zernike coefficients varies the most within full set of 18 terms due to the pre-corneal tear film fluctuations. Usually the variations of total *RMS* wavefront error is due to the fluctuation of the lower-order terms. However sometimes higher-order Zernike aberration terms might give a significant contribution to the to-

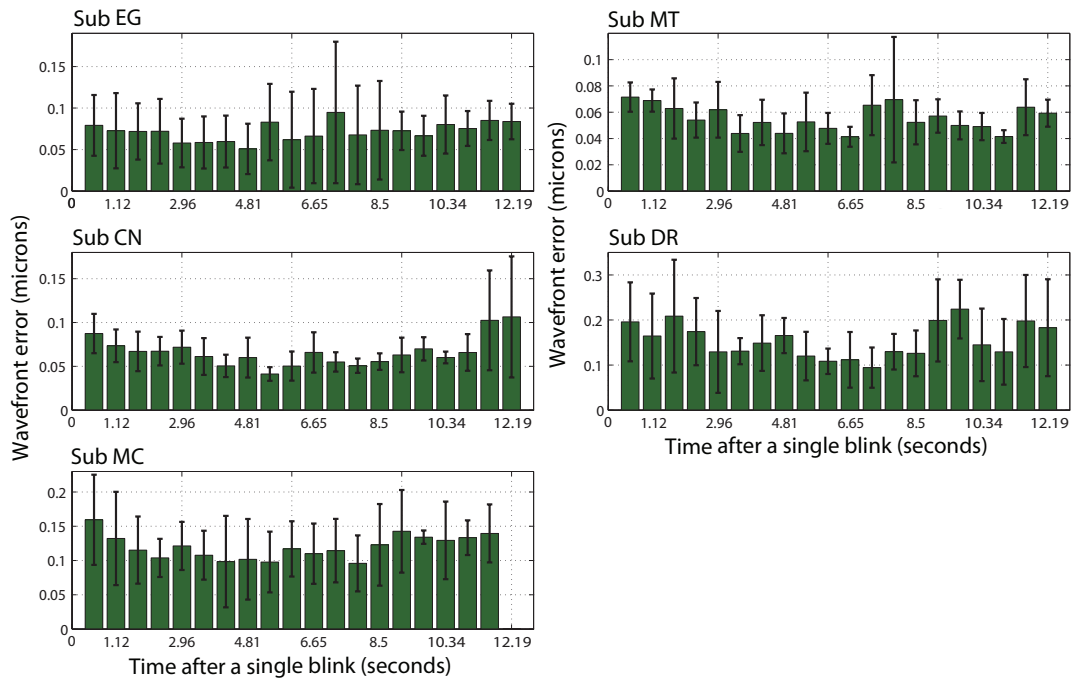


Figure 4.15: Distribution of the mean, absolute values of the residual higher-order RMS wavefront error ± 1 SD. Higher-order aberration terms include 3^{rd} , 4^{th} and 5^{th} Zernike aberration orders.

tal RMS wavefront change. The amplitude of variation for each Zernike component differs from eye to eye. For subject *EG*, the highest variation can be observed for the defocus coefficient $c(2,0)$ equal to $0.16 \pm 0.04 \mu m$ of the SD wavefront error. The amplitude of variations of the remaining aberration terms decrease as the Zernike order increases. Subject *MT* indicates the highest fluctuation for the "with-the-rule" Zernike astigmatism coefficient $c(2,2)$, and similar level of variation (about $0.04 \mu m$) for Zernike terms from the 3^{rd} level. Similar situation may be observed for subject *CN*, with small differences in amplitude between Zernike aberration coefficients: vertical trefoil coma $c(3,-3)$, horizontal coma $c(3,1)$ and horizontal trefoil coma $c(3,3)$, vertical coma $c(3,-1)$. In case of subject *DR*, besides the large amplitude of fluctuation from the 2^{nd} order terms, there is a significant variation of horizontal trefoil coma $c(3,3)$, secondary diagonal astigmatism $c(4,-2)$, spherical aberration $c(4,0)$, and horizontal quadrafoil $c(4,-2)$ Zernike aberration coefficients. The vertical coma component $c(3,-1)$ reaches the highest level of the SD wavefront error, being at $0.13 \pm 0.03 \mu m$, for subject *MC*. It also displays non negligible magnitude of variation for the horizontal trefoil coma $c(3,3)$ and secondary vertical coma $c(5,-1)$ coefficients. For this subject, diagonal astigmatism $c(2,-2)$ and Zernike defocus aberration are on the same level in terms of

variation magnitude, being around $0.09 \mu m$.

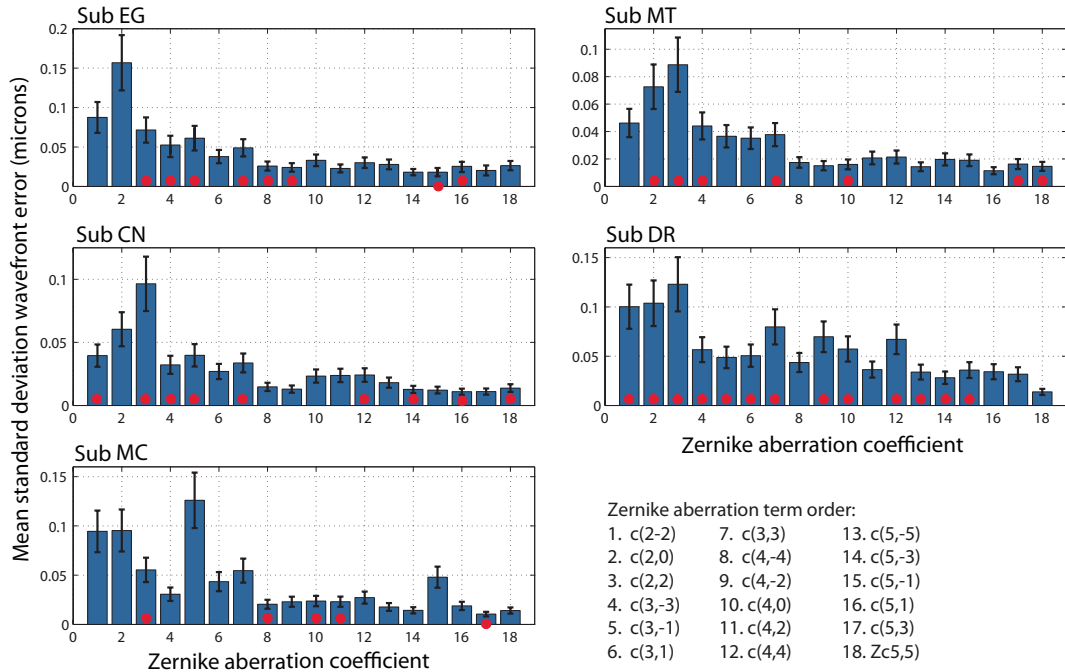


Figure 4.16: Group mean standard deviation (*SD*) of each subject for each Zernike aberration coefficient. Data presented, are the mean of multiple trials for a particular subject. Error bars are ± 1 *SEM*. Red dots represent these of the Zernike aberration coefficients that are significant correlated with the time after a blink. Statistical significance was set to the $p < 0.05$ level.

Red dots in Fig. 4.16 indicate the Zernike aberration coefficients, which were found to be significant correlated with the time after the blink. In order to find such a correlation consecutive paired Student's t-tests were performed for each Zernike aberration coefficient. Statistical significance was set to the $p < 0.05$ level. Within our group of 5 eyes, the most frequent aberration coefficients that undergo a significant fluctuations with a time after the blink are: horizontal astigmatism $c(2,2)(p = 0.004)$, spherical aberration $c(4,0)(p = 0.001)$, and coma-like aberration coefficients: vertical trefoil coma $c(3,-3)(p = 0.006)$, horizontal trefoil coma $c(3,3)(p = 0.01)$, vertical coma $c(3,-1)(p = 0.01)$ and secondary vertical coma $c(5,1)(p = 0.01)$. This suggests that not all aberration terms are sensitive with the same magnitude to the tear film fluctuations.

The additional amounts of the *RMS* wavefront error caused mainly by fluctuation of tear film on the corneal surface are presented in Table 4.1. The Zernike aberration

orders from 2nd to 5th and the mean *RMS* error, show variation in residual wavefronts due to tear film changes. It also shows inter-subject variability. Although the number of subjects in this study might be not sufficient for far-reaching conclusions, we were able to detect a non negligible optical effects of tear film due to its temporal variation on the cornea. The main value of residual *RMS* indicates that the amount of wavefront aberrations, caused mainly by the changes in the *TF*, is oscillating around $RMS = 0.11 \pm 0.05 \mu m$ *SD*. The importance of this estimation is such that it is equal to the amount of *RMS* wavefront error for the region on the retina considered as isoplanatic patch in previous Chapter.

Table 4.1: Additional wavefront aberration caused by a tear film variation (given in *RMS* error). Errors are $\pm 1SD$ (standard deviation).

Subject	mean <i>RMS</i> μm	2 nd order <i>RMS</i> μm	3 rd order <i>RMS</i> μm	4 th order <i>RMS</i> μm	5 th order <i>RMS</i> μm
EG	0.06 ± 0.02	0.04 ± 0.02	0.03 ± 0.01	0.02 ± 0.01	0.02 ± 0.01
MT	0.06 ± 0.02	0.05 ± 0.02	0.02 ± 0.01	0.020 ± 0.005	0.010 ± 0.004
CN	0.05 ± 0.02	0.04 ± 0.02	0.02 ± 0.02	0.01 ± 0.01	0.010 ± 0.004
DR	0.13 ± 0.06	0.10 ± 0.05	0.04 ± 0.03	0.05 ± 0.03	0.03 ± 0.01
MC	0.11 ± 0.05	0.10 ± 0.05	0.05 ± 0.02	0.04 ± 0.02	0.04 ± 0.01
Mean	0.10 ± 0.04	0.06 ± 0.03	0.03 ± 0.01	0.03 ± 0.02	0.02 ± 0.01

Table 4.2, presents values of the *RMS* of grouped Zernike aberration terms that were found to be highly correlated with a time after a blink. From Fig. 4.13 it can be clearly seen that the contribution from 2nd order astigmatism terms to the variation of the residual *RMS* is crucial for some subjects. The higher-order aberration coefficients shown in Table 4.2 are coma-like aberrations and spherical aberration. In order to see the distribution of these aberrations in time after a blink one can refer to the Fig. 4.15 where the amounts of the *RMS* error of the grouped higher-order aberrations as a function of the time after a blink are plotted. It clearly shows that coma-like aberrations undergo the largest variation in amplitude after a single blink.

From our data analysis presented in this chapter we can conclude that wavefront aberrations should be measured carefully to avoid the undesirable effects of pre-corneal tear film evolution (e.g. break-up). This is especially important in wavefront-guided refractive surgery. The Shack-Hartmann based wavefront measurements, may be a reliable tool in analysis determining the effect of the tear film after blinking on the optical quality of the entire eye. In light of such a "delicate" matter like the tear

Table 4.2: Additional wavefront aberration caused by a tear film variation (given in *RMS* error). **SA** stands for spherical aberration coefficient. Errors are $\pm 1SD$ (standard deviation).

Subject	2^{nd} o. ast. <i>RMS</i> (μm)	3^{rd} o. coma <i>RMS</i> (μm)	3^{rd} o. tref. coma <i>RMS</i> (μm)	5^{th} o. coma <i>RMS</i> (μm)	SA <i>RMS</i> (μm)
EG	0.028 ± 0.017	0.011 ± 0.005	0.026 ± 0.012	0.013 ± 0.008	0.008 ± 0.007
MT	0.038 ± 0.025	0.014 ± 0.006	0.011 ± 0.005	0.008 ± 0.003	0.007 ± 0.0045
CN	0.026 ± 0.011	0.018 ± 0.014	0.013 ± 0.008	0.006 ± 0.004	0.004 ± 0.003
DR	0.043 ± 0.030	0.028 ± 0.020	0.030 ± 0.024	0.017 ± 0.013	0.025 ± 0.021
MC	0.041 ± 0.035	0.040 ± 0.020	0.030 ± 0.011	0.015 ± 0.011	0.015 ± 0.015
Mean	0.035 ± 0.008	0.022 ± 0.011	0.021 ± 0.009	0.012 ± 0.005	0.012 ± 0.008

film distribution on the corneal surface, we shall be aware of some factors that can make difficult our final judgement of its impact on vision. These are main factors: eye movements, accommodation, errors in alignment.

Chapter 5

Conclusions

The main purpose of the thesis is to acquire a better understanding of image formation in the human eye. Considering the overall effect on the peripheral image quality on the retina we shall note that the retinal image will be aberrated not only by lower-order Zernike terms (e.g. astigmatism and defocus), but also by the higher-order terms. One of the main goal in measuring the field dependent aberrations is to explore the symmetry and its presence in various characteristics of the optical system of the eye. The knowledge about these gives us an opportunity to interpret the field aberration pattern in terms of the optical structures of the eye and the shape of the retinal surface and in particular its position (orientation) with respect to the line of sight.

Our experimental data for a young population has confirmed the previously-reported significance of the lower-order aberrations to the image formation on the retina. The defocus and astigmatism measured experimentally across the central visual field show larger growth in comparison with the changes of other aberration terms. Understanding the field-dependent nature of lower-order aberrations is of high interest for optical design of future ophthalmic instruments.

We have shown that the changes in the tear film on the front surface of the cornea have a non-negligible effect on the fluctuations of the ocular wavefront. This effect should be taken into account when the optical properties of the eye are reconstructed from the ocular wavefront measurements [60]. In general, one has to average out the tear film optical effect when constructing a subject-specific eye model intended

for wavefront-guided eye surgery or intra-ocular lens fitting. One can do it by time averaging of wavefront measurements prior to eye reconstruction.

5.1 Field Dependence of Ocular Aberrations

In our study of the field-dependence of ocular aberrations, we investigated 25 eyes of young and healthy subjects without any optical abnormalities under cycloplegia conditions. The aberrations of the wavefronts were measured along the horizontal and vertical meridians up to ± 5 degree visual field with an aberrometer consisting of Shack-Hartmann (*SH*) wavefront sensor and pupil tracking system.

From the comparative analysis of our experimental data and wide-field eye models we have made several observations as follows. The various aberration groups show large inter-subject variability and the averaged value of the total *RMS* error on axis is approximately $0.5 \mu m$, which is consistent with previous findings for a 6 mm pupil [100, 129, 150]. In order to show a magnitude of subject variability in our study we look into the mean standard deviation of Zernike terms as shown in Fig. 5.1. For clarity we show only the data corresponding to the four field points and the central point at the line of sight. Error bars represent the standard error of the mean (*SEM*). The *SEM* means the standard error of the mean standard deviation (i.e. $SEM = (\overline{SD}) / \sqrt{n}$, where n is the sample size). The statistical tool we choose in order to calculate the variability is the standard deviation error (*SD*). In the work of Thibos *et.al.* [126] a large population of 200 eyes were measured in terms of monochromatic aberration pattern using a Shack-Hartmann principle based sensor. They found that the pattern of ocular aberrations undergoes the Gaussian distribution among population, hence it is fair to use the *SD* here.

Figure 5.1 illustrates inter-subject variability of Zernike aberration terms. We can note immediately that there is large variation of the horizontal/vertical astigmatism term $c(2,2)$ with similar amplitude (over the central field) equal to $SD = 0.40 \pm 0.08 \mu m$ *SEM*. The 3^{rd} order coma-like aberrations display a lower level of variability (oscillating slightly above $0.1 \mu m$ *SD*) although, besides the spherical aberrations the 3^{rd} order terms undergo a significant inter-subject variation among remaining higher-order aberrations. Spherical aberration $c(4,0)$ varies from eye to eye with a standard deviation error $SD = 0.10 \pm 0.02 \mu m$. This is the same amplitude as this aberration coefficient itself $c(4,0) = 0.1 \mu m$. This large inter-subject variability, even in the young eye population, indicates that one needs to consider wavefront aberration data on

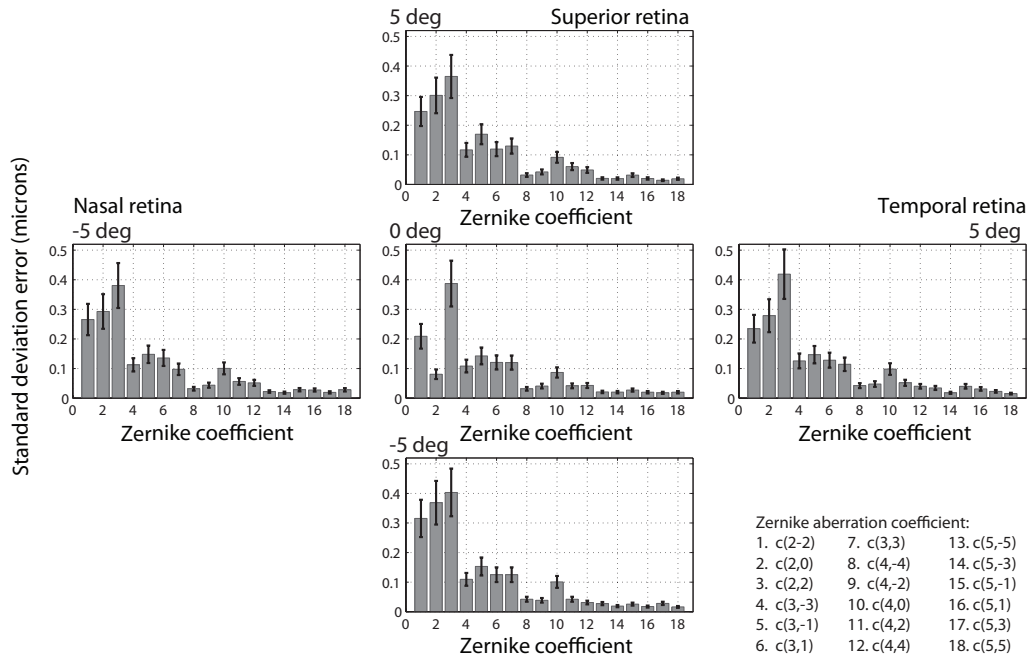


Figure 5.1: Inter-subject variability expressed as the mean standard deviation error for each Zernike aberration coefficient given in *microns*. Error bars are ± 1 SEM.

individual basis, the generic description is not representative, especially if one is interested in a customized eye model.

The knowledge about statistical distribution of ocular aberrations within a central visual field is important not only because in our every-day life we use the region of the retina close to the line of sight (*LOS*) axis, but also because of retinal imaging and other clinical applications near the fovea region. We showed a typical amount of various aberration terms that one should expect over the central visual field for young eyes. Although our experimental data is especially valuable for modeling of a typical young eye or design of new ophthalmic devices, yet we shall keep in mind that because of large inter-subject variation one should be careful in using the term "*typical*" eye.

Searching for asymmetries in mean values of aberrations across both meridians we observed that our 10×10 *degree* visual field does not display any significant difference in the total amount of aberrations between nasal - horizontal and inferior-superior side of retina. For reference see Fig. 3.9 and Fig. 3.10 (Chapter 3 "*On-axis and Off-axis Aberrations of the Human Eye*"). Perhaps this similar behavior of the horizontal and vertical meridian is only due to the small region of observation of the field distribution

of ocular aberrations. At this stage, our results do not confirm previous findings that the total amount of ocular aberrations is likely to be higher on the temporal retinal side (nasal visual field) [39, 130, 132, 170].

Figure 5.2 shows the standard deviation (SD) of averaged over 5 field points aberration terms in two meridians. Error bars represent the SEM . This shows variation of each Zernike coefficient along a given meridian. It can be clearly seen that the Zernike terms, which fluctuate the most with the field angle are those coming from lower-order aberrations. As we expected, the horizontal astigmatism term $c(2,2)$ indicates a larger variation in the horizontal meridian $SD = 0.11 \pm 0.06 \mu m SEM$, whereas the oblique astigmatism $c(2,-2)$ fluctuates more in the vertical meridian with $SD = 0.14 \pm 0.06 \mu m$.

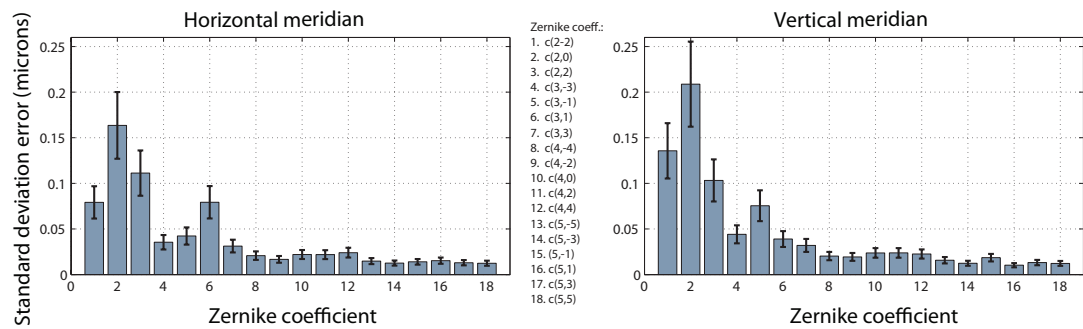


Figure 5.2: Mean standard deviation of each Zernike aberration for averaged over 5 points in two meridians. Error bars are $\pm 1 SEM$.

Not surprisingly the Zernike defocus shows the highest variation throughout the visual field, leading to $SD = 0.16 \pm 0.1 \mu m SEM$ in the horizontal meridian, and being even higher in the vertical visual field $SD = 0.21 \pm 0.09 \mu m$. Similarly to the two astigmatism terms, both components of the Zernike coma aberration fluctuate significantly in a corresponding meridian. In the horizontal meridian, the horizontal coma component $c(3,1)$ showed the variation level of the $SD 0.08 \pm 0.05 \mu m$, whereas, the vertical coma component $c(3,-1)$ was found to fluctuate more in the vertical field with similar amplitude of $SD = 0.08 \pm 0.05 \mu m$. Remaining higher-order terms from 4th and 5th Zernike aberration order indicate less variation, oscillating around $SD = 0.02 \mu m$ in both meridians. The two components of trefoil coma fluctuate between field points with an amplitude of $SD = 0.03 \pm 0.02 \mu m$, except the vertical trefoil coma $c(3,-3)$ in the vertical meridian, where it exhibits a slightly more variation of $SD = 0.04 \pm 0.03 \mu m$. This analysis shows that only few terms from the full set of Zernike aberrations (18), display a significant variation along the horizontal and the vertical visual field. As

previously described in the Chapter no. 3 (*On-axis and Off-axis Aberrations of the Human Eye*), the astigmatism, defocus and coma were found to vary the most with the field and hence they play an important role in off-axis distribution of ocular aberrations. This conclusion is in line with the previous studies [171] and [133].

We neglected the effect of the elliptical pupil when off-axis measurements were reported. The reason was a relatively small field angle (5 degree) and the fact that our simulations indicated that this source of error was negligible compared to other noise sources in the iris-edge detection process. However there is an attempt to quantify the wavefront aberration with Zernike polynomials over an elliptical pupil in the case of measurements in the far periphery [172]. There is no accepted format for reporting off-axis ocular aberrations as of time of writing. For our experiment we were measuring wavefront errors at the circular exit pupil of the aberrometer, which is sufficient for eye modeling.

Figure 5.3 shows mean values of the defocus coefficient $c(2,0)$ plotted as a function of field angle (ω).

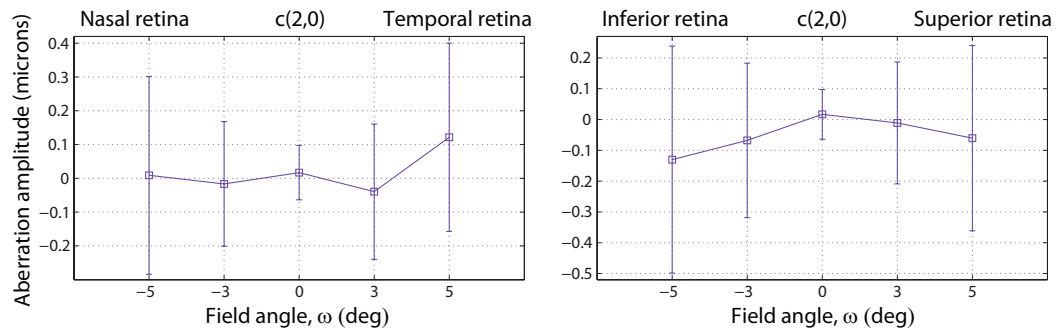


Figure 5.3: The mean Zernike defocus coefficient $c(2,0)$ plotted as a function of field angle (ω). Error bars are ± 1 SD. The mean value $c(2,0) = 0.71 \mu\text{m}$ of defocus at $\omega = 0$ has been removed from all field points.

Before we start to analyse Fig. 5.3, it is important to note, that 17 eyes, from the total number of 25 in our study, were recognized as myopic prior to the experiment. This explains the mean spherical refraction of $-0.55 D$. The plots in Fig. 5.3 show the distribution of the defocus coefficient $c(2,0)$ in the horizontal and vertical meridian. Comparing both meridians one can immediately recognize the vertical meridian as being more symmetric, whereas the horizontal meridian exhibits more irregularities. This observation is only valid for the central field, since we are unable to follow defocus growth at larger field angles. The difference in the $c(2,0)$ distribution between both meridians may be attributed to the asphericity and toricity of the retina. The

retina of a real eye exhibits various departures from a perfect sphere, typically being more prolate in a myopic group due to larger axial elongation of the eye globe. As a result, one could expect that the gradual change in defocus occurring off-axis may be different in the two meridians. The rate of the defocus growth may differ between two meridians due to the asymmetry of the retina, which has been investigated previously by measuring peripheral ocular dimensions [173]. A tendency of the $c(2,0)$ coefficient towards negative values in the vertical meridian may be related to so-called hyperopic shift of focus towards the field periphery and has been previously reported in myopic eyes [83,124]. There is less indication about general trend in the horizontal meridian. Perhaps the visual field we have explored in our population study is not enough to see a general trend in the defocus field variation. The lack of a clear quadratic field dependence and irregularities of defocus in the central visual field has been reported earlier [170].

Figure 5.4 depicts the field dependence of the mean 0-90 *degree* astigmatism coefficient $c(2,2)$ in both meridians with error bars indicating $\pm 1SD$. We show only this type of astigmatism, since it was found to have large impact to the total ocular aberrations along both meridians. The oblique-oriented astigmatism coefficient $c(2,-2)$ was not dominant in our measurements; as we expected this term contributes more along the meridians at 45-135 *degree*.

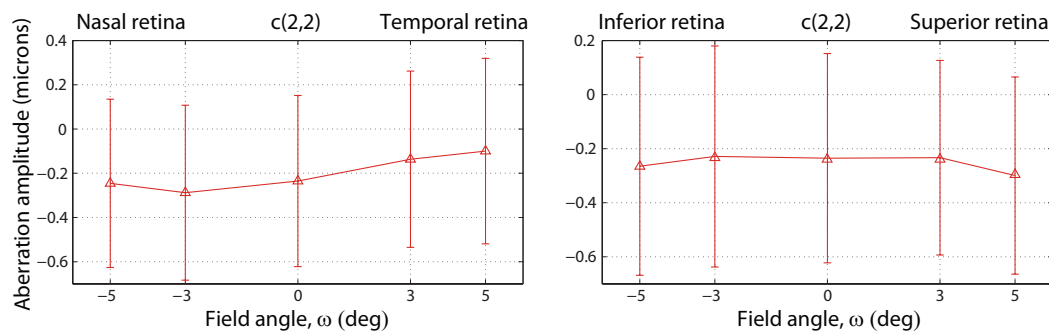


Figure 5.4: The mean Zernike astigmatism coefficient $c(2,0)$ plotted as a function of field angle (ω). Error bars are $\pm 1SD$

It has been suggested that the negative values of $c(2,2)$ astigmatism may be due to the steeper corneal surface along the vertical meridian than along the horizontal meridian. This has been reported earlier [125,142,150]. In the vertical meridian we observed suppression of the $c(2,2)$ coefficient, which may be attributed to some compensation on the line of sight axis owing to the cornea-lens balance [80,100]. This can not be clearly claim here as more data on the aberrations due to the anterior corneal surface

is needed (e.g. corneal topography together with the wavefront data would help).

Within the higher-order aberration terms, coma aberration increased linearly with the field position. Figure 5.5 presents these results in details. On the left-hand side, the horizontal component of the Zernike coma aberration $c(3,1)$ shows linear dependence with the horizontal field location. It reaches its maximum of $0.11 \mu\text{m}$ at 5 degree nasal retina and $-0.04 \mu\text{m}$ downwards in the temporal retina field. Similarly, on the right-hand side, the vertical coma component $c(3,-1)$ exhibits a linear growth across the vertical visual field. It reaches the value of $-0.05 \mu\text{m}$ in the inferior retina and $0.04 \mu\text{m}$ in the posterior retina. Our data is consistent with the common behavior in other optical systems, namely when going off-axis in a given meridian, one develops coma with orientation that is in line with that meridian. Furthermore, a linear change of coma with the field angle was reported earlier [132, 135, 171]. It is important to note here, that however the linear increase in coma aberration with the field is in good agreement with Seidel aberration theory, the lack of rotational symmetry in the eye usually results in non-zero value for coma aberration in the center of the visual field (line of sight). We can clearly see that coma is present along line of sight (or optical axis, which is likely to be along -5 degree nasal retina). Evidently we cannot regard the eye as an aplanatic system.

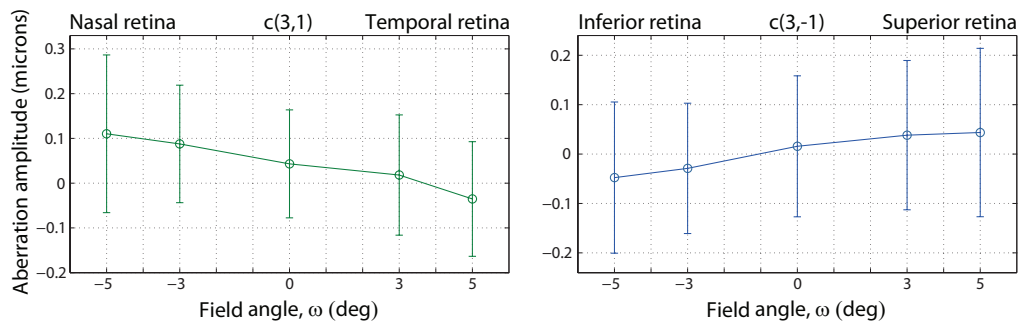


Figure 5.5: Mean coma components distribution in the two meridians. Horizontal coma coefficient (on the left) $c(3,1)$ across the horizontal visual field $\pm 1SD$ and vertical coma coefficient $c(3,-1)$ (on the right) across the vertical field of view $\pm 1SD$.

In order to look more closely into the most significant Zernike aberrations, we present three coefficients: $c(2,0)$, $c(2,2)$ and $c(3,1)$ as a function of field angle along the horizontal meridian in Fig. 5.6.

In order to find the field point, at which the three Zernike coefficients reach their minimum, the least square fitting method (with linear and quadratic fitting) was applied. This also allows us to see roughly the growth of these terms even over a wider field

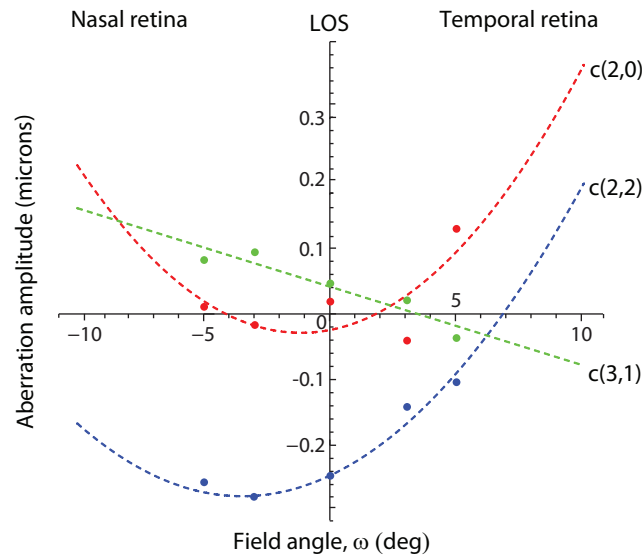


Figure 5.6: The mean Zernike coefficients $c(2,0)$, $c(2,2)$ and $c(3,1)$ plotted as a function of field angle (ω). LOS stands for line of sight. For the sake of clarity, error bars have been omitted, for more details see Figs. 5.3, 5.4, and 5.5.

of view. We admit that this is rough approximation, since there are only 5 experimental field points used in our approximation. The mean value of defocus $c(2,0)$ on-axis is not shown here as it was systematically removed by the instrument Badal system prior to measurements for each eye. Any clear statement about field-dependence of these aberration terms in relation to the classical Seidel theory is hardly possible here, due to the fact that each field-dependent aberration has an additional constant component, which drifts its minimum from the optical axis (being an approximation already). The constant component for the astigmatism $c(2,2)$ may come from cylindricity (toricity) of the cornea and additional coma $c(3,1)$ may be generated by the tilts and misalignments of the optical components of the eye. In the theoretical work of Espinosa *et.al* [78], it was suggested that the field-dependent astigmatism may be canceled by astigmatism component generated by the cornea at some points along the field. They found these points of correction for astigmatism to be around ± 5 degree in respect to the optical axis. In our case the astigmatism $c(2,2)$ reaches its minimum at field angle $\omega = -3.5$ degree (nasal retina) and zero at $\omega = -13.8$ nasally and $\omega = +6.8$ degree temporarily in respect to the line of sight. Since we do not have direct access to aberrations of the anterior corneal surface alone, we are not able to comment on possible corrections between corneal astigmatism (constant component due to corneal toricity) and classical field-dependent astigmatism component. Coma $c(3,1)$ reaches its zero at $\omega = +3.4$ degree on the temporal side of the retina. For the

$c(2,0)$ term Fig. 5.6 does not give a full information because the Badal optometer corrected the amount of defocus on-axis. However, we can observe that the minimum for $c(2,0)$ falls on $\omega = -1.2$ degree nasal retina. Taking into account the defocus amount removed by Badal on-axis we can say that this is the largest aberration term that appears on-axis and off-axis.

The lack of rotational symmetry complicates the analysis of the optical system of the eye. The possible tilts and mutual decentrations of the cornea and lens resulted in the averaged angle α , being approximately 5 degree horizontally and 2 degree vertically away from the line of sight (but can vary from eye to eye). Furthermore, even the cornea and the lens alone can display some asymmetries about their axes [1]. However, there have been several studies showing that the corneal contribution to coma is somewhat reduced by the crystalline lens [80,91], yet the eye is far from being an aplanatic system [91], since it is not free from spherical aberration and coma even at the young age. These facts bring us to general problem of modeling and interpreting aberrations in decentred optical systems. Strictly speaking Seidel theory of aberrations is valid only for rotationally symmetric centered optical systems. Ocular aberrations of individual eyes show even larger deviations compared to the irregularities we found in our averaged data. Seidel theory is still useful for analyzing the optical system of the eye. However one has to deal with an additional family of aberrations, which comes from misalignment and toricity of optical surfaces and asymmetry in the structure of the GRIN lens.

Estimation of the isoplanatic region is especially crucial for retina imaging. The size of isoplanatic patch defines the size of the visual field, that can be corrected with an adaptive optics (AO) system at any given time. In light of this, it is important to understand how the field-dependent aberrations (varying across the field at different rates) are related to the isoplanatic patch of the eye. We are aware, that we estimate this area only along two meridians, and hence we are unable to detect all asymmetrical changes in the isoplanatic region [153]. We assumed the AO corrector optically conjugated to the pupil with no other intrinsic aberration in the imaging system. We used a criterion which links the Strehl ratio (SR) and the RMS wavefront error simply as:

$$SR = \exp(-W^2), \quad (5.1)$$

where the wavefront error W is measured in rad . This creates the boundary of the isoplanatic patch, inside of which, the RMS wavefront error should not exceed $0.11 \mu m$

(hence the *SR* should be higher than 0.37). Our results indicate that the averaged isoplanatic region is approximately 2.3 ± 0.87 degree, which is comparable with earlier studies [132, 138, 153–155]. Our results are in line with theoretical predictions of the eye model based on reverse ray-tracing, we published earlier [60]. We found that because of high inter-subject variability in our study, there is a large variety in size of the isoplanatic patch.

The main result of this study is that the dominant factor in the total *RMS* of wavefront error is field astigmatism and field curvature (when defocus is removed on-axis). This means that correcting these field-dependent terms can significantly help to improve retinal imaging over central 10 degree field without using adaptive optics system. The *AO* correction would be beneficial for a small region on the retina (1-2 degree), but it is unlikely to be effective over a field larger than the isoplanatic patch [174]. Using additional deformable mirrors would complicate the instrument design and might not give sufficient correction over large fields (more than 10 degree). Our results suggest that correction of astigmatism and field curvature by traditional optics of the instrument is a promising option. A dedicated optical system with components producing variable amount of astigmatism and field curvature could help to eliminate the lower-order ocular aberrations over a larger central field. In addition, one could incorporate elements in the pupil to compensate for typical values of the spherical aberration and also compensate the misalignment coma aberration. This can be done using a dedicated adaptive optics (*AO*) system with a deformable mirror conjugated to the pupil. Using adaptive optics in conjunction with variable field corrector might be an alternative to the multi-conjugated *AO* system proposed recently [175].

Based on our observations of typical variations in distribution of the *RMS* wavefront error along meridians we identified three groups of eyes. We found that nearly constant value of the *RMS* error across the field meridian does not necessarily mean that choosing foveal wavefront (or any other field point) as a reference for off-axis correction will guarantee a decent correction (or significant increase in the isoplanatic patch after correction). The three groups of typical field distributions of the total *RMS* is only one way to categorize field aberration patterns for a number of eyes. We showed that even for young and healthy eyes the field dependence of field curvature or astigmatism might significantly vary between subjects due to the subject-dependant asymmetries, misalignments or decentrations present in the optical system of the eye.

Our results strongly indicate that a proper alignment between the optical axis of an aberrometer and the eye is critical for obtaining a repeatable results. Even small movement of the pupil centre from the instrument optical axis results in increasing of

ocular aberrations. With no rotational symmetry in the eye, even in the central visual field, our suggestion is to measure optical components of the eye using the same axis of reference. The future of this approach is the new generation of instruments that can simultaneously measure the topography of the cornea and the wavefront aberration of the whole eye.

5.2 Optical Effects of Tear Film Evolution After a Single Blink

The purpose of this part in our study was to measure the changes of ocular aberrations on the visual axis after a single blink, which is directly related to the tear film evolution. The data was collected for 5 young eyes without any corneal abnormalities. The accommodation of the eye was paralyzed by 1 percent drop of Tropicamide to avoid changes in ocular aberrations due to the crystalline lens refocusing. Numerical analysis of each single Zernike coefficient (up to 5th order) was performed to study the variations of its amplitude after blinking.

The influence on wavefront causing by the tear film (*TF*) has been reported previously. The significance of the *TF* stems from the fact that, as the most anterior optical surface of the eye, it undergoes the largest change in refractive index, which makes this optical surface the most powerful. Hence any local changes in the tear film thickness and regularity lead to changes in the ocular aberrations pattern. After a blink, tears are moving rapidly with the upper eyelid and after one second tear spreading velocity drops to minimum [176]. Over a certain post-blink time, the pre-corneal *TF* undergoes a significant changes in its distribution, which can significantly influenced the wavefront shape and degrade the retinal image quality [93,97,115,159,161,163,168,177–179]. It has also a non-negligible impact for achieving high quality retinal images [93,115]. Recent study by Kimball *et.al* [180], indicated the evaporation of the aqueous component as the main factor of the *TF* thinning and break-up, which confirmed previous findings of Thibos and colleagues [115]. The other conclusion from the work of Kimball was that an evaporation process is even much faster than previously reported.

The stability of the pre-corneal tear film is a non-negligible factor when talking about open-loop *AO* correction over an isoplanatic region. As we have showed, it can change the actual shape of the wavefront, which causes local changes in aberration amplitude. However our statement about the tear film is not quantitatively strong

(limited data and other factors cause fluctuations of ocular wavefronts in time), we believe, that in our analysis the contribution from the TF fluctuation on the cornea surface is dominant.

The changes in thickness of the tear film after a blink is a known fact. It has been well documented that after a blink, the TF became thicker at the superior cornea and thinner at the inferior cornea during the "*build-up*" phase [179]. A possible mechanism for this is that, immediately after a blink, thinner lipid layer in the superior cornea causes a high surface tension, which results in upward drift of the TF and hence provides a thicker layer of tear in the upper cornea [181].

We found a significant correlation between coma-like wavefront aberrations and the time elapsed after a single blink. This result supports previous findings [178, 179]. It was suggested that such an influence on these types of the ocular aberration comes from a thicker layer of tears at the inferior edge of the cornea or thinner layer at the superior edge of the cornea due to gravity. This effect may be responsible for creating asymmetry, primarily in the vertical meridian of the cornea. In the work of Montés-Micó *et.al* [178], coma-like aberrations were found to increase with time after a blink and similar effect was found by Koh and colleagues [163]. Although in our case we do not see any obvious pattern in decreasing or increasing coma-like aberrations after the blink, but we observed that changes in the tear film are contribute to the changes in coma-like aberrations. As it has been suggested earlier, coma-like aberrations are sensitive to the thickness of tear film on the cornea surface, but the distribution of tears may differ from eye to eye [179]. Our results show a significant changes in spherical aberration after a blink. This has been reported earlier with a suggestion that it may be an effect of more rapid tear evaporation and thinning at the center of the cornea compared with the periphery [178].

All the subjects in our study ($n = 5$) displayed a statistically significant correlation between horizontal astigmatism coefficient $c(2,2)$ and the time after the blink. Combined astigmatism strongly contributed to the residual RMS wavefront error (see Fig. 4.13 for reference). The influence of the tear film on the horizontal astigmatism may be attributed to its vertical axis of symmetry (in the pupil plane). This is also valid for our observation about the 3^{rd} coma-like aberration coefficients and spherical aberration, these aberration terms display vertical axis of symmetry, which means that they are more liable to react with the changes of the tear film on the corneal surface.

It seems understandable that the stability of ocular aberrations is critical for highly efficient corrections. It is especially important when fixed aberration pattern is needed

in order to fully correct ocular aberrations (e.g. customized corneal ablation). Hence if, for any reason, the optical system of the eye is not stable, there is not possible to find a fixed correction pattern.

A question arises: what is the origin of the changes in wavefront aberration that is associated with the fluctuation of tear film?

One of our conclusion is: the tear film does help to maintain good quality image on the retina under condition that it is evenly distributed on the corneal surface. It helps in covering all irregularities and roughness of the corneal epithelium layer. The local changes in thickness after a single blink, lack of uniformity of the refractive index of the *TF*, uneven surface of the tear film caused by evaporation and finally break-up of the *TF* are responsible for changing the aberrations pattern of ocular wavefront and, in consequence in some cases, degrading the retinal image quality. Although we were able to measure its influence to the whole eye amount of aberrations, we are not certain about its exact origins, which may occur with variety of combinations. In

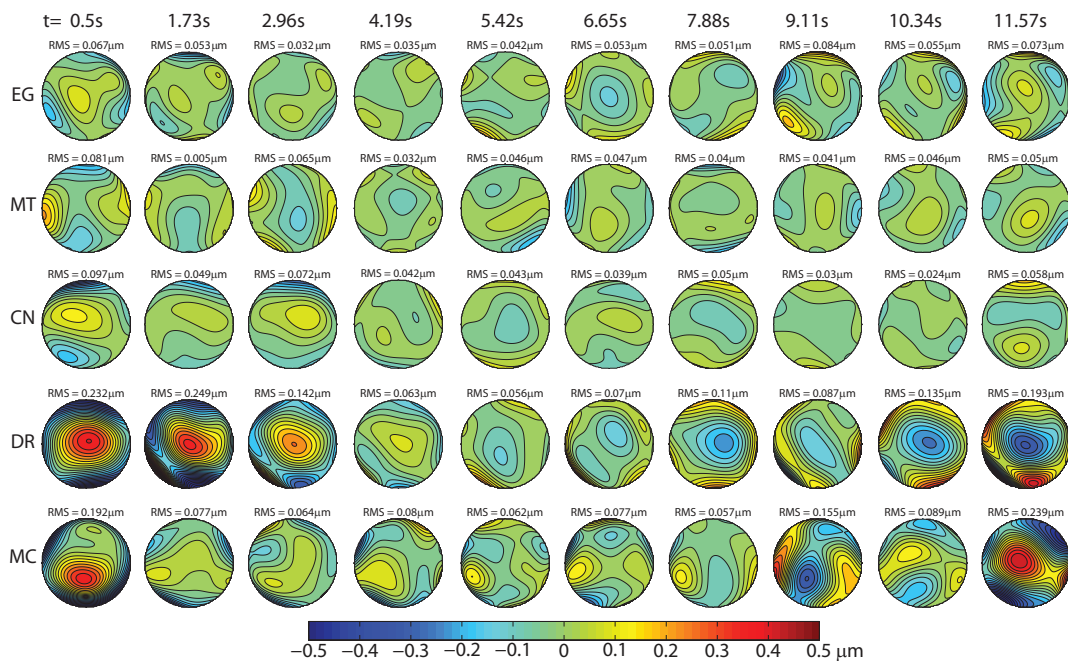


Figure 5.7: Mean residual phase maps of the wavefront aberration for each subject as a function of time elapsed from the start of experiment. For the sake of clarity, only 10 wavefronts out of 20 are shown (t indicates time after the blink). Wavefronts were reconstructed using 18 first Zernike terms over a 6 mm pupil (tip and tilt were removed).

conclusions, we found that after a single blink a tear film exhibits temporal variation

on the corneal, which has non-negligible optical effects to the whole eye aberration pattern. In order to illustrate the nature of the changes in the wavefront aberration pattern in the individual eye after a blink, Fig. 5.7 presents mean residual phase maps of the wavefront aberration for each subject. The phase maps are reconstructed using 18 first Zernike aberration terms (tip and tilt are removed) over a 6 mm pupil. It can be easily seen that the changes of the wavefront differ in terms of magnitude for each eye.

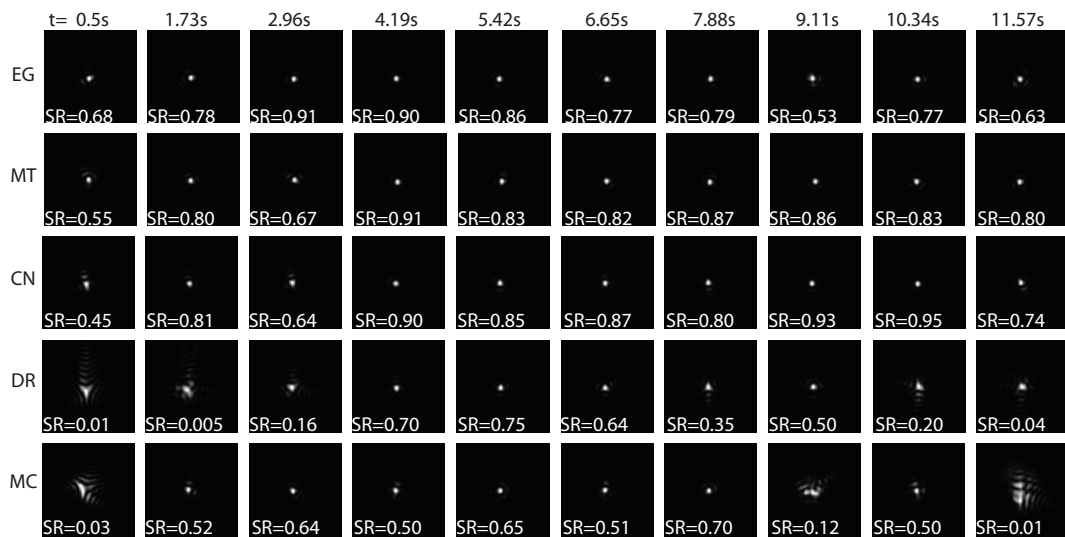


Figure 5.8: The *PSF* images for a 6 mm pupil diameter at $\lambda = 677 \text{ nm}$ and corresponding value of the Strehl ratio (*SR*) for each subject as a function of time elapsed after the blink. The corresponding wavefront error *RMS* (from which the *PSF* and the *SR* were calculated) is shown in Fig. 5.7.

Figure 5.8 shows the *PSF* images (based on the Fourier transform of the corresponding wavefronts from Fig. 5.7) and the Strehl ratio values (*SR*). The variables used in the calculation of the corresponding *PSF* are: pupil diameter of 6 mm, reference wavelength of $\lambda = 677 \text{ nm}$, nodal distance of $n = 16.7 \text{ mm}$. The images of the *PSF* were re-scaled in size, in order to make the spatial structures more visible in the images. This shows again the optical effect due to the tear film variation does not have the same magnitude for all subjects.

From our data analysis we conclude that the optical effects caused by the tear film cannot be neglected. Before any wavefront analysis is performed, one shall take into account the tear film effect, but the optimal way of doing it is yet to be found. Below we list some related questions:

- At what time (after a single blink) the ocular wavefront shall be measured? Immediately after a blink; when the *TF* still may unevenly cover the cornea, causing a large variation in aberration pattern, or while it is well distributed (stable phase) over the corneal surface causing minor changes to the wavefront. In the latter case, the difficult is, that the stabilization process of the *TF* may differ in terms of time after a blink from eye to eye, so additional measurements prior to representative wavefronts measurements will be required.
- How can we minimize the optical effect of the tear film in the data analysis? Although, averaging experimentally obtained wavefront frames is a possibility, the question is still valid: how many and over which time period one should collect and average wavefront frames?
- Is it representative to use just one blink measurement on any aberrometer?

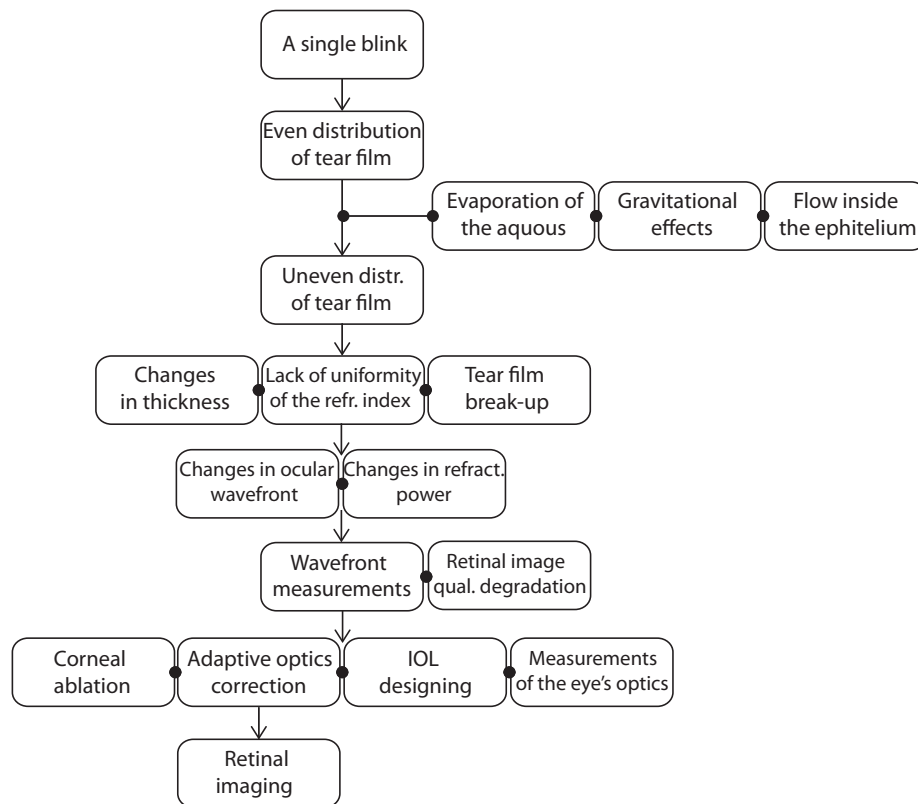


Figure 5.9: An illustrative diagram showing possible factors and results of an uneven distribution of the tear film on the corneal surface. It also shows which regions of the eye research may be affected due to tear film variations.

Our results on the changes in ocular wavefront inducted by the pre-corneal tear film

fluctuation indicate that a more careful and complex measurement regime is needed. It would be appropriate to measure ocular wavefront aberration and the tear film distribution on the cornea (in terms of changes in thickness for example) at the same time.

Figure 5.9 presents an illustrative diagram showing possible factors and results of an uneven distribution of tear film on the corneal surface. As a non-negligible factor, the tear film should be carefully considered especially in all cases when ocular wavefront measurement is a starting point for widely understood correction of the ocular aberrations of the eye (e.g wavefront guided laser eye surgery or *AO* correction). In order to create more realistic eye model, the information about pre-corneal tear film should be added.

5.3 Future Work and Applications

Our experimental results indicate that there is large inter-subject variability in aberrations pattern even within 25 young eyes in the study. We observed that there are different types of the distribution of the total *RMS* error along the field of view and we distinguished 3 different groups. Although this is just one way for categorizing the experimental data, it shows that even for young eyes (without any optical abnormalities) there is no consistency between horizontal and vertical meridians, which uncover the lack of symmetry in both meridians. We shown that even for the eyes of similar distribution of the total *RMS* error, the residual aberrations (with respect to the line of sight (*LOS*)) may have different patterns of field distribution. For a better understanding one shall look into a single Zernike aberration mode, and analyse its field behavior.

Figure 5.10 shows wavefronts measured over two eyes with varying distribution of the total *RMS* error along the horizontal meridian. The eye no. 14 represents a quadratic distribution of the total *RMS* and the eye no. 4 a non-varying distribution of the total *RMS*, with its amplitude within $RMS = 0.1 \mu m$. Figure 5.10 also presents the $c(2,0)$ defocus coefficient as a function of the horizontal field angle for both *A* and *B*. Case *A* corresponds to the original measured set of wavefronts. Case *B* corresponds to the effect of subtracting the central wavefront from each field point. This can be regarded as a perfect correction on-axis by a corrector (*DM*) conjugated to the pupil. Corresponding plots (right hand side), show the field variation of defocus. Because of quadratic field dependance of the defocus, the corrector operating on-axis may not

be efficient for a good compensation. We shall bear in mind that in our study, defocus term was minimized on-axis by a Badal system prior to each eye measurement (this explains small values for $c(2,0)$ on-axis). Without initial correction from the Badal, one can expect the value of defocus being higher on-axis with the shape of the field distribution curve as preserved.

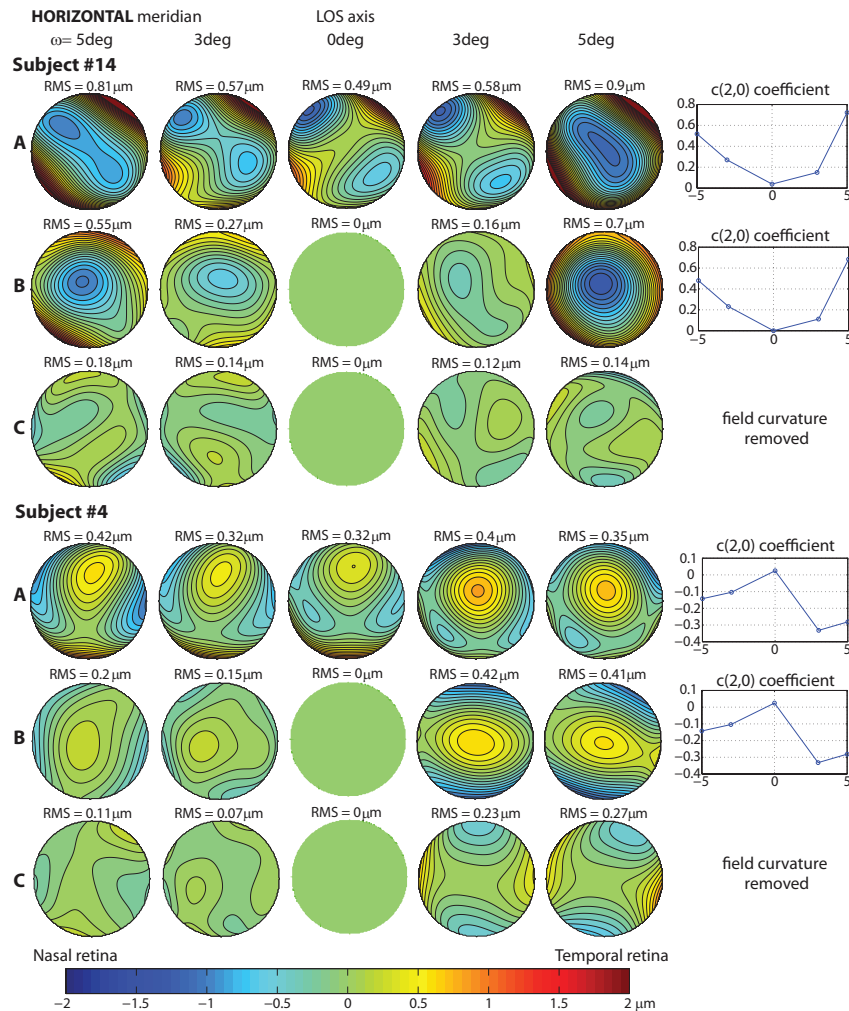


Figure 5.10: Wavefront aberration distribution across the **horizontal** visual field for the eye no.14 and no.4. Case **A** presents the original measured wavefronts (with the Zernike defocus aberration minimized on-axis with the Badal system). Case **B** shows the residual wavefronts after subtracting the central wavefront along the line of sight axis (*LOS*). Case **C** illustrates the case of completely removing field curvature term. For both eyes the values of defocus $c(2,0)$ coefficient as a function of horizontal field angle are also plotted.

Case C illustrates an effect of removing field curvature from residual wavefronts com-

pletely and hence improving the wavefront quality. This can be done by using variable field corrector, or field-flattener in this case. The next step would be to correct the field-dependent component of astigmatism, which can be achieved with variable conventional optics. Proposed solution, deformable mirror operating on-axis and variable optical correctors, might be an alternative to multi-conjugated AO systems.

Our experimental data on young population eyes may be incorporated into a model eye, which describes the central field of view with all decentrations, shifts and tilts of optical components of the optical system of the eye. This brings us to another question: how far shall we go with complexity of such a model? How many and which parameters should be used to build such a model that is valid for on-axis and off-axis aberrations prediction? Little is known about a complex structure of the crystalline lens and its refractive index distribution. This remains an ultimate challenge in eye modeling.

Our aberration distribution within central visual field results, are affected mainly due to tear film variation on the cornea. It may affect actual image we gathered about aberration pattern in the 10 by 10 *degree* field of view. This fact yields for searching other solutions that may efficiently help to fight some of the unwanted factors. Instruments that can simultaneously measure wavefront of the entire eye and topography and the corneal wavefront with respect to the same axis have been recently demonstrated. This will help to reconstruct the optical parameters of the eye in a more efficient way. Although it is a big step forward in the eye metrology, an instrument that would be able to measure field aberrations simultaneously, rather than sequentially, should be aimed in the future.

Our future work along the main line of our experimental results on off-axis aberrations and the optical effects of the tear film evolution are as follows:

- For a better statistical knowledge of the off-axis distribution of ocular aberrations one needs to measure more eyes. It would be especially beneficial for the design of physical model eye and provide the input requirements for variable conventional optics to correct field aberrations.
- Future path could be to find optimum way of doing ocular tomography for which one could use the dedicated instrument featuring corneal topographer and wavefront sensor operating on the same axis. This could help to disentangle the cornea aberrations from crystalline lens field aberrations, in particular astigmatism and field curvature. The balancing mechanism for the corneal and lenticu-

lar aberrations is of high interest in ophthalmic area.

- Accounting for tear film optical effects in eye models would be our next step (finding a way to describe the "*effective*" tear film distribution based on time averaging).
- Our future work will be to use 25 specified-eye models to identify the isoplanatic patch size in young eyes using instantaneous tears profile.
- Having a more realistic representation of human eye, one could decompose ocular aberrations into the constant components and field-dependent components. This could help to complement the Seidel theory of aberrations with the new types of aberrations originating from misaligned and rotational-asymmetric surfaces in the eye.
- It would also be helpful to find the useful way of reporting the off-axis aberrations in human eye, which avoids ellipticity of entrance pupil occurring at oblique angles.

Bibliography

- [1] George Smith David A. Atchison. *Optics of the Human Eye*. Butterworth-Heinemann, 2000.
- [2] P. Artal and J. Tabernero. Optics of human eye: 400 years of exploration from Galileo's time. *Appl. Optics*, 49(16):123–130, 2010.
- [3] W. N. Charman. Wavefront technology: Past, present and future. *Contact Lens and Anterior Eye*, 28:75–92, 2005.
- [4] H. Helmholtz. *Treatise on physiological optics*. Dover Publications, Inc. New York, 2005.
- [5] N. J Wade and S. Finger. The eye as an optical instrument: from camera obscura to Helmholtz's perspective. *Perception*, 30(10):1157–1177, 2001.
- [6] A. Plesh and U. Klingbeil. Optical characteristics of a scanning laser ophthalmoscope. *SPIE proc.*, 1161:390–398, 1989.
- [7] A. G. Podoleanu, G. M. Dobre, D. J. Webb, and D. A. Jackson. Simultaneous en-face imaging of two layers in the human retina by low-coherence reflectometry. *Opt. Letters*, 22(13):1039–1041, 1997.
- [8] H. W. Babcock. The possibility of compensating astronomical seeing. *Publ. Astr. Soc. Pac.*, 65:229–236, 1953.
- [9] J. Liang and D. R. Williams. Aberrations and retinal image quality of the normal human eye. *J. Opt. Soc. Am. A*, 14(11):2873–2883, 1997.
- [10] A. Roorda, F. Romero-Borja, W. J. Donnelly III, H. Queener, T. J. Hebert, and M. C. W. Campbell. Adaptive optics scanning laser ophthalmoscopy. *Opt. Express*, 10(9):405–412, 2002.
- [11] L. Diaz-Santana, C. Torti, I. Munro, P. Gasson, and C. Dainty. Benefit of higher closedloop bandwidths in ocular adaptive optics. *Opt. Express*, 11(20):2597–2605, 2003.

- [12] D. Miller, J. Qu, R. S. Jonnal, and K. E. Thorn. Coherence gating and adaptive optics in the eye. *SPIE proceedings*, 4956:65–72, 2003.
- [13] B. Hermann, E. J. Fernández, A. Unterhuber, H. Sattmann, A. F. Fercher, W. Drexler, P. M. Prieto, and P. Artal. Adaptive-optics ultrahigh-resolution optical coherence tomography. *Opt. Letters*, 29(18):2142–2144, 2004.
- [14] C. Torti, B. Považay, B. Hofer, A. Unterhuber, J. Carroll, P. K. Ahnelt, and W. Drexler. Adaptive optics optical coherence tomography at 120,000 depth scans/s for non-invasive cellular phenotyping of the living human retina. *Opt. Express*, 17(22):19382–19400, 2009.
- [15] M. Wojtkowski. High-speed optical coherence tomography: basics and applications. *Appl. Optics*, 49(16):30–61, 2010.
- [16] E. Dalimier. *Adaptive Optics Correction of Ocular Higher-Order Aberrations and the Effects on Functional Vision*. PhD thesis, National University of Ireland, Galway, 2007.
- [17] E. Dalimier and C. Dainty. Use of a customized vision model to analyze the effects of higher-order ocular aberrations and neural filtering on contrast threshold performance. *J. Opt. Soc. Am. A*, 25(8):2078–2087, 2008.
- [18] E. Dalimier and C. Dainty. Role of ocular aberrations in photopic spatial summation in the fovea. *Opt. Letters*, 35(4):589–591, 2010.
- [19] S. Patel, J. Marshall, and F. W. Fitzke. Shape and radius of posterior corneal surface. *Refract. Corn. Surg.*, 9:173–181, 1993.
- [20] B. K. Pierscionek and R. C. Augusteyn. Shapes and dimensions of in vitro human lenses. *Clin. Exp. Optom.*, 74:223–228, 1991.
- [21] J. P. Craig, P. A. Simmons, S. Patel, and A. Tomlinson. Refractive index and osmolality of human tears. *Optom. Vision Sci.*, 72(10):718–724, 1995.
- [22] D. H. Szczesna, Z. Kulas, H. T. Kasprzak, and U. Stenevi. Examination of in vivo tear film stability after eye blink and eye drying. *Proc. of SPIE-OSA Biomedical Optics, SPIE*, 6633:663314–8, 2007.
- [23] Linda Lundström. *Wavefront Aberrations and Peripheral Vision*. PhD thesis, Royal Institute of Technology, Stockholm, Sweden, 2007.
- [24] P. M. Kiely, G. Smith, and L. G. Carney. The mean shape of the human cornea. *Optica Acta*, 29(8):1027–1040, 1982.
- [25] J.D. Bartlett and S.D. Janus. *Clinical ocular pharmacology (4th edition)*. Butterworth-Heinemann, London, 2000.
- [26] M. Rynders, B. Lidkea, W. Chisholm, and L. N. Thibos. Statistical distribution of foveal transverse chromatic aberration, pupil centration, and angle ψ in a population of young adult eyes. *J. Opt. Soc. Am. A*, 12(10):2348–2357, 1995.

- [27] M. A. Wilson, M. C. W. Campbell, and P. Simonet. Change of pupil centration with change of illumination and pupil size. *Optom. Vision Sci.*, 69(2):129–136, 1992.
- [28] H.A. Weeber. *Mechanics of Human Accommodation and Presbyopia*. Ponsen & Looijen B.V., 2008.
- [29] H. L. Liou and N. A. Brennan. Anatomically accurate finite model eye for optical modeling. *J. Opt. Soc. Am. A*, 14:1684–1695, 1997.
- [30] S. Barbero and S. Marcos. Analysis of the optical field on the human retina from wavefront aberration data. *J. Opt. Soc. Am. A*, 25(9):2280–2285, 2008.
- [31] R.S. Snell and M. A. Lemp. *Clinical anatomy of the eye*. Blackwell Science, Inc., 1998.
- [32] P. L. Kaufman and A. Alm. *Adler's physiology of the eye: clinical application*. Mosby-Year Book Inc., 11830 Westline Industrial Drive, St. Louis, Missouri 63146, 10th edition, 2003.
- [33] H. Gross. *Handbook of Optical Systems, Volume 1, Fundamentals of Technical Optics*. Wiley-VCH Verlag GmbH & Co. KGaA, Weinheim, Germany, 2005.
- [34] S. Marcos, S. A. Burns, P. M. Prieto, R. Navarro, and B. Baraibar. Investigating sources of variability of monochromatic and transverse chromatic aberrations across eyes. *Vision Res.*, 41(28):3861–3871, 2001.
- [35] R. Navarro, L. González, and J. L. Hernández. Optics of the average normal cornea from general and canonical representations of its surface topography. *J. Opt. Soc. Am. A*, 23(2):219–232, 2006.
- [36] J. Tabernero, A. Benito, V. Nourrit, and P. Artal. Instrument for measuring the misalignments of ocular surfaces. *Opt. Express*, 14(22):10945–10956, 2006.
- [37] R. Mandell, C. Chiang, and S. Klein. Location of the major corneal reference points. *Optom. Vision Sci.*, 72:776–784, 1995.
- [38] T. O. Salmon and L. N. Thibos. Videokeratoscope-line-of-sight misalignment and its effect on measurements of corneal and internal ocular aberrations. *J. Opt. Soc. Am. A*, 19(4):657–669, 2002.
- [39] D. A. Atchison. Anterior corneal and internal contributions to peripheral aberrations of human eyes. *J. Opt. Soc. Am. A*, 21(3):355–359, 2004.
- [40] A. Gullstrand. *Handbuch der Physiologischen Optik*, volume 1. J. P. Southall trans., 3rd edition, 1909. Appendix II.
- [41] S. G. El Hage Y. Le Grand. *Physiological Optics*. Springer-Verlag, 1980.
- [42] H. H. Emsley. *Visual optics (Vol. 1)*. Butterworths, 5th ed. edition, 1952.

- [43] L. N. Thibos, M. Ye, X. Zhang, and A. Bradley. The chromatic eye: a new reduced-eye model of ocular chromatic aberration in humans. *Appl. Opt.*, 31:3594–3600, 1992.
- [44] A. G. Bennett. A method of determining the equivalent powers of the eye and its crystalline lens without resort to phakometry. *Ophthalm. Physiol. Opt.*, 8(1):53–59, 1988.
- [45] W. Lotmar. Theoretical eye model with aspherics. *J. Opt. Soc. Am.*, 61:1522–1529, 1971.
- [46] O. Pomerantzeff, M. Pankratov, G. J. Wang, and P. Dufault. Wide-angle optical model of the eye. *Am. J. Optom. Physiol. Opt.*, 61:166–176, 1984.
- [47] I. H. Al-Ahdali and M. A. El-Messiery. Examination of the effect of the fibrous structure of a lens on the optical characteristic of the human eye: a computer-simulated model. *Appl. Opt.*, 25:5738–5745, 1995.
- [48] Y. J. Liu, Z. Q. Wang, L. P. Song, and G. G. Mu. An anatomically accurate eye model with a shell-structure lens. *Optik*, 116:241–246, 2005.
- [49] A. Popiołek-Masajada. Numerical study of the influence of the shell structure of the crystalline lens on the refractive properties of the human eye. *Ophthalm. Physiol. Opt.*, 19(1):41–28, 1999.
- [50] J. W. Blaker. Toward an adaptive model of the human eye. *J. Opt. Soc. Am.*, 70:220–223, 1980.
- [51] G. Smith, D. Atchison, and B. Pierscionek. Modeling the power of the aging human eye. *J. Opt. Soc. Am. A*, 9:2111–2117, 1992.
- [52] A. V. Goncharov and C. Dainty. Wide-field schematic eye models with gradient-index lens. *J. Opt. Soc. Am. A*, 24:2157–2174, 2007.
- [53] R. Navarro, F. Palos, and L. Gonzales. Adaptive model of the gradient index of the human lens. i. formulation and model of aging ex vivo lenses. *J. Opt. Soc. Am. A*, 24:2175–2185, 2007.
- [54] G. Smith. The optical properties of the crystalline lens and their significance. *Clin. Exp. Optom.*, 86:3–18, 2003.
- [55] Y. Wang and L. N. Thibos. Oblique (off-axis) astigmatism of the reduced schematic eye with elliptical refracting surface. *Optom. Vision Sci.*, 74:557–562, 1997.
- [56] L. N. Thibos, M. Ye, X. Zhang, and A. Bradley. Spherical aberration of the reduced schematic eye with elliptical refracting surface. *Optom. Vision Sci.*, 74(7):548–556, 1997.

- [57] I. Escudero-Sanz and R. Navarro. Off-axis aberrations of a wide-angle schematic eye model. *J. Opt. Soc. Am. A*, 16:1881–1891, 1999.
- [58] R. Navarro. Accommodation-dependent model of the human eye with aspherics. *J. Opt. Soc. Am. A*, 2:1273–1281, 1985.
- [59] A. C. Kooijman. Light distribution on the retina of a wide-angle theoretical eye. *J. Opt. Soc. Am.*, 73:1544–1550, 1983.
- [60] A. V. Goncharov, M. Nowakowski, M. T. Sheehan, and C. Dainty. Reconstruction of the optical system of the human eye with reverse ray-tracing. *Opt. Express*, 16(3):1692–1703, 2008.
- [61] D. A. Atchison. Optical models for human myopic eyes. *Vision Res.*, 46(14):2236–2250, 2006.
- [62] R. C. Bakaraju, K. Ehrmann, E. Papas, and A. Ho. Finite schematic eye models and their accuracy to in-vivo data. *Vision Res.*, 48(16):1681–1694, 2008.
- [63] W. T. Welford. *Aberrations of optical systems*. Adam Hilger Ltd, Techno House, Redcliffe Way, Bristol BS1 6NX, England, 1986.
- [64] K. Creath J. C. Wyant. *Applied optics and optical engineering, Vol. XI*. Academic Press, 1992.
- [65] M. Born and E. Wolf. *Principles of optics*. Pergamon Press, 1964 and 1965.
- [66] Pierre Y. Belly et al. *The Design and Construction of Large Optical Telescopes*. Springer-Verlag New York, Inc., 2002.
- [67] Guang-Ming Dai. *Wavefront optics for vision correction*. SPIE Press, 2008.
- [68] American National Standards Institute. Methods for reporting optical aberrations of eyes. *ANSI Z80.28-2004*, 2004.
- [69] Gregory J. Michels Keith B. Doyle, Victor L. Genberg. *Integrated optomechanical analysis*. SPIE, Bellingham, Washington, USA, 2002.
- [70] J. W. Goodman. *Introduction to Fourier Optics*. New York: McGraw Hill, 1996.
- [71] K. M. Hampson. Adaptive optics and vision. *J. Modern Opt.*, 55(21):3425–3467, 2008.
- [72] C. A. Curcio and K. R. Sloan R. E. Kalina A. E. Hendrickson. Human photoreceptor topography. *J. Comp. Neurol.*, 292(4):497–523, 1990.
- [73] S. Gladysz, J. C. Christou, L. W. Bradford, R William, and L. C. Roberts. Temporal variability and statistics of the strehl ratio in adaptive-optics images. *The Publications of the Astronomical Society of the Pacific*, 120(872):1132–1143, 2008.

- [74] T. S. Ross. Limitations and applicability of the marchal approximation. *Appl. Optics*, 48(10):1812–1818, 2009.
- [75] D. R. Williams, P. Artal, R. Navarro, M. J. McMahon, and D. H. Brainard. Off-axis optical quality and retinal sampling in the human eye. *Vision Res.*, 36(8):1103–1114, 1996.
- [76] P. Artal. Calculations of two-dimensional foveal retinal images in real eyes. *J. Opt. Soc. Am. A*, 7(8):1374–1381, 1990.
- [77] N. Charman. *Handbook of Optics, vol. III, Vision and Vision Optics, Chpt. 1, Optics of the Eye*. McGraw-Hill, 2010.
- [78] J. Espinosa, D. Mas, and H. T. Kasprzak. Corneal primary aberrations compensation by oblique light incidence. *J. Biomed. Opt.*, 14(4):044003, 2009.
- [79] A. M. McKendrick and N. A. Brennan. Distribution of astigmatism in the adult population. *J. Opt. Soc. Am. A*, 13(2):206–212, 1996.
- [80] J. E. Kelly, T. Mihashi, and H. C. Howland. Compensation of corneal horizontal/vertical astigmatism, lateral coma, and spherical aberration by internal optics of the eye. *J. Vision*, 4(4):262–271, 2004.
- [81] P. Artal, A. Guirao, E. Berrío, and D. R. Williams. Compensation of corneal aberrations by the internal optics of the human eye. *J. Vision*, 1(1):1–8, 2001.
- [82] M. C. M. Dunne, G. P. Misson, E. K. White, and D. A. Barnes. Peripheral astigmatic asymmetry and angle alpha. *Ophthalm. Physiol. Opt.*, 13(3):303–305, 1993.
- [83] A. Seidemann, F. Schaeffel, A. Guirao, Lopez-Gil, and Pablo Artal. Peripheral refractive errors in myopic, emmetropic, and hyperopic young subjects. *J. Opt. Soc. Am. A*, 19(12):2363–2373, 2002.
- [84] S. G. El Hage and F. Berny. Contribution of the crystalline lens to the spherical aberration of the eye. *J. Opt. Soc. Am.*, 63(2):205–211, 1973.
- [85] R. I. Calver, M. J. Cox, and David B. Elliott. Effect of aging on the monochromatic aberrations of the human eye. *J. Opt. Soc. Am. A*, 16(9):2069–2078, 1999.
- [86] J. S. McLellan, S. Marcos, and S. A. Burns. Age-related changes in monochromatic wave aberrations of the human eye. *Invest. Ophthalmol. Vis. Sci.*, 42(6):1390–1395, 2001.
- [87] R. A. Applegate, W. J. Donnelly III, J. D. Marsack, D.E. Koenig, and K. Pseudovs. Three-dimensional relationship between high-order root-mean-square wavefront error, pupil diameter, and aging. *J. Opt. Soc. Am. A*, 24(3):578–587, 2007.
- [88] H. Cheng, J. K. Barnett, A. S. Vilupuru, J. D. Marsack, S. Kasthurirangan, R. A. Applegate, and A. Roorda. A population study on changes in wave aberrations with accommodation. *J. Vision*, 4(4):272–280, 2004.

- [89] H. Radhakrishnan and W. N. Charman. Age-related changes in ocular aberrations with accommodation. *J. Vision*, 7(7):1–21, 2007.
- [90] P. Rosales and S. Marcos. Phakometry and lens tilt and decentration using a custom-developed purkinje imaging apparatus: validation and measurements. *J. Opt. Soc. Am. A*, 23(3):509–520, 2006.
- [91] J. Tabernero, A. Benito, E. Alcón, and P. Artal. Mechanism of compensation of aberrations in the human eye. *J. Opt. Soc. Am. A*, 24(10):3274–3283, 2007.
- [92] H. S. Smirnov. Measurement of the wave aberration in the human eye. *Biophysics*, 6:52–66, 1961.
- [93] R. Tutt, A. Bradley, C. Begley, and L. N. Thibos. Optical and visual impact on tear break-up in human eyes. *Invest. Ophthalmol. Vis. Sci.*, 41(13):4117–4123, 2000.
- [94] A. Dubra. *A Shearing Interferometer for the Evaluation of Human Tear Film Topography*. PhD thesis, Imperial College, London, 2004.
- [95] A. Dubra, C. Paterson, and C. Dainty. Study of the tear topography dynamics using a lateral shearing interferometer. *Opt. Express*, 12(25):6278–6288, 2004.
- [96] D. Szcześna and D. R. Iskander. Lateral shearing interferometry for analysis of tear film surface kinetics. *Optom. Vision Sci.*, 87(7):513–517, 2010.
- [97] K. Y. Li and G. Yoon. Changes in aberrations and retinal image quality due to tear film dynamics. *Opt. Express*, 14(25):12552–12559, 2006.
- [98] S. Gruppetta, F. Lacombe, and Pascal Puget. Study of the dynamic aberrations of the human tear film. *Opt. Express*, 13(19):7631–7636, 2005.
- [99] P. Artal, A. Benito, and J. Tabernero. The human eye is an example of robust optical design. *J. Vision*, 6(1):1–7, 2006.
- [100] J. C. He, J. Gwiazda, F. Thorn, and R. Held. Wave-front aberrations in the anterior corneal surface and the whole eye. *J. Opt. Soc. Am. A*, 20(7):1155–1163, 2003.
- [101] T. Young. On the mechanism of the eye. *Philos. Trans. R. Soc. London*, 91:23–88, 1801.
- [102] G. Yoon. *Wavefront sensing and diagnostic uses, Chapter III, Adaptive optics for vision science*. John Wiley & Sons, Inc., 2006.
- [103] R. Navarro and L. A. Losada. Aberrations and relative efficiency of light pencils in the living human eye. *Optom. Vision Sci.*, 74(7):540–547, 1997.
- [104] R. Navarro and E. Moreno-Barriuso. Laser ray-tracing method for optical testing. *Opt. Letters*, 24(14):951–953, 1998.

- [105] R. H. Webb, C. M. Penney, and K. P. Thompson. Measurement of ocular local distortion with a spatially resolved refractometer. *Appl. Optics*, 31(19):3678–3686, 1992.
- [106] J. C. He, S. Marcos, R. H. Webb, and S. A. Burns. Measurement of the wavefront aberration of the eye by a fast psychophysical procedure. *J. Opt. Soc. Am. A*, 15(9):2449–2456, 1998.
- [107] P. Mierdel, M. Kaemmerer, M. Mrochen, H. E. Krinke, and T. Seiler. Ocular optical aberrometer for clinical use. *J. Biomed. Opt.*, 6(2):200–104, 2001.
- [108] R. Ragazzoni. Pupil plane wavefront sensing with an oscillating prism. *J. Modern Opt.*, 43(2):289–293, 1996.
- [109] I. Iglesias, R. Ragazzoni, Y. Julien, and P. Artal. Extended source pyramid wavefront sensor for the human eye. *Opt. Express*, 10(9):419–428, 2002.
- [110] S. Chiesa and C. Dainty. Investigation of pyramid wavefront sensor sensitivity for ophthalmic applications. *ARVO poster*, 2308/A558, 2010.
- [111] E. M. Daly and C. Dainty. Ophthalmic wavefront measurements using a versatile pyramid sensor. *Appl. Opt.*, 49(31):67–77, 2010.
- [112] J. Hartmann. Bemerkungen über den bau und die justirung von spektrographen. *Z. Instrumentenk.*, 20(47), 1900.
- [113] R. V. Shack and B. C. Platt. Production and use of a lenticular Hartmann screen. *J. Opt. Soc. Am.*, 61(656), 1971.
- [114] J. Liang, B. Grimm, S. Goelz, and J. F. Bille. Objective measurements of wave aberrations of the human eye with the use of a Hartmann-Shack wave-front sensor. *J. Opt. Soc. Am. A*, 11(7):1949–1957, 1994.
- [115] L. N. Thibos and X. Hong. Clinical applications of the Shack-Hartmann aberrometer. *Optom. Vision Sci.*, 76(12):817–825, 1999.
- [116] A. Chernysov, U. Sterr, F. Riehle, J. Helmcke, and J. Pfund. Calibration of a Shack-Hartmann sensor for absolute measurements of wavefronts. *Appl. Optics*, 44(30):6419–6415, 2005.
- [117] C. Leroux and J. C. Dainty. A simple and robust method to extend the dynamic range of an aberrometer. *Opt. Express*, 17(21):19055–19061, 2009.
- [118] F. Zhou, X. Hong, D. T. Miller, L. N. Thibos, and A. Bradley. Validation of a combined corneal topographer and aberrometer based on shack-hartmann wave-front sensing. *J. Opt. Soc. Am. A*, 21(5):683–696, 2004.
- [119] D. Neal *et.al.* Combined wavefront aberrometer and new advanced corneal topographer. *A.S.C.R.S. poster*, 416387, 2008.

- [120] L. Thibos, R. A. Applegate, J. T. Schwiegerling, and R. Webb. Standards for reporting the optical aberrations of eyes. *Vision Sci. and Its Appl.*, 35:232–244, 2000.
- [121] T.D. Raymond, D. Neal, S. Farrer, and C.D. Baer. The correlation of combined topo/wavefront measurements. *ARVO poster*, 5652/D805, 2010.
- [122] L. N. Thibos, D. L. Still, and A. Bradley. Characterisation of spatial aliasing and contrast sensitivity in peripheral vision. *Vision Res.*, 36(2):249–258, 1996.
- [123] Y. Z. Wang L. N. Thibos and A. Bradley. Effects of refractive error on detection acuity and resolution acuity in peripheral vision. *Invest. Ophthalmol. Vis. Sci.*, 38(10):2134–2143, 1997.
- [124] W. N. Charman. Aberrations and myopia. *Ophthalm. Physiol. Opt.*, 25(4):285–301, 2005.
- [125] J. Porter, A. Guirao, I. G. Cox, and D. R. Williams. Monochromatic aberrations of the human eye in a large population. *J. Opt. Soc. Am. A*, 18(8):1793–1803, 2001.
- [126] L. N. Thibos, X. Hong, A. Bradley, and X. Cheng. Statistical variation of aberration structure and image quality in a normal population of healthy eyes. *J. Opt. Soc. Am. A*, 19(12):2329–2348, 2002.
- [127] J. F. Castejón-Mochón, N. López-Gil, A. Benito, and P. Artal. Ocular wave-front aberration statistics in a normal young population. *Vision Res.*, 42(13):1611–1617, 2002.
- [128] S. Plainis and I. G. Pallikaris. Ocular monochromatic aberration statistics in a large emmetropic population. *J. Modern Opt.*, 55(4,5):759 – 772, 2008.
- [129] R. Navarro, Esther Moreno, and Carlos Dorronsoro. Monochromatic aberrations and point-spread functions of the human eye across the visual field. *J. Opt. Soc. Am. A*, 15(9):2522–2529, 1998.
- [130] D. A. Atchison and D. H. Scott. Monochromatic aberrations of human eyes in the horizontal visual field. *J. Opt. Soc. Am. A*, 19(11):2180–2184, 2002.
- [131] L. Lundström, S. Manzanera, P. M. Prieto, D. B. Ayala, N. Gorceix, J. Gustafsson, P. Unsbo, and P. Artal. Effect on optical correction and remaining aberrations on peripheral resolution acuity in the human eye. *Opt. Express*, 15(20):12654–12661, 2007.
- [132] D. A. Atchison, S. D. Lucas, R. Ashman, M. A. Huynh, D. W. Schilt, and P. Q. Ngo. Refraction and aberration across the horizontal central 10° of the visual field. *Optom. Vision Sci.*, 83(4):213–221, 2006.
- [133] A. Mathur, D. A. Atchison, and D. H. Scott. Ocular aberrations in the peripheral visual field. *Opt. Letters*, 33(8):863–865, 2008.

- [134] D. A. Atchison and E. L. Markwell. Aberrations of emmetropic subjects at different ages. *Vision Res.*, 48(21):2224–2231, 2008.
- [135] A. Mathur, D. A. Atchison, and W. N. Charman. Effects of age on peripheral ocular aberrations. *Opt. Express*, 18(6):5840–5853, 2010.
- [136] Junzhong Liang, David R. Williams, and Donald T. Miller. Supernormal vision and high-resolution retinal imaging through adaptive optics. *J. Opt. Soc. Am. A*, 14(11):2884–2892, 1997.
- [137] D. L. Fried. Anisoplanatism in adaptive optics. *J. Opt. Soc. Am.*, 72(1):52–61, 1982.
- [138] P. Bedggood, M. Daaboul, R. Ashman, G. Smith, and A. Metha. Characteristics of the human isoplanatic patch and implications for adaptive optics retinal imaging. *J. Biomed. Opt.*, 13(2):024008, 2008.
- [139] A. V. Dubinin, T. Yu. Cherezova, A. I. Belyakov, and A. V. Kudryashov. Isoplanatism of the optical system of the human eye. *J. Opt. Technol.*, 75(3):172–174, 2008.
- [140] W. Lotmar and T. Lotmar. Peripheral astigmatism in the human eye: Experimental data and theoretical model predictions. *J. Opt. Soc. Am. A*, 61:510–513, 1974.
- [141] M. T. Sheehan. Ocular aberrations. wavefront sensing in clinical application. Master’s thesis, Dublin Institute of Technology, 2007.
- [142] M. T. Sheehan, A. V. Goncharov, V. M. O’Dwyer, V. Toal, and C. Dainty. Population study of the variation in monochromatic aberrations of the normal human eye over the central visual field. *Opt. Express*, 15(12):7367–7380, 2007.
- [143] R. Navarro, E. Moreno-Barriuso, Salvador Bará, and Teresa Mancebo. Phase plates for wave-aberration compensation in the human eye. *Opt. Letters*, 25(4):236–238, 2000.
- [144] C. E. Leroux. *Time-resolved aberrometry of the eye with a Shack-Hartmann wavefront sensor*. PhD thesis, National University of Ireland, Galway, 2010.
- [145] E. Fernández, A. Unterhuber, P. Prieto, B. Hermann, W. Drexler, and P. Artal. Ocular aberrations as a function of wavelength in the near infrared measured with a femtosecond laser. *Opt. Express*, 13(2):400–409, 2005.
- [146] C. E. Leroux, A. Tzschachmann, and J. C. Dainty. Pupil matching of Zernike aberrations. *Opt. Express*, 18(21):21567–21572, 2010.
- [147] H. Hofer, P. Artal, B. Singer, J. L. Aragón, and D. R. Williams. Dynamics of the eye’s wave aberration. *J. Opt. Soc. Am. A*, 18(3):497–506, 2001.

- [148] C. Leahy, C. Leroux, C. Dainty, and L. Diaz-Santana. Temporal dynamics and statistical characteristics of the microfluctuations of accommodation: Dependence on the mean accommodative effort. *Opt. Express*, 18(3):2668–2681, 2010.
- [149] M. Bland. *An introduction to medical statistics*. Oxford University Press, 2000.
- [150] A. Guirao, J. Porter, D. R. Williams, and I. G. Cox. Calculated impact of higher-order monochromatic aberrations on retinal image quality in a population of human eyes. *J. Opt. Soc. Am. A*, 19(1):1–9, 2002.
- [151] J. R. Kuszak, R. K. Zoltoski, and C. Siverston. Fibre cell organization in crystalline lenses. *Exp. Eye Res.*, 78:673–687, 2003.
- [152] M. Di Jorio. The general theory of isoplanatism for finite aperture and field. *J. Opt. Soc. Am.*, 39:305–319, 1949.
- [153] E. M. Maida, K. Venkateswaran, J. Marsack, and A. Roorda. What is the size of the isoplanatic patch in the human eye? <http://wwwcfao.ucolick.org/EO/internshipsnew/mainland/posters/erika.pdf> (2004).
- [154] A. Dubinin, T. Cherezova, A. Belyakov, and A. Kudryashov. Anisoplanatism in human retina imaging. *Proc. SPIE*, 5894:88–94, 2005.
- [155] A. Dubinin, T. Cherezova, A. Belyakov, and A. Kudryashov. Human eye anisoplanatism: eye as a lamellar structure. *Proc. SPIE 6138*, 613813, 2006.
- [156] J. Tarrant and A. Roorda. The extent of the isoplanatic patch of the human eye. (<http://vision.berkeley.edu/wildsoet/Arvo2006/Isoplanatictin.pdf> (2006)).
- [157] J. I. Prydal and F. W. Campbell. Study of precorneal tear film thickness and structure by interferometry and confocal microscopy. *Invest. Ophthalmol. Vis. Sci.*, 33:1996–2005, 1992.
- [158] S. Barbero. Refractive power of a multilayer rotationally symmetric model of the human cornea and tear film. *J. Opt. Soc. Am. A*, 23(7):1578–1585, 2006.
- [159] M. Zhu, M. J. Collins, and D. R. Iskander. Microfluctuations of wavefront aberrations of the eye. *Ophthalm. Physiol. Opt.*, 24(6):562–571, 2004.
- [160] J. Németh, B. Erdélyi, B. Csákány, P. Gáspár, A. Soumelidis, F. Kahlesz, and Z. Lang. High-speed videotopographic measurement of tear film build-up time. *Invest. Ophthalmol. Vis. Sci.*, 43(6):1783–1790, 2002.
- [161] R. Montés-Micó, J. L. Alió, G. Munoz, and W. N. Charman. Temporal changes in optical quality of air-tear film interface at anterior cornea after blink. *Invest. Ophthalmol. Vis. Sci.*, 45(6):1757–1752, 2004.
- [162] F. J. Holly. Formation and rapture of the tear film. *Exp. Eye Res.*, 15:515–525, 1973.

- [163] S. Koh, N. Maeda, T. Kuroda, Y. Hori, H. Watanabe, T. Fujikado, Y. Tano, Y. Hirohara, and T. Mihashi. Effect of tear film break-up on high-order aberrations measured with wavefront sensor. *Amer. J. Ophthalmol.*, 134(1):115–117, 2002.
- [164] S. Martinez-Conde, S. L. Macknik, and D. H. Hubel. The role of fixational eye movements in visual perception. *Nat. Rev. Neurosci.*, 5:229–240, 2004.
- [165] M. Muma, D. R. Iskander, and M. J. Collins. The role of cardiopulmonary signals in the dynamics of the eye’s wavefront aberrations. *IEEE Trans Biomed Eng.*, 57(2):373–383, 2010.
- [166] K. M. Hampson, I. Munro, C. Paterson, and C. Dainty. Weak correlation between the aberration dynamics of the human eye and the cardiopulmonary system. *J. Opt. Soc. Am. A*, 22:1241–1250, 2005.
- [167] J. Németh, B. Erdélyi, and B. Csákány. Corneal topography changes after a 15 second pause in blinking. *J. Cataract Refract. Surg.*, 27:589–592, 2001.
- [168] S. Koh, N. Maeda, Y. Hirohara, T. Mihashi, S. Ninomiya, K. Bessho, H. Watanabe, T. Fujikado, and Y. Tano. Serial measurements of higher-order aberrations after blinking in normal subjects. *Invest. Ophthalmol. Vis. Sci.*, 47(8):3318–3324, 2006.
- [169] L. N. Thibos, X. Hong, A. Bradley, and C. G. Begley. Deterioration of retinal image quality due to break-up of the corneal tear film. (ARVO abstract). *Invest. Ophthalmol. Vis. Sci.*, 40:S544:Abstract nr 2875, 1999.
- [170] J. Gustafsson, E. Terenius, J. Buchheister, and P. Unsbo. Peripheral astigmatism in emmetropic eyes. *Ophthalm. Physiol. Opt.*, 21(5):393–400, 2001.
- [171] A. Guirao and P. Artal. Off-axis monochromatic aberrations estimated from double pass measurements in the human eye. *Vision Res.*, 39(2):207–217, 1999.
- [172] L. Lundström, J. Gus, and P. Unsbo. Population distribution of wavefront aberrations in the peripheral human eye. *J. Opt. Soc. Am. A*, 26(10):2192–2198, 2009.
- [173] E. A. H. Mallen and P. Kashyap. Measurement of retinal contour and supine axial length using the zeiss iol master. *Ophthalm. Physiol. Opt.*, 27(4):404–411, 2007.
- [174] A. Dubinin, A. Belyakov, T. Cherezova, and A. Kudryashov. Anisoplanatism in adaptive compensation of human eye aberrations. In *Optics in Atmospheric Propagation nad Adaptive Systems VII*. J.D. Gonglewski and K. Stein Eds., Proc SPIE, 5572:330-339, 2004.
- [175] P. Bedggood and A. Metha. System design considerations to improve isoplanatism for adaptive optics retinal imaging. *J. Opt. Soc. Am. A*, 27(11):37–47, 2010.

- [176] H. Owens and J. Phillips. Spreading of the tears after a blink. *Cornea*, 20(5):484–487, 2001.
- [177] C. Albarrán, A. M. Pons, and A. Lorrente. Influence of the tear film on optical quality of the eye. *Contact Lens and Anterior Eye*, 20(4):129–135, 1997.
- [178] R. Montés-Micó, J. L. Alió, G. Muñoz, J. J. Pérez-Santonja, and W. N. Charman. Postblink changes in total and corneal ocular aberrations. *Ophthalmology*, 111(4):758–767, 2004.
- [179] Mingxia Zhu. *Microfluctuations of wavefront aberrations*. PhD thesis, Centre for Eye Research, School of Optometry, Queensland University of Technology, Brisbane, Australia, 2005.
- [180] S. H. Kimball, P. E. King-Smith, and J. J. Nichols. Evidence for the major contribution of evaporation to tear film thinning between blinks. *Invest. Ophthalmol. Vis. Sci.*, 52:6294–6297, 2010.
- [181] P. E. King-Smith, B. A. Fink, R. M. Hill, K. W. Koelling, and J. M. Tiffany. The thickness of the tear film. *Current Eye Res.*, 29(4-5):357–368, 2004.